

Kondo Physics and Many–Body Effects in Quantum Dots and Molecular Junctions

A dissertation presented to
the faculty of
the College of Arts and Sciences of Ohio University

In partial fulfillment
of the requirements for the degree
Doctor of Philosophy

David A. Ruiz–Tijerina

December 2013

© 2013 David A. Ruiz–Tijerina. All Rights Reserved.

This dissertation titled
Kondo Physics and Many–Body Effects in Quantum Dots and Molecular Junctions

by
DAVID A. RUIZ–TIJERINA

has been approved for
the Department of Physics and Astronomy
and the College of Arts and Sciences by

Sergio E. Ulloa
Professor of Physics and Astronomy

Robert Frank
Dean, College of Arts and Sciences

ABSTRACT

RUIZ-TIJERINA, DAVID A., Ph.D., December 2013, Physics

Kondo Physics and Many-Body Effects in Quantum Dots and Molecular Junctions (133 pp.)

Director of Dissertation: Sergio E. Ulloa

In this document we present a study of the thermodynamic and transport properties of two kinds of quantum impurity systems in the Kondo regime. The first system consists of a spin-1 molecule in which mechanical stretching along the transport axis produces a magnetic anisotropy. We find that a generic coupling between a vibrational mode along this axis and the molecular spin induces a correction to the magnetic anisotropy, driving the ground state of the system into a non-Fermi-liquid phase. A transition into a Fermi-liquid ground state can then be induced by means of stretching, going through an underscreened spin-1 Kondo ground state at zero effective anisotropy.

In the second system we study the effects of a charge detector, implemented by a quantum point-contact (QPC), on the Kondo state of a nearby spin-1/2 quantum dot (QD). While making the charge detection possible, the Coulomb interaction between the electrons traversing the QPC and those within the QD contribute to decoherence of the Kondo state. By modeling the QPC as two metallic terminals connected to an intermediate localized level, we can explore three transport regimes of the detector: a zero-conductance regime, a finite-conductance regime in mixed valence, and unitary conductance in a Kondo ground state that has been suggested as an explanation to the “0.7 anomaly” in QPCs. Transitions between these different ground states can be achieved by tuning the strength of a capacitive coupling that parameterizes the electrostatic interaction.

DEDICATION

To my beloved mother and sister

ACKNOWLEDGEMENTS

Through the years of academic and scientific work that I spent at Ohio University, I had the fortune of meeting many people that influenced me, taught me, and some who changed my life for the better. So many, in fact, that these short pages of acknowledgement are simply not enough to do them justice. I will, however, make a humble attempt at recognizing, if only a few of them, for the wonderful things that they have done for me.

First and foremost I thank my mentor and advisor, Prof. Sergio Ulloa, for all that I have learned from him as a scientist and as a human being; for his endless patience when I went through hard times, and for all the valuable advice that he has given me. His unwavering trust and the enormous freedom he always gave me helped me become a more independent, more professional researcher. I could not have asked for a better role model.

I would like to thank Edson Vernek for generously making his NRG code available to me, but more importantly for all the help and wonderful discussions we have had in our collaborations. I look forward to our future work together. I am enormously grateful to Pablo Cornaglia, who not only took the time to teach me about the subtleties of the NRG method and the physics of Kondo systems, but also was an excellent host during my unforgettable visits to Instituto Balseiro. Also to Carlos Balseiro, from whom I learned so much during my stay in Bariloche, for his encouraging attitude and useful insights during our discussions. I hope to get the chance to collaborate with both of them in the near future.

I am thankful to my committee members, Profs. Wojtek Jadwisieniczak and Saw Wai Hla, for their useful input and their constructive comments about my work. To Prof. Nancy Sandler who taught me so much during her courses, our group meetings and personal and professional discussions outside of work, and for her friendship, which I value deeply. Also to Prof. Horacio Castillo, who taught me so much during courses,

discussions, and in my TA work under his supervision. His homework's were long, and his classes fast paced, but every bit I learned from them has been tremendously useful in my work.

I would like to thank the staff and former staff of the Department of Physics and Astronomy, especially Tracy Inman, Candy Dishong, Julie Goettge, Wayne Chiasson, Don Roth, and Ennice Sweigart. I truly appreciate their constant help, their patience and the kindness they always show me and my classmates.

There is a special place in my heart for my group mates, who through these years became my family away from home: through hardship and joy, endless homework and research challenges, Tejinder Kaur, Mahmoud Asmar and I were always together, supporting and taking care of each other. Then Mariama Rebello Sousa Dias came over from Brasil an became part of our little family, always a great colleague, a great listener and full of energy. They became like my brother and sisters, and I will always be thankful for having them in my life. I also treasure the great times I spent with Greg Petersen in Athens, Bariloche and Buenos Aires— it was impossible to get bored with him around—, and my friends Ginetom Diniz, Daiara Faria and Diego Mastroguseppe.

Thanks also to my friends outside my research group: Ramana Thota, Lisa Cashmore and Omar Jamil, and all my class mates. I especially thank Karina Avila for all the support and encouragement she showed me since day one at Ohio University; I am truly grateful for our wonderful friendship, and for her always believing in me.

Finally, I wish to thank my family and friends back home in México for their constant support and encouragement during my studies at Ohio University. All the courage it took to leave my home, to compete with my classmates and to go from a student to a professional, I got from their belief in me. I would be nowhere near where I stand today, if it were not for the hard work of my mother, and all the effort she put into my upbringing and education since the day I was born. She and my sister were always the

rock that supported me on all my endeavors. And last, but not least, to the memory of my godfather, Samuel Javier Tijerina, who inspired me to chase my dreams, and who first showed me that one can be passionate about knowledge.

TABLE OF CONTENTS

	Page
Abstract	3
Dedication	4
Acknowledgements	5
List of Tables	10
List of Figures	11
List of Symbols	13
1 Introduction	14
2 The Kondo effect	16
2.1 Introduction	16
2.2 The Kondo problem	17
2.3 The Kondo effect in nanostructures	20
3 Wilson's numerical renormalization group	26
3.1 Renormalization group theory	26
3.1.1 Introduction	26
3.1.2 The renormalization group transformation	27
3.1.3 Fixed points	29
3.1.4 Poor man's scaling of the $s - d$ model	31
3.1.5 Summary	36
3.2 The numerical renormalization group	36
3.2.1 Mapping the Anderson model onto a tight-binding chain	37
3.2.2 Iterative diagonalization and RG flow of the eigenvalues	45
3.3 The Kondo effect revisited	49
4 Dynamical magnetic anisotropy in a spin-1 molecular junction	54
4.1 Molecular vibrations and dynamic anisotropy	58
4.2 Anisotropic Kondo Hamiltonian	66
4.3 Conductance calculations	73
4.4 Effective magnetic moment calculations	79
4.5 Conclusions	83

5	Decoherence effects of a charge detector on a nearby quantum dot	84
5.1	Introduction	84
5.2	Variational calculation of the Kondo ground state of the SIAM	88
5.3	Variational calculation of the ground state of two capacitively-coupled QDs	93
5.4	Quantum charge fluctuations of dot q and their effects on dot d	102
5.5	Conclusions	110
5.6	Future work on capacitively-coupled quantum dots	111
6	Final remarks and outlook	113
	Bibliography	115
	Appendix A: Dynamical anisotropy	121
	Appendix B: Detailed calculation of the variational ground state for the SIAM	132

LIST OF TABLES

Table	Page
4.1 Higher energy states of the Hamiltonian H_0 , given by Eq. (4.5).	60
4.2 Higher energy states of the Hamiltonian H_M , given by Eq. (4.12).	62
4.3 List of states in the sub-basis considered in the calculation of the Kondo Hamiltonian.	70
A.1 Matrix elements involving the molecular state $ T, +1; \tilde{n}\rangle$	125
A.2 Matrix elements involving the molecular state $ T, -1; \tilde{n}\rangle$	126
A.3 Matrix elements involving the molecular state $ T, -1; \tilde{n}\rangle$	128

LIST OF FIGURES

Figure	Page
2.1 Resistance minimum at low temperatures for dilute magnetic alloys.	17
2.2 Feynman diagram for the $s - d$ model up to second order in perturbation theory	18
2.3 (a) Scanning electron microscope image of a SET. (b) Energy level structure of the SET's central region.	21
2.4 Zero-bias conductance measurements of the SET, as a function of gate voltage	23
3.1 Flow of the coupling constants of the s - d model, obtained through Anderson's poor man's scaling RG scheme	35
3.2 Virtual spin flip process in the interacting Anderson model	39
3.3 Logarithmic discretization used in the numerical renormalization group method, with discretization parameter $\Lambda = 2$	40
3.4 Renormalization group flow of the lowest-lying energy levels of the single-impurity Anderson Hamiltonian	47
3.5 First two stages of the iterative diagonalization procedure.	49
3.6 (a) Entropy and (b) magnetic-moment-squared of the symmetric, single-impurity Anderson model, as functions of temperature	51
3.7 NRG results for the local spectral density at the impurity site for the single-impurity Anderson model.	53
4.1 The molecule Co(tpy-SH) between metallic leads.	55
4.2 SEM image of the break junction setup.	55
4.3 Phase diagram of the spin-1 molecular system, with dynamic anisotropy. . . .	71
4.4 Second-stage Kondo temperature T_K^* obtained by means of NRG calculations. .	74
4.5 Total spectral density at the molecular level a	76
4.6 Zero-bias conductance as a function of temperature, for different values of the net anisotropy	79
4.7 Effective magnetic moment squared of the system as a function of temperature.	81
4.8 Maps of μ^2 as a function of ω_0 and A_1	82
5.1 Experimental setup of the two-slit experiment performed by Buks, <i>et al.</i>	85
5.2 Depiction of the zero-bias conductance profile of a typical QPC, as a function of gate voltage.	87
5.3 Comparison between the numerical solution to Eq. (5.12), and the approximate solution Eq. (5.13). All parameters in units of the half bandwidth D	92
5.4 Charge and charge fluctuations within a QD, as a function of gate voltage: comparison between variational solution and NRG results	94
5.5 Capacitively-coupled quantum dots, d and q	94
5.6 (a) Solutions to Eqs. (5.30a) and (5.30b), for fixed QD parameters and varying u . (b) Variational calculation of the charge in dots d and q	99

5.7	Spectral densities for QDs d and q for the parameters of Fig. 5.6, evaluated using NRG.	101
5.8	Low-energy charge excitations in the FOFP.	103
5.9	Low-energy charge excitations in the FOFP.	103
5.10	Solutions to the variational equations as a function of ε_q , for three different values of u : $1 \times 10^{-4} D$, $1 \times 10^{-3} D$, $1 \times 10^{-2} D$	104
5.11	Same as Fig. 5.10, but for parameters: $U_d = 0.04 D$, $U_q = 0.50 D$, $\varepsilon_d = -U_d/2$, $\Gamma_d = 0.002 D$, $\Gamma_q = 0.05 D$ and $u = 1 \times 10^{-3} D$, $5 \times 10^{-3} D$, $1 \times 10^{-2} D$	104
5.12	(a) Zero-bias conductance of QD d at low temperatures, as a function of the dot q level ε_q . (b) Suppression to the conductance ($\gamma_d := 1 - G_d/G_0$). Parameters: $U_d = 0.04 D$, $\varepsilon_d = -0.020 D$ and $-0.012 D$, $U_q = 0.5 D$, $\Gamma_d = 0.002 D$, $\Gamma_q = 0.05 D$; $u = 0.001 D$, $0.010 D$	106
5.13	(a) Zero-bias conductance of QD q at low temperatures, as a function of the dot d level ε_d . (b) Suppression to the conductance ($\gamma_q := 1 - G_q/G_0$). Parameters: $U_d = 0.04 D$, $U_q = 0.5 D$, $\varepsilon_q = -0.10 D$ and $\varepsilon_q = -0.25 D$, $\Gamma_d = 0.002 D$, $\Gamma_q = 0.05 D$; $u = 0.001 D$, $0.010 D$	107
5.14	Zero-bias conductance of QD d at low temperatures, as a function of the dot level ε_d . Parameters: $U_d = 0.04 D$, $U_q = 0.5 D$, $\Gamma_d = 0.002 D$, $\Gamma_q = 0.05 D$; $u = 0.010 D$	108
5.15	Zero-bias conductance of q at low temperatures, as a function of the dot level ε_q , for dot d in the symmetric case (green) and close to mixed-valence, but still in the Kondo regime (red). Parameters: $U_d = 0.04 D$, $\varepsilon_d = -0.020 D$ and $-0.012 D$, $U_q = 0.5 D$, $\Gamma_d = 0.002 D$, $\Gamma_q = 0.05 D$; $u = 0.010 D$	109
5.16	Conductance through dot q as a function of the energy level ε_q for $U_q = 0.05 D$. The curves correspond to the charge-dependent couplings to the band $V_q^{01} = 0.0357 D$, $V_q^{12} = 0.02523 D$, and $V_q^{01} = 0.04370 D$, $V_q^{12} = 0.0357 D$, corresponding to hybridizations $\Gamma_q^{01} = 0.002 D$, $\Gamma^{12} = 0.001 D$, and $\Gamma_q^{01} = 0.003 D$, $\Gamma^{12} = 0.001 D$	112
B.1	Variational amplitudes as a function of the impurity level energy ε_d , for $V = 0.0357 D$	133

LIST OF SYMBOLS

- Symbols:
 1. $[A, B] := [A, B]_- = AB - BA$
 2. $\{A, B\} := [A, B]_+ = AB + BA$
 3. $|A\rangle$: Denotes a fermionic state of label A in Dirac notation.
 4. $|A\rangle$: Denotes a bosonic state of label A in Dirac notation.
 5. $|A\rangle|B\rangle := |A\rangle \otimes |B\rangle$
 6. $\text{Im}\{z\}$: Denotes the imaginary part of a complex number z .
 7. \mathbb{C} : The set of complex numbers.
 8. $1_{n \times n}$: The $n \times n$ unit matrix.
- Conventions and abbreviations:
 1. SIAM: Single-impurity Anderson model
 2. QD: Quantum dot.
 3. QPC: Quantum point contact
 4. FOFP, LMFP, SCFP: Free-orbital, local-moment and strong-coupling fixed points, respectively.
 5. It is customary in the literature of quantum mechanics to distinguish between operators and complex numbers by means of a circumflex, or “hat” (operator \hat{x} , as opposed to complex number x). This convention is not followed in this document: the distinction between operators and numbers will be evident through context.
 6. The momentum quantum number \vec{k} is used frequently throughout the document. We make use of the shorthand notation $k := \|\vec{k}\|$ for the magnitude of the momentum, and in fact any other vector.
 7. Spin-up and spin-down states are denoted by an index $\sigma = \uparrow, \downarrow$. When σ appears within algebraic expressions, however, the reader should interpret: $\uparrow = +1$ and $\downarrow = -1$.
 8. In this work the temperature is usually measured in units of energy for convenience (and due to philosophical inclinations of the author). The reader should make the mental substitution $T \rightarrow k_B T$, with k_B the Boltzmann constant, unless the temperature is specifically presented in units of Kelvin. ($k_B = 8.61733 \times 10^{-5} \text{ eV K}^{-1}$)
 9. The notation “H. c.” will be used to abbreviate the Hermitian conjugate of the operator (or product of operators) immediately to the left.

1 INTRODUCTION

In the last few decades technological advances have led to exciting new possibilities in the field of surface physics. The advent of the Scanning Tunneling Microscope[1, 2] (STM) allowed to image individual molecules and atoms deposited in surfaces, and more recently to move them around at will. Lithography and etching methods have made it possible to fabricate complex, functional patterns in semiconductor surfaces at the nanoscale[3]; these systems exhibit quantum properties that can be tuned and probed by means of gate voltages, magnetic fields, etc., opening the unprecedented possibility to directly test the laws of physics at atomic scales.

In 1998, a seminal paper by Golhaber–Gordon *et al.* announced the observation of conductance signatures of the Kondo effect in a single–electron transistor[4]. This re–ignited the interest in Kondo physics, because for the first time the Kondo effect was observed in a single, tunable quantum impurity, as opposed to a bulk system of magnetic impurities embedded in a metal[5, 6]. After this, new and better fabrication techniques began developing rapidly and an ever growing number of systems have been built and studied.

The Kondo effect revival reached molecular systems as well. Electronic transport through break junction systems with molecules has been measured[7, 8], and molecules deposited on metallic surfaces have been probed with STM[9, 10], and have been shown to display all the signatures of Kondo correlations: universal behavior of the conductance and magnetic moment as functions of temperature, an enhanced zero–bias conductance, and the quenching of the latter with magnetic fields and bias voltages.

These days it is well known that the basic recipe: tunable quantum impurity system, metallic band and a hybridization between the two, is very likely to produce the Kondo effect in one form or another, in the correct parameter regime. By tuning one of these systems into and out of such a regime, we are changing the system’s ground state and

effectively driving a quantum phase transition[11]. Not only is this an interesting physical phenomenon in its own right, but it is also of vital importance for the design of novel nanoscale electronic and spintronic devices for technologies in the near and distant future.

In this document we will discuss original work in two such systems: (i) a stretchable spin-1 molecular junction[12], and (ii) two semiconductor quantum dots (QDs) coupled capacitively. In the former, we studied the effects of molecular vibrations on the magnetic anisotropy induced by stretching the molecule along the transport axis. In the latter, we studied the dephasing that one of the QDs induces in the other's Kondo ground state by means of Coulomb repulsion; this system mimics the behavior of a charge detector such as the one described in Ref. [13], with the quantum point contact (QPC) replaced by a QD in various transport regimes. We believe that our findings provide fundamental insight into the behavior of these systems and others like them, and have the added value of corresponding to real systems already available for experimentation, and of possible relevance for future design of electronic and spintronic devices at the nanoscale.

This document is organized in the following way: Chapter 2 provides a conceptual introduction to the Kondo problem, as well as a brief account of experimental observations of the Kondo effect in the bulk and in nanostructures and molecular systems. Then, our main method of calculation, the numerical renormalization group, is introduced in Chapter 3, followed by a revision of the Kondo effect. Armed with the basic concepts and calculation techniques, we proceed to discuss our study of system (i) in Chapter 4, and system (ii) in Chapter 5. Our closing remarks are presented in Chapter 6.

2 THE KONDO EFFECT

2.1 Introduction

The field of solid-state physics as we know it today was born with the advent of quantum mechanics, during the first two decades of the 20th century. The new understanding of lattice dynamics at the quantum level (phonons) and its scattering effect on electrons led to a clearer insight into the thermoelectric properties of metals, and the newly-discovered wave nature of electrons resolved discrepancies between predictions of thermodynamic and electronic transport properties of metals as described by classical kinetic theory[14, 15], and the new experimental results of the time. The predictions from the new theories were in excellent agreement with experiments on pure metals[16], but evidence of a resistance minimum in dilute magnetic alloys began to emerge[17], which could not be explained by the Drude–Sommerfeld theory of free electrons.

Figure 2.1 shows resistance measurements by de Haas and de Boer on two different gold wires with less than $10^{-4}\%$ of copper and silver impurities. According to free-electron theories, the resistance is expected to decrease monotonically at low temperatures as vibrational excitations of the lattice are quenched, until reaching a constant lower limit related to the presence of defects in the crystalline structure. The experiments, however, revealed the onset of an unexpected scattering mechanism that increases the resistance below some characteristic temperature scale ($\sim 4K$ in this case).

The origin of this additional scattering at low temperatures remained a mystery for three decades, until further experiments on the concentration of transition elements in metals[6] showed a correlation between the unknown scattering mechanism and the presence of impurities with unpaired electrons in atomic d - or f -shells. Soon after, J. Kondo[18] demonstrated the appearance of a logarithmic dependence of the resistivity with temperature ($R \sim -\log T$) through his work with the $s-d$ model proposed by

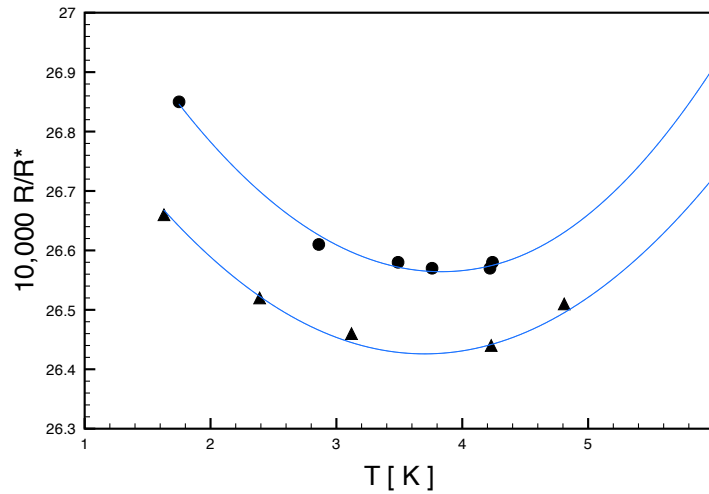


Figure 2.1: Resistance minimum at low temperatures, observed in two different gold wires with copper and silver impurities (less than $10^{-4}\%$). R^* is the corresponding sample's resistance at $T = 273.15K$: 1.936Ω and 0.264Ω , respectively. Data obtained from Ref.[17]; colored lines added as a guide to the eye.

Zener[19], and developed by Kasuya[20] and Yosida[21, 22]. This contribution to the resistivity has its origin in the exchange interaction between the impurities and the electrons from the metallic band, originating directly from the spin degrees of freedom of the problem, and appears only below a certain characteristic temperature scale— now known as the Kondo temperature— giving rise to the resistance minimum.

2.2 The Kondo problem

In spite of Kondo's success in finding the nature of the mechanism that produces the resistance minimum, his results are instead considered a *problem*, or rather the evidence of a fundamental handicap of perturbation theory in the many-body problem. Let us consider a localized spin-1/2 magnetic moment embedded in the metal, originating from either a d -shell or an f -shell, unpaired electron within an impurity. The interaction

between the electronic band and the impurity is given by the Hamiltonian

$$H_{sd} := \sum_{\vec{k}, \vec{k}'} J_{\vec{k}, \vec{k}'} \left[s_z \left(c_{\vec{k}\uparrow}^\dagger c_{\vec{k}\uparrow} - c_{\vec{k}\downarrow}^\dagger c_{\vec{k}\downarrow} \right) + s_+ c_{\vec{k}\uparrow}^\dagger c_{\vec{k}\downarrow} + s_- c_{\vec{k}\downarrow}^\dagger c_{\vec{k}\uparrow} \right], \quad (2.1)$$

with $c_{\vec{k}\sigma}^{(\dagger)}$ the annihilation(creation) operator of the band electron of momentum \vec{k} and spin projection σ , s_z the spin projection operator of the local moment, and s_+ and s_- the raising and lowering operators of the local moment's spin. This is known as the $s - d$ model[19].

Since both the impurity and the band spin projections (s_z and S_z , respectively) are good quantum numbers, an incoming electron from the metallic band will scatter off the magnetic impurity with non-zero probability only between states that preserve both numbers. This, however, does not forbid transitions to states with different numbers as intermediate states in perturbation theory. The Feynman diagram in Fig. 2.2 represents this possibility to lowest order in the perturbative expansion.

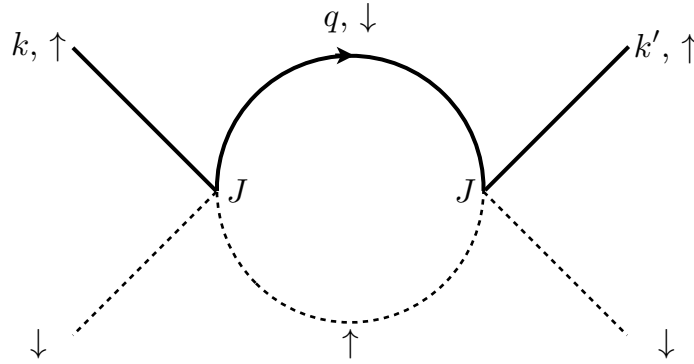


Figure 2.2: Feynman diagram for the $s - d$ model up to second order in perturbation theory. The solid line represents the band electronic state, and the dashed line represents the impurity.

The amplitude for the diagram of Fig. 2.2 is given by

$$P_{\vec{k}, \vec{k}'} \sim \frac{\langle \vec{k}, \uparrow; \downarrow | H_{sd} | \vec{q}, \downarrow; \uparrow \rangle \langle \vec{q}, \downarrow; \uparrow | H_{sd} | \vec{k}', \uparrow; \downarrow \rangle}{\varepsilon_k - \varepsilon_q}, \quad (2.2)$$

where \vec{k} and \vec{k}' are the momenta of the electron in the final and initial states, respectively.

Let us simplify the calculation by assuming that the coupling is independent of momentum, *i.e.*, $J_{\vec{k},\vec{q}} = J_{\vec{q},\vec{k}'} = J$, and sum over all possible intermediate momenta q .

Introducing the density of states $\rho(\varepsilon)$ we obtain

$$P_{\vec{k},\vec{k}'} \sim J^2 \int dq \frac{1 - f_{FD}(\varepsilon_q)}{\varepsilon_k - \varepsilon_q} = J^2 \int d\varepsilon \frac{1 - f_{FD}(\varepsilon)}{\varepsilon_k - \varepsilon} \rho(\varepsilon), \quad (2.3)$$

with $f_{FD}(\varepsilon)$ the Fermi–Dirac distribution. If the intermediate state is occupied, the Pauli principle forbids the transition, so we multiply by the term $(1 - f_{FD}(\varepsilon))$ which gives the probability that the state is empty. Assuming a constant density of states and working at zero temperature, all states below the Fermi level ε_F are occupied, whereas the states above are empty. Assuming a half bandwidth of D , Eq. (2.3) becomes

$$P_{\vec{k},\vec{k}'} = J^2 \rho \int_{\varepsilon_F}^D \frac{d\varepsilon}{\varepsilon_k - \varepsilon} = J^2 \rho \log \left| \frac{\varepsilon_k - \varepsilon_F}{\varepsilon_k - D} \right|, \quad (2.4)$$

and the logarithmic term appears. Also, at finite temperature T we have $\langle |\varepsilon_k - \varepsilon_F| \rangle \sim T$, and we can draw a simple conclusion from Eq. (2.4): considering that the resistance is inversely proportional to the transmission probability that we just calculated, it must be that

$$R(T) \sim -\log T. \quad (2.5)$$

This is the result obtained by Kondo[18].

The origin of the divergence is clearly the degeneracy of the spin–up and spin–down states of the local moment: if this degeneracy were broken— say, $E(k, \downarrow) = E(k, \uparrow) + \Delta$ — the intermediate state in the diagram of Fig. 2.2 would contribute a term proportional to $(\varepsilon_k - \varepsilon_q - \Delta)^{-1}$, yielding a converging integral in Eq. (2.2).

A divergence coming from a small, additive correction to the free Hamiltonian representing the free local moment and the Fermi sea of the metal is, of course, not physically sound. As verified by Kondo himself, higher–order diagrams produce terms

that further contribute to the divergence, rather than correct it: a clear signal that this seemingly innocent model cannot be handled with perturbative techniques.

As puzzling as these results were at the time, nowadays the origins of the Kondo problem are very well understood: in order for a perturbative treatment to be valid, the power series expansion of the spin–spin interaction must be centered “close” to the true ground state of the system. The calculation shown above assumes that the true ground state will be the Fermi sea of the metallic leads, slightly deformed by the impurity degrees of freedom, when in reality the presence of the spin–spin interaction leads to a qualitatively different ground state[23].

Throughout this document we will present several non–perturbative methods of solution that give different insights into the physics of this problem. We will focus particularly on a technique contributed by Kenneth G. Wilson in 1975[24], based on the *Renormalization group* (RG): a general field–theoretical method developed by himself which to date is used in most areas of physics, from condensed matter to particle physics¹.

2.3 The Kondo effect in nanostructures

After Kondo’s analysis of the $s - d$ model, the Kondo problem became increasingly well understood. Wilson’s RG[24] proved to be a robust tool for calculations of thermodynamic properties of this and similar models, and in 1980 a fully analytical method of diagonalization was found by P. B. Wiegmann[25], and independently by N. Andrei[26]. Nevertheless, the topic was never put to rest: with the rapid advance of sample fabrication techniques, interest in the Kondo effect was rekindled in the late 90’s, as signatures of the Kondo effect were observed in single–electron devices and in magnetic atoms on surfaces, rather than bulk samples.

¹ We discuss the RG in Chapter 3.

Experiments on the Kondo effect in a single–electron transistor were pioneered by D. Goldhaber–Gordon, *et al.*[4] Through deposition of metallic leads on top of an GaAs/AlGaAs heterostructure, they were able to produce a “droplet” consisting of a few electrons, which leaks onto the 2–dimensional electron gas (2DEG) in the heterostructure. The experimental setup is shown in Figure 2.3(a): the top and bottom metal contacts on the left, as well as the shaped contact on the right, produce a confining potential that traps a small number of electrons in the intermediate region. The central contact on the left produces a gate voltage that can raise or lower the localized electronic levels within the droplet.

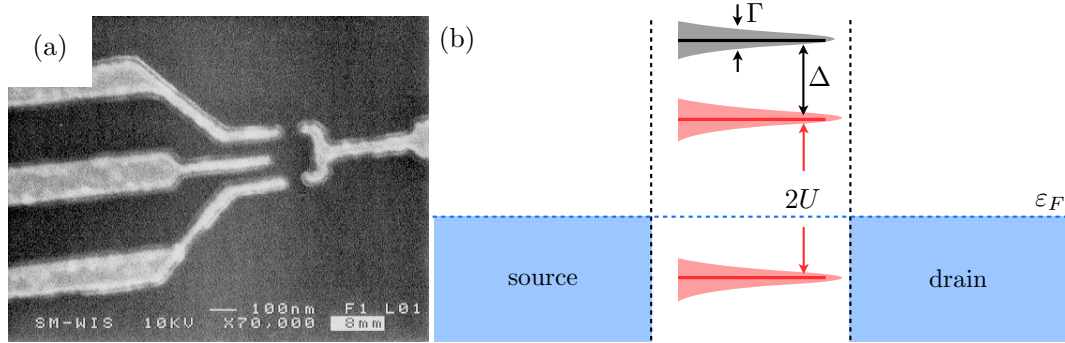


Figure 2.3: (a) Scanning electron microscope image of a SET. The top–left, bottom–left and right contacts produce a confining potential for the central region, whereas the central contact on the left provides a gate voltage. The SET is fabricated by deposition of metallic contacts on a GaAs/AlGaAs heterostructure (extracted from Ref. [4], with permission of Nature Publishing Group). (b) Energy level structure of the central region. The splitting $2U$ between single and double occupation of the lower state (red) comes from Coulomb interactions; higher (black) and lower energy states (not shown) can be accessed by changing the gate voltage. Hybridization with the 2DEG in the heterostructure produces a broadening Γ of the levels.

The small confining region contains widely–spaced electronic levels. In addition, the small size and low electronic density make electron–electron interactions more important, introducing an energy cost of $2U$ for double occupation of a single electron level, where

$U \sim e^2/(2C)$, with C the capacitance of the droplet. This level structure is shown in Fig. 2.3(b), where the level marked in red is split between single and double occupation, and there is a spacing Δ between double occupation of the lower level, and the next single-electron state within the droplet. The leaking of the droplet onto the 2DEG produces a broadening Γ for each level. Typical values in heterostructures are $U \sim 1\text{meV}$, $\Gamma \sim 0.1\text{meV}$; the reported values for this experiment in particular are reported to be $\Gamma \approx 0.2\text{ meV}$ and U between 0.6 and 2.0 meV.

Figure 2.3(b) depicts a situation in which the single occupation level is below the Fermi level of the 2DEG, while the double occupation level is above. The separation $2U \gg \Gamma$, so that at low temperatures the system is in a Coulomb blockade regime; that is, electrons cannot tunnel into the droplet due to the high energy cost of double occupation, and so they cannot get from source to drain. The zero-bias conductance $G = dI_{sd}/dV_{bias}|_{V_{bias}=0}$ is expected to be zero, unless a gate voltage shifts the levels until one coincides with ε_F up to a difference of order Γ . Surprisingly, the experimental measurements show that this is not the case.

Figures 2.4(a) and (b) show conductance measurements as a function of the gate voltage at different temperatures, and Fig. 2.4(c) shows the same measurements for a reduced broadening, Γ . As expected, conductance peaks appear when a level within the droplet is aligned with the Fermi level of the 2DEG ($V_g \approx -80\text{mV}$, -60mV), but contrary to expectations, the conductance does not vanish between some pairs of peaks, although it does vanish between others (*e. g.*, V_g between -60mV and -40mV). This anomalous enhancement of the conductance cannot be attributed to the level broadening or the temperature, which are significantly smaller than the level separation ($0.0078\text{ meV} \leq T \leq 0.069\text{meV}$, *vs.* $U \approx 0.6\text{ meV}$ and $\Gamma \approx 0.2\text{ meV}$). It is also clear from

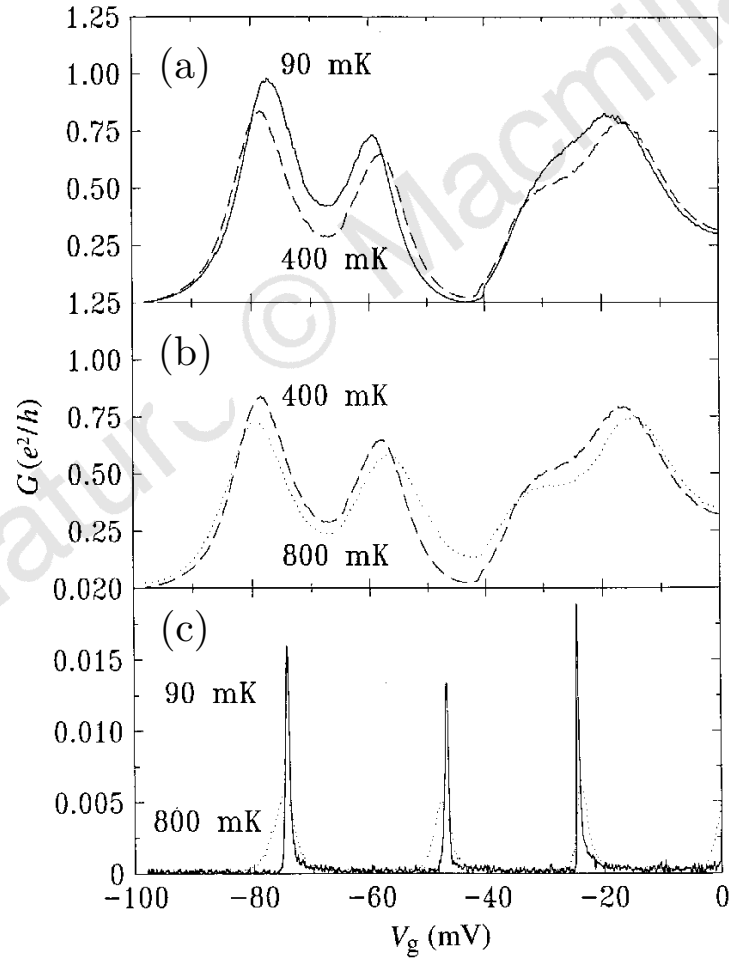


Figure 2.4: Zero-bias conductance measurements of the SET, as a function of gate voltage. (a) and (b) Measurements for constant $\Gamma \ll U$, for temperatures from 90mK to 800mK. An anomalous enhancement of the conductance is observed between the first and second peaks, from left to right, but not between the second and third. (c) Measurements for reduced Γ , achieved by tuning the confining voltage, for temperatures from 90mK up to 800mK. No anomalous enhancement of the conductance between resonances is observed. (Extracted from Ref. [4], with permission of Nature Publishing Group)

Fig. 2.4(c) that reducing the broadening can destroy the effect, at least for the temperature range of the measurements.

The reason for this enhancement of the conductance is the onset of the Kondo effect. For the parameters at hand, the lower electronic level is singly occupied on average, due to

the high ($U \gg \Gamma$) energy cost of double occupancy. This leaves a single electron whose spin is a localized magnetic moment that can interact with the electrons in the 2DEG in the same fashion as we described in Section 2.2. The Kondo ground state is characterized by a peak in the local density of states of the droplet exactly at $\varepsilon = \varepsilon_F$ (see Section 3.3), breaking the Coulomb blockade and enhancing the conductance. Thus, the region between $V_g = -0.8mV$ and $V_g = -0.6mV$ corresponds to single (or odd) occupancy of the electronic level within the droplet, where the Kondo effect can take place, and the region between $V_g = -0.6mV$ and $V_g = -0.4mV$ to double (or even) occupation, where no enhancement of the conductance is observed.

The quenching of the Kondo effect by reducing the level broadening still requires justification. As mentioned in Section 2.1, the resistance minimum produced by the Kondo effect in the bulk is associated with a temperature scale T_K , called the Kondo temperature. At $T < T_K$, the behavior of the system is dominated by the Kondo effect, whereas for $T > T_K$ the effect is quenched. In 1965, A. A. Abrikosov estimated T_K as [27]

$$T_K \sim D \exp \left\{ -\frac{1}{2\rho(\varepsilon_F)J} \right\}, \quad (2.6)$$

with $\rho(\varepsilon_F)$ the density of states of the metal at the Fermi level. Later, in 1966, J. R. Schrieffer and P. A. Wolff established a relation between the Kondo coupling and the broadening Γ between the localized magnetic moment and the electronic band for a case analogous to the one discussed in this section. [28] The relation is

$$J \sim D\Gamma \frac{U}{\varepsilon_d(\varepsilon_d + U)}. \quad (2.7)$$

From Eqs. (2.6) and (2.7) we find that $T_K \sim \exp\{-\Gamma^{-1}\}$, which vanishes as Γ goes to zero, justifying the absence of the enhanced conductance in Fig. 2.4(c).

The SET in the experiments of Goldhaber-Gordon's is an example of a quantum dot (QD): an artificial nanostructure with an atomic-like, discrete electronic structure.

Research on the Kondo effect in QDs continued to gain momentum: Cronenwett *et al.*

successfully tuned the ground state of a QD into and out of the Kondo phase, and controlled the Kondo temperature by means of a gate voltage[29]. Sasaki *et al.* observed a spin-1 Kondo effect in AlGaAs/InGaAs heterostructures in a stacked (as opposed to lateral) QD configuration.

The Kondo effect is by no means exclusive to quantum dots. Iancu *et al.* observed the Kondo effect on TBrPP-Co molecules deposited on a Cu(111) surface, and tuned the Kondo temperature by switching the molecular configuration on (and thus their hybridization to) the metallic surface through voltage pulses with an scanning electron microscope.[9, 10] Roch *et al.* fabricated a single-molecule transistor with a C_{60} molecule by means of electromigration, whose ground state could be tuned by means of a gate voltage between a spin-1 triplet and a spin-0 singlet.[7] Coupled to Al/Al₂O₃ leads, this led to the observation of a quantum phase transition (QPT) to and from a Kondo ground state. More recently, Parks *et al.* observed an underscreened Kondo effect on a spin-1 Co atom, embedded in a stretchable octahedral molecule in a break junction configuration. Stretching of the molecule produced a magnetic anisotropy, through which the ground state could be tuned into and out of the Kondo regime.[8]

Be it QDs, individual molecules, quantum point contacts, carbon nanotubes, etc., the Kondo effect plays a fundamental role in the low-temperature behavior of complex nanostructures.

3 WILSON'S NUMERICAL RENORMALIZATION GROUP

3.1 Renormalization group theory

3.1.1 Introduction

The renormalization group (RG) method appears naturally in the study of critical phenomena. In the vicinity of a second order (continuous) phase transition, the main thermodynamic quantities diverge as power laws; the associated exponents are known as critical exponents, and obey certain relations that imply that they are not independent from each other[30].

A particularly important quantity is the correlation length ξ of the order parameter—the physical quantity that distinguishes between different phases, usually changing from zero to a finite value as a phase transition occurs—, which gives the maximum length scale at which correlations are important. In a d -dimensional Ising spin system close to its critical point described by the reduced temperature $t = (T - T_C)/T_C$ and the magnetic field h , for example, the correlation length diverges as² $\xi \sim 1/h^\nu$ at $t = 0$. This means that in this regime fluctuations at all length scales are important for the correct description of the system, making all types of mean-field approaches—which rely on the existence of a length scale, above which correlations can be ignored—unsuitable.

Another known result from the theory of critical phenomena is that the relevant thermodynamic quantities near criticality are homogeneous functions of t and h . Furthermore, the correlation function of the order parameter is known to be a homogeneous function of position near criticality, that is

$$G_{mm}^c(\lambda x) = \lambda^p G_{mm}^c(x), \quad (3.1)$$

² The value of the critical exponent ν depends on the dimensionality d . For $d \geq 4$ the mean-field theory value is $\nu = 1/2$, and in general it can be related to the critical exponent α , with $\xi \sim t^{-\alpha}$, by the Josephson scaling law $2 - \alpha = \nu d$. See Ref. [30] for further details.

with λ and p independent of x . This relation implies an underlying symmetry under change of scale: a self-similarity of the system at different length scales. Suppose taking advantage of these two facts: utilizing the self-similarity of the correlation function at different scales to eliminate the correlated degrees of freedom of the system up to ξ , and then be left with an uncorrelated system, describable up to length scales larger than ξ . This scheme was proposed by L. Kadanoff[31] in three steps: a systematic coarse graining of the system, a rescaling and a renormalization of the relevant quantities.

3.1.2 The renormalization group transformation

We present the formalism leading to a RG transformation in terms of a specific example, following reference [24]. Consider a spin lattice defined by $\{s_n\}$; that is, at each lattice point \vec{x}_n there is a spin degree of freedom $s_n = \pm 1$. As mentioned in Section 3.1.1, the first step in the RG program is to coarse-grain the lattice by averaging the order parameter—in this case, the magnetization $m(\vec{x})$ —over a region of size L of the order of a few lattice constants. We do so by defining the conjugate field

$$m(\vec{k}) := \sum_{\vec{x}_n} \exp \{ i\vec{k} \cdot \vec{x} \} s_n, \quad (3.2)$$

and then averaging as

$$m(\vec{x}) = \int_0^\Lambda \frac{d^3k}{(2\pi)^3} \exp \{ -i\vec{k} \cdot \vec{x} \} m(\vec{k}), \quad (3.3)$$

where we have defined the cutoff wave vector $\Lambda = 2\pi/L$. Integrating up to Λ we average only the short wavelength fluctuations, producing an average magnetization that describes the system well at wavelengths larger than $2\pi/\Lambda$.

All statistical averages at temperature T are calculated by means of the partition function

$$Z := \sum_{\{s_n\}} \exp \{ -\beta H(s_n) \}, \quad (3.4)$$

where $\sum_{\{s_n\}} = \sum_{s_1} \sum_{s_2} \cdots$, is a sum over all possible configurations of the spins, and $\beta = 1/T$. This can be put in terms of the magnetization Eq. (3.3) as

$$Z = \prod_{k=0}^{\Lambda} \int dm(\vec{k}) \exp\{H_{\Lambda}(m)\}, \quad (3.5)$$

where the integrals are over the possible values that each magnetization component $m(\vec{k})$ can take, and the multiplication should be interpreted as

$$\prod_{k=k_1}^{k_N} \int dm(\vec{k}) = \int dm(\vec{k}_1) \cdots \int dm(\vec{k}_N).$$

Formally, this can be done by fixing the total magnetization of $m(\vec{k})$ in each Boltzmann factor as

$$\exp\{-\beta H_{\Lambda}(m)\} = \sum_{\{s_n\}} \left[\prod_{k=0}^{\Lambda} \delta \left(m(\vec{k}) - \sum_{\vec{x}_n} \exp\{i\vec{k} \cdot \vec{x}\} s_n \right) \right] \exp\{-\beta H(s_n)\}. \quad (3.6)$$

In the continuum limit the integral Eq. (3.5) becomes a functional integral over the conjugate field $m(\vec{k})$ in the form

$$Z = \int_{k=0}^{k=\Lambda} \mathcal{D}m(\vec{k}) \exp\{-\beta H_{\Lambda}(m)\}. \quad (3.7)$$

The central part of the expression Eq. (3.7) is the Boltzmann factor inside the integral, where the original Hamiltonian $H(s_n)$ has been replaced by a free energy H_{Λ} dependent on a field $m(\vec{k})$, in the same fashion as Landau–Ginzburg theory[32]. Suppose now that the same procedure were performed for a wave number $\Lambda/2$, say, instead of Λ . This would produce a functional $\exp\{-\beta H_{\Lambda/2}\}$ related to $\exp\{-\beta H_{\Lambda}\}$ by

$$\exp\{-\beta H_{\Lambda/2}\} = \int_{k>\Lambda/2}^{\Lambda} \mathcal{D}m(\vec{k}) \exp\{-\beta H_{\Lambda}\}, \quad (3.8)$$

such that the partition function would be given by

$$Z = \int_{k=0}^{k=\Lambda} \mathcal{D}m(\vec{k}) \exp\{-\beta H_{\Lambda/2}\}. \quad (3.9)$$

Equation (3.8) represents a renormalization group transformation. It can be put in terms of dimensionless variables by rescaling the wave vectors as $\vec{q} = \vec{k}/\Lambda$, and defining $m(\vec{k}) = z_\Lambda \sigma(\vec{q})$, where z_Λ is chosen so that $\sigma(\vec{q})$ can be of order one for all \vec{q} , regardless of the value of the corresponding $m(\vec{k})$. The rescaling of the dimensionless variables is clearly different for different values of Λ , and so the field $\sigma(\vec{q})$ for cutoff Λ and the field $\sigma'(\vec{q})$ for $\Lambda/2$, are different. For consistency, they must be related to each other by the condition

$$z_\Lambda \sigma(\vec{q}) = z_{\Lambda/2} \sigma'(2\vec{q}), \quad (3.10)$$

and the ratio $R = z_{\Lambda/2}/z_\Lambda$ determines the renormalization of the field due to successive RG transformations; equation (3.10) is the mathematical statement the self-similarity mentioned above. Equation (3.8) can be rewritten as

$$\exp\{-\beta H_{\Lambda/2}(\sigma')\} = \int_{q < 1/2}^1 \mathcal{D}\sigma(\vec{q}) \exp\{-\beta H_\Lambda(\sigma)\}, \quad (3.11)$$

where the functional differential has been redefined ($\mathcal{D} \rightarrow D$) to account for the change of variables.

3.1.3 Fixed points

The RG transformation maps the free energy H_Λ into a new, effective free energy $H_{\Lambda/2}$ that describes the system at length scales twice as large. The condition Eq. (3.10) can be interpreted in a very simple manner: assume an initial free energy along the lines of Landau–Ginzburg theory; that is, one that respects all the symmetries of the original

Hamiltonian. Specifically, suppose that the free energy is given by a field integral such as³

$$\int_0^\Lambda \frac{d^d q}{(2\pi)^d} \left(\frac{t + Kq^2 + Lq^4 + \dots}{2} \right) m^2(\vec{q}) - hm(0). \quad (3.12)$$

The partition function can be coarse grained by eliminating fluctuations between length scales $2\pi/\Lambda$ and $2\pi/(\Lambda/2)$, or between wave numbers $\Lambda/2$ and Λ , by separating the functional differential as $\{m(\vec{q})\} \rightarrow \{\sigma(\vec{q}^>)\} \oplus \{m(\vec{q}^<)\}$, with $\{\sigma(\vec{q})\}$ corresponding to the smaller Fourier modes. The partition function is

$$Z = \int \mathcal{D}\sigma(\vec{q}^>) \int \mathcal{D}m(\vec{q}^<) \exp \{-\beta H(\sigma, m)\}. \quad (3.13)$$

The Gaussian form of the free energy allows us to decouple both fields, and the functional integration over the field σ can be performed directly, yielding

$$Z \sim \int \mathcal{D}m(\vec{q}) \exp \left\{ - \int_0^{\Lambda/2} \frac{d^d q}{(2\pi)^d} \left(\frac{t + Kq^2 + Lq^4 + \dots}{2} \right) m^2(\vec{q}) + hm(0) \right\}. \quad (3.14)$$

We now rescale the wave numbers to restore the exact same range of integration of Eq. (3.12) and obtain

$$Z \sim \int \mathcal{D}m(\vec{q}) \exp \left\{ - \int_0^\Lambda \frac{d^d q}{(2\pi)^d} b^{-d} \left(\frac{t + Kb^{-2}q^2 + Lb^{-4}q^4 + \dots}{2} \right) m^2(\vec{q}) + hm(0) \right\} \quad (3.15)$$

The extra factors can be absorbed into the coupling constants as

$$\begin{aligned} t &\rightarrow z^2 b^{-d} t, \\ h &\rightarrow zh, \\ K &\rightarrow z^2 b^{-(d+2)} K, \\ L &\rightarrow z^2 b^{-(d+4)} L. \end{aligned} \quad (3.16)$$

³ The introduction of Eq. (3.12) requires some justification. A typical Landau–Ginzburg free energy for this kind of system is the Gaussian model

$$\int d^d x \left(\frac{t}{2} m^2 + \frac{K}{2} (\nabla m)^2 + \frac{L}{2} (\nabla^2 m)^2 + \dots - \vec{h} \cdot \vec{m} \right),$$

with \vec{h} the external magnetic field. Eq. (3.12) is the same free energy in terms of the Fourier modes of the field $m(\vec{x})$. For further details see Ref. [33], Section 4.6.

where we have defined a rescaled magnetization $m(\vec{q}) \rightarrow m(\vec{q})/z$ (recall the definitions of z_Λ and $z_{\Lambda/2}$). We say that the couplings are *renormalized*, and subsequent transformations will produce a *flow* of the values of the couplings. It is possible, however, that the free energy be mapped into an identical form

$$\exp\{-\beta H^*\} = \int_{k>\Lambda/2}^{\Lambda} \mathcal{D}m(\vec{k}) \exp\{-\beta H^*\}, \quad (3.17)$$

with the exact same coupling constants. When this happens, we say we are in a *fixed point*. The importance of these points cannot be overemphasized: the fact that the free energy maps onto itself under a change of scale is an indication of the self similarity discussed in Sec. 3.1.1. In this way, a fixed point indicates that the free energy describes the system at a critical point.

Near a fixed point, the system may be described in terms of the fixed–point free energy, plus a small deviation, δH . Techniques of perturbation theory may be used to understand whether the couplings will flow toward the fixed point or away from it, and also how “fast” this will happen. In the former case, the operator is called an *irrelevant operator*, and in the latter it is called a *relevant operator*. When neither case is true, the operator is called *marginal*, and a perturbative treatment is not suitable for the description of the problem. We will not discuss here the details of fixed–point perturbation theory, but the reader may find a formal treatment in Ref. [34]. We will, however, work out a practical application of RG methods to the $s - d$ model, which is directly useful for the understanding of Kondo physics.

3.1.4 Poor man’s scaling of the $s - d$ model

To better understand how the RG flow of the coupling constants can give us information about the behavior of a system of this kind, we treat a simple example where the concepts are used without strictly following the methodology. The poor man’s scaling method was introduced by P. Anderson to treat the $s - d$ model introduced in Chapter 2—

which corresponds to a specific regime of the Anderson impurity model[28]—, as he recognized that, just as in the case of a critical point, correlations are of fundamental importance to the description of the Kondo effect.[35].

The Hamiltonian for the $s - d$ model is⁴

$$H_{s-d} = \sum_{\vec{k}\sigma} \epsilon_k c_{\vec{k}\sigma}^\dagger c_{\vec{k}\sigma} + \frac{J_\pm}{2} (S_+ s_- + S_- s_+) + J_z S_z s_z, \quad (3.18)$$

with the electronic operators $c_{\vec{k}\sigma}$ and $c_{\vec{k}\sigma}^\dagger$ corresponding to a metallic band, and the band spin operators defined as $S_i = \sum_{\vec{k}\mu\mu'} c_{\vec{k}\mu}^\dagger \sigma_{\mu\mu'}^i c_{\vec{k}\mu'}$, with σ^i the Pauli matrices. The lower-case counterparts correspond to a quantum impurity —historically an atomic d -level—, and the spin-flip operators are defined as $s_\pm = s_x \pm i s_y$. The non-diagonal part will be grouped in a term V_{imp} .

The standard method of solution would be to solve the Dyson equation for the Green's function, or alternatively for the T -matrix:

$$T = V_{\text{imp}} + G_0 V_{\text{imp}} T, \quad (3.19)$$

with the free-electronic resolvent Green's function

$$G_0 = \left[\omega - \sum_{\vec{k}\sigma} \epsilon_k c_{\vec{k}\sigma}^\dagger c_{\vec{k}\sigma} \right]^{-1}. \quad (3.20)$$

We assume that ω is limited to an electronic band from energy $-D$ to D , and we proceed to decimate its degrees of freedom systematically, to produce subsequent effective Hamiltonians that describe the system at progressively lower energies. This procedure is not arbitrary: it was proposed by Anderson on the assumption that it is the lowest energy degrees of freedom which matter most in the highly correlated regimes of the Hamiltonian Eq. (3.18).

⁴ This definition of the $s - d$ model differs from that of Eq. (2.1) in that momentum scattering is ignored. This simplified version of the $s - d$ model is the minimal form that produces the Kondo effect, as it contains all the relevant spin-flip correlations.

The decimation is as follows: we eliminate the degrees of freedom of energy in the ranges $[-D, -D + \Delta]$ and $(D - \Delta, D]$ —where clearly Δ plays the role of the cutoff Λ —by means of a projection operator P_Δ that projects onto the sector of the many-body Hilbert space where these states lie. Equation (3.19) becomes

$$T = V_{\text{imp}} + V_{\text{imp}} P_\Delta G_0 T + V_{\text{imp}} (1 - P_\Delta) G_0 T, \quad (3.21)$$

and with the substitution of the Dyson equation again, but only in the second term, we obtain

$$\begin{aligned} T &= V_{\text{imp}} + V_{\text{imp}} P_\Delta G_0 (V_{\text{imp}} + V_{\text{imp}} [P_\Delta + (1 - P_\Delta)] G_0 T) \\ &\quad + V_{\text{imp}} (1 - P_\Delta) G_0 T \\ &= (V_{\text{imp}} + V_{\text{imp}} P_\Delta G_0 V_{\text{imp}}) + V_{\text{imp}} P_\Delta G_0 V_{\text{imp}} P_\Delta G_0 T \\ &\quad + (V_{\text{imp}} + V_{\text{imp}} P_\Delta G_0 V_{\text{imp}}) (1 - P_\Delta) G_0 T \\ &= V' + V' (1 - P_\Delta) G_0 T + \dots, \end{aligned} \quad (3.22)$$

with the definition

$$V' = V_{\text{imp}} + V_{\text{imp}} P_\Delta G_0 V_{\text{imp}}. \quad (3.23)$$

Pursuing an effective Hamiltonian to second order in V_{imp} , we disregard the term $V_{\text{imp}} P_\Delta G_0 V_{\text{imp}} P_\Delta G_0 T$ because support for this term comes from only the states within the decimated regions with a magnitude proportional to $\rho^2(D)\Delta^2$, which can be made arbitrarily small through Δ . Thus, up to order Δ^2 , we have obtained the exact same form for the Dyson equation, and consequently the effective Hamiltonian has the exact same functional form as the original one, with a renormalized interaction V' . The change in the interaction operator is given by

$$dV_{\text{imp}} = V' (1 - P_\Delta) G_0 V_{\text{imp}}, \quad (3.24)$$

and this will clearly reflect itself in the coupling constants J_\pm , J_z . Expressing dV_{imp} in terms of the electronic operators and the coupling constants is a relatively lengthy

algebraic process, and so we will not present it here. The interested reader can find the details in Anderson's own words in Ref. [35]. We simply state the main results of this analysis: first, that dV_{imp} leads to a shift in the ground state energy of the system

$$\delta E_{\text{gnd}} \approx \log 2 \int_{-D}^D d\omega \left(\frac{(J_z \rho(\omega))^2}{8} + \frac{(J_{\pm} \rho(\omega))^2}{4} \right), \quad (3.25)$$

and second, that a spin-flip term is produced with the same form as the original interaction term in the Hamiltonian:

$$\begin{aligned} dV_1 = & \frac{\rho(\omega)\Delta}{\omega - D + \delta E_{\text{gnd}}} \\ & \times \sum_{\vec{k}\mu} \sum_{\vec{l}\nu} c_{\vec{k}\mu}^{\dagger} \left[-J_{\pm}^2 (S_z s_z)_{\mu\nu} - \frac{J_{\pm} J_z}{2} (S_+ s_- + S_- s_+)_{\mu\nu} \right] c_{\vec{l}\nu}, \end{aligned} \quad (3.26)$$

from which the following flow equations can be obtained:

$$\frac{dJ_z}{dD} = -\frac{\rho}{\omega - D + \Delta} J_{\pm}^2, \quad (3.27a)$$

$$\frac{dJ_{\pm}}{dD} = -\frac{\rho}{\omega - D + \Delta} J_z J_{\pm}. \quad (3.27b)$$

Notice that the “coarse graining” in this case consists in reducing the half bandwidth D .

That explains the meaning of the derivatives in Eqs. (3.27). Dividing one by the other, and integrating over the bandwidth, we obtain the condition $J_z^2 - J_{\pm}^2 = \text{const}$. These results can be presented in the form of a flow, as shown in Fig. 3.1. The flow of the couplings can be

understood as follows: for $J_{\pm}^2 - J_z^2 < 0$, when $J_z < 0$, the spin-flip coupling flows to zero, and the diagonal coupling flows to a finite value. We thus enter a ferromagnetic regime indicated as *ferromagnetic Kondo*. All other cases flow toward large values of both J_z and J_{\pm} , where the approximation in the scheme becomes progressively less accurate. This may be seen as a problem of the method, but qualitatively it does reveal the flow toward strong coupling that culminates in the *antiferromagnetic Kondo* regime. Particularly, along the line $J_{\pm}^2 - J_z^2 = 0$ the usual (isotropic) Kondo effect arises. We focus in the latter two regimes.

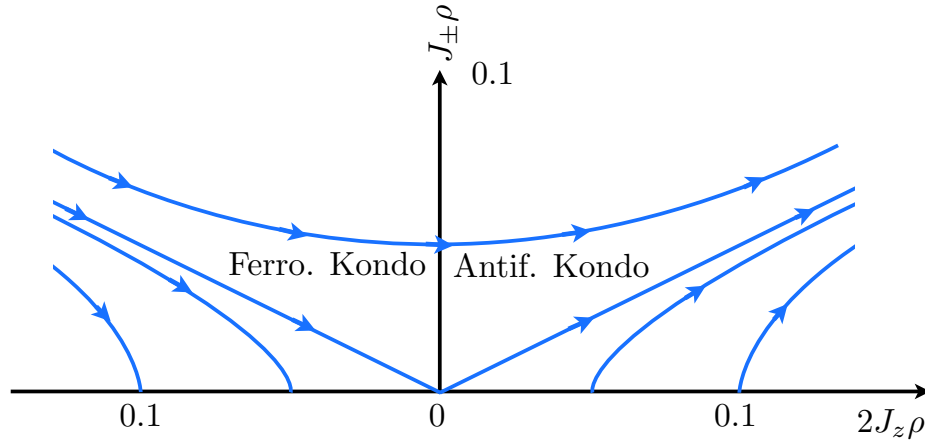


Figure 3.1: Flow of the coupling constants of the s-d model, obtained through Anderson's poor man's scaling RG scheme. Arrows indicate the flow of the coupling constants J_z , J_{\pm} with subsequent transformations, starting from any point in the plane. Four regimes are shown in the picture: two corresponding to the sign of J_z , and two for each of these, above and below the diagonals. Below the diagonals, the coupling J_{\pm} flows to zero for both signs of J_z , whereas above the couplings flow toward (positive) strong coupling. For further details, see Ref. [35].

The subsequent transformations can be interpreted as effective Hamiltonians, valid whenever the only relevant energy scales are those within the ever-decreasing bandwidth. The relevance of an energy scale E is weighed by its Boltzmann factor $\exp\{-E/T\}$, which is negligible if the energy is much larger than the temperature, and thus at temperatures $T \ll D$ (variable D , changing with subsequent transformations) the transformed Hamiltonian describes the system correctly. In the limit of low temperatures—that is, after many transformations—the couplings flow toward large values, making any other energy scale irrelevant, and the system can effectively be described by a pair of spins—one of which is the electronic band—locked in a singlet state. The degrees of freedom are significantly reduced by virtue of the strength of the couplings, and we have a reliable picture of the behavior of the system at zero temperature.

Many other results for the physics of the Kondo effect will be presented, but we will do it in terms of a more accurate calculation tool: the *numerical renormalization group*.

3.1.5 Summary

This discussion of the RG method may seem scattered and confusing. Our purpose here was to introduce the ideas of the method and some of its variations, and how versatile it can be to fit different kinds of field theories. There is, of course, a standard RG method for quantum field theories. The reader may consult Ref. [36], chapter 8, and Ref. [37], chapter 28, and references therein.

In the following we will focus on yet another scheme: Wilson's numerical renormalization group method. This is specialized to the treatment of quantum impurity systems, and along with its many variations it is arguably the *ultimate* tool for the study of Kondo physics.

3.2 The numerical renormalization group

In this section we develop the central calculation tool that we utilized for the results presented in subsequent chapters. We will be as thorough as possible in presenting the formalism, but the reader should know that the method, while very powerful and robust, is not devoid of subtleties that may require further reading in order to be understood. We refer the reader interested in going more in depth into the subject to the following references: the basic formalism of the numerical renormalization group, as well as the precise connection between this formalism and the one presented in Sec. 3.1.2, is best presented in Ref. [24]. This review, by K. Wilson himself, presents the basic method for the Kondo model in the case of an impurity with only spin degrees of freedom, coupled to an electronic band with a flat density of states. The corresponding treatment for the Anderson model is presented in Refs. [38] and [39]. Further developments that include a

metallic band with an arbitrary density of states can be found in the review by R. Bulla *et al.*, Ref. [40].

Calculations regarding electronic transport through the quantum impurity depend mainly on the spectral density of the impurity site. In order to calculate this dynamic quantity we follow the methods presented in Ref. [41].

3.2.1 Mapping the Anderson model onto a tight-binding chain

This formalism regards the Anderson Hamiltonian with the generic form

$$H_A = H_{imp} + \sum_{\vec{k}\sigma} \varepsilon(k) c_{\vec{k}\sigma}^\dagger c_{\vec{k}\sigma} + \sum_{\vec{k}\sigma} \left\{ V_{\vec{k}} d_\sigma^\dagger c_{\vec{k}\sigma} + V_{\vec{k}}^\dagger c_{\vec{k}\sigma}^\dagger d_\sigma \right\}. \quad (3.28)$$

The terms in the Hamiltonian are as follows: the operators $c_{\vec{k}\sigma}$ and $c_{\vec{k}\sigma}^\dagger$ are fermionic operators corresponding to electronic states in the band, of momentum \vec{k} and spin projection σ ; the dispersion $\varepsilon(k)$ gives the energy of the states of momentum \vec{k} , and its only restriction is that it may only depend on the magnitude k . The coupling $V_{\vec{k}}$ is given by the overlap of the impurity state $\psi_{d\sigma}(\vec{x})$ — typically a d -level, which can be distinguished from the band s -states by angular momentum— with the momentum state $\phi_{\vec{k}\sigma}(\vec{x})$, and for simplicity we will assume it to be independent of momentum: $V_{\vec{k}} = V$. There is plenty of freedom for the form of the impurity Hamiltonian, H_{imp} , but in the present form it is required that it only couple to the band through a single state (two, counting spin) represented by the operators d_σ and d_σ^\dagger . This is not a fundamental restriction, but it will be the case in our calculations.

One important feature of H_{imp} is that it includes an energy cost U_i for double occupancy in the i -th level of the impurity in the Hubbard form $U_i n_{i\uparrow} n_{i\downarrow}$. This interaction term is fundamental for the onset of electronic correlations that give rise to the Kondo effect. Let us, however, ignore this interaction and describe the influence of the band on the impurity through the self energy Σ ; specifically by its imaginary part, the hybridization

function $\Gamma(\omega)$ given by

$$\Gamma(\omega) := \pi \sum_{\vec{k}} V_{\vec{k}}^2 \delta(\omega - \varepsilon(k)) = \pi V^2 \sum_{\vec{k}} \delta(\omega - \varepsilon(k)). \quad (3.29)$$

Let us assume, like in Sec. 3.1.4, that the impurity only hybridizes to states of the band for energies between $-D$ and D . In the case of a flat band, $\rho(\omega) = 1/2D$, the hybridization function is simply the constant $\Gamma(\omega) = \pi V^2/2D$. Although this will be the case in our calculations in subsequent chapters, we will not introduce this restriction; instead, we follow R. Bulla *et al.* [42], in using instead a continuous Hamiltonian

$$H = H_{imp} + \sum_{\sigma} \int_{-D}^D d\epsilon g(\epsilon) a_{\sigma}^{\dagger}(\epsilon) a_{\sigma}(\epsilon) + \sum_{\sigma} \int_{-D}^D d\epsilon h(\epsilon) [d_{\sigma}^{\dagger} a_{\sigma}(\epsilon) + a_{\sigma}^{\dagger}(\epsilon) d_{\sigma}], \quad (3.30)$$

with the newly introduced dispersion $g(\epsilon)$ and coupling function $h(\epsilon)$. The operators $a_{\sigma}(\epsilon)$ and $a_{\sigma}^{\dagger}(\epsilon)$ are fermionic and obey the canonical relations

$$\{a_{\sigma}(\epsilon), a_{\sigma'}^{\dagger}(\epsilon')\} = \delta(\epsilon - \epsilon') \delta_{\sigma\sigma'}. \quad (3.31)$$

When one writes the path integrals for the Hamiltonians Eq(3.28) and Eq. (3.30), it can be shown that their actions are equivalent as long as the hybridization function, the continuous dispersion and the coupling function satisfy the equation

$$\Gamma(\omega) = \pi \frac{d\epsilon(\omega)}{d\omega} h^2[\epsilon(\omega)], \quad (3.32)$$

with the condition $g(\epsilon(\omega)) = \omega$ for all ω ; that is to say, g is the inverse function to ϵ . This allows some freedom for the functional forms of the coupling function; we will take advantage of this freedom to make the method suitable for an arbitrary form of the dispersion $\varepsilon(\omega)$, and in consequence of the density of states. In the flat-band case, for example, the choice $g(\omega) = \omega$ and $h(\omega) = \sqrt{\rho(\omega)}$ fulfills the requirement.

The central problem in solving the interacting Anderson Hamiltonian Eq. (3.30) consists of dealing with the interactions of each band state with the rest, through virtual

hopping processes to and from the impurity. Picture the hopping sequence of Figure 3.2: in a state in which the impurity is occupied by a single electron of spin \uparrow , the hopping term allows for a band electron of spin \downarrow to jump into the impurity with an energy cost of $\varepsilon_i + U_i$, followed by a subsequent relaxation back to single occupancy. Imagine now that the electron that leaves the impurity has spin projection \uparrow , effectively flipping the spin of the impurity. Consider now another electron from the band, with spin projection \downarrow . While it could have hopped into the impurity before the previous process, it is now forbidden by the Pauli exclusion principle, and this may be regarded as an indirect interaction between band states. Electronic correlations, to be more precise.

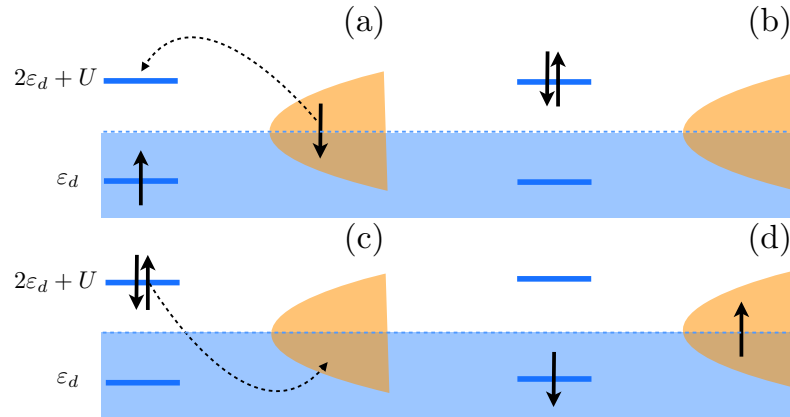


Figure 3.2: Virtual spin flip process in the interacting Anderson model. The levels represent many-body states of the impurity and their energies, rather than the single particle levels of the basis. (a) The initial state has the impurity occupied by a single electron, and an electron at the Fermi level of the band with opposite spin projection may hop into the impurity. (b) The impurity is doubly occupied, and (c) it may relax to single occupation by moving either electron into the band. (d) Depending on which electron goes to the band, the impurity spin may be flipped effectively.

Attempts were made to handle the highly correlated nature of this Hamiltonian in different perturbative schemes[18]. These were plagued with infrared divergences, and while a fully analytic solution was eventually found[25, 26] in the local moment regime

(see below), it is difficult to generalize to more complex impurity structures. K. Wilson introduced a numerical renormalization group scheme based on the mapping of the electronic band into a chain of states with exponentially decreasing local energies and tight binding couplings. This mapping is achieved by discretizing the continuous band, assumed to go from $-D$ to D , by means of a parameter $\Lambda > 1$. The continuous range is divided into regions going from $D\Lambda^{-(i+1)}$ to $D\Lambda^{-i}$, with $i = 0$ to an arbitrarily large, positive integer, and introducing an effective fermionic state to represent the full range of states within this energy region. The discretized band is shown in Figure 3.3 for $\Lambda = 2$. From now on we utilize D as the unit of energy ($D \rightarrow 1$), and we set our reference at the band's Fermi level: $\varepsilon_F = 0$.

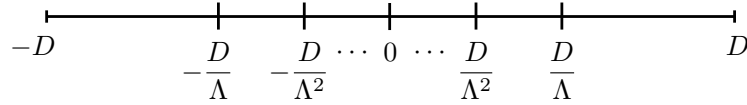


Figure 3.3: Logarithmic discretization used in the numerical renormalization group method, with discretization parameter $\Lambda = 2$.

Within each interval $x_n^- = [-\Lambda^{-n}, -\Lambda^{-(n+1)}]$ and $x_n^+ = [\Lambda^{-(n+1)}, \Lambda^{-n}]$, we define a full Fourier basis given by

$$\psi_{np}^+(\epsilon) = \begin{cases} \frac{1}{\sqrt{d_n}} \exp\{+i\omega_n p \epsilon\} & , \quad \epsilon \in x_n^+, \\ 0 & , \quad \text{otherwise} \end{cases} \quad (3.33a)$$

$$\psi_{np}^-(\epsilon) = \begin{cases} \frac{1}{\sqrt{d_n}} \exp\{-i\omega_n p \epsilon\} & , \quad \epsilon \in x_n^-, \\ 0 & , \quad \text{otherwise} \end{cases} \quad (3.33b)$$

where $\omega_n = 2\pi/d_n$, $d_n = \Lambda^n(1 - \Lambda^{-1})$ is the size of the n th interval, and p takes all integer values between $-\infty$ and ∞ . The electronic operators in $a_{\epsilon\sigma}$ in Eq. (3.30) can be expanded

in terms of the basis Eq. (3.33) as

$$a_{\epsilon,\sigma} = \sum_{n,p} \left\{ \psi_{np}^+(\epsilon) a_{np\sigma} + \psi_{np}^-(\epsilon) b_{np\sigma} \right\}, \quad (3.34)$$

and its respective Hermitian conjugate. Substituting into the Hamiltonian (3.30) we obtain:

$$\begin{aligned} \int_{-1}^1 d\epsilon h(\epsilon) \left(d_{\sigma}^{\dagger} a_{\epsilon\sigma} + a_{\epsilon\sigma}^{\dagger} d_{\sigma} \right) &= \sum_{np} \int_{-1}^1 d\epsilon h(\epsilon) \left[d_{\sigma}^{\dagger} \left(\psi_{np}^+ a_{np\sigma} + \psi_{np}^- b_{np\sigma} \right) \right. \\ &\quad \left. + \left(\left[\psi_{np}^+ \right]^* a_{np\sigma}^{\dagger} + \left[\psi_{np}^- \right]^* b_{np\sigma}^{\dagger} \right) d_{\sigma} \right]. \end{aligned} \quad (3.35)$$

At this point it is convenient to make $h(\epsilon) \rightarrow h_n$, a n -dependent constant, so that

$$\begin{aligned} \int_{-1}^1 d\epsilon h(\epsilon) \left(d_{\sigma}^{\dagger} a_{\epsilon\sigma} + a_{\epsilon\sigma}^{\dagger} d_{\sigma} \right) &= \sum_{np} \int_{-1}^1 d\epsilon \left[d_{\sigma}^{\dagger} \left(h_n^+ \psi_{np}^+ a_{np\sigma} + h_n^- \psi_{np}^- b_{np\sigma} \right) + \right. \\ &\quad \left. \left(h_n^+ \left[\psi_{np}^+ \right]^* a_{np\sigma}^{\dagger} + h_n^- \left[\psi_{np}^- \right]^* b_{np\sigma}^{\dagger} \right) d_{\sigma} \right] \\ &= \sum_{np} \sqrt{d_n} \left\{ d_{\sigma}^{\dagger} \left(h_n^+ \delta_{p,0} a_{np\sigma} + h_n^- \delta_{p,0} b_{np\sigma} \right) + \left(h_n^+ \delta_{p,0} a_{np\sigma}^{\dagger} + h_n^- \delta_{p,0} b_{np\sigma}^{\dagger} \right) d_{\sigma} \right\}. \end{aligned} \quad (3.36)$$

This substitution is not only permissible, but it is not even an approximation if we transfer all the ϵ dependence to $g(\epsilon)$ in the interval, such that Eq. (3.32) is met. Integrating (3.32) with respect to ϵ in the intervals x_n^{\pm} with the condition that $h(\epsilon)^{\pm}$, $\epsilon \in x_n^{\pm}$, be replaced by h_n^{\pm} , we obtain

$$\int_{x_n^{\pm}} d\epsilon \frac{d\omega}{d\epsilon(\omega)} \frac{\Gamma(\omega)}{\pi} = \int_{x_n^{\pm}} d\epsilon (h_n^{\pm})^2, \quad (3.37)$$

and therefore

$$(h_n^{\pm})^2 = \frac{1}{d_n} \int_{x_n^{\pm}} d\omega \frac{\Gamma(\omega)}{\pi}, \quad (3.38)$$

where we use the shorthand notation

$$\int_{x_n^{\pm}} d\omega := \int_{x_{n+1}^{\pm}}^{x_n^{\pm}} d\omega.$$

With this form of h_n^\pm and the definition $(\gamma_n^\pm)^2 = \pi d_n (h_n^\pm)^2$ we can finally write the hybridization term as

$$\begin{aligned} & \int_{-1}^1 d\epsilon h(\epsilon) (d_{\epsilon\sigma}^\dagger a_{\epsilon\sigma} + a_{\epsilon\sigma}^\dagger d_{\epsilon\sigma}) = \\ & \frac{1}{\sqrt{\pi}} \sum_n \left\{ d_{\epsilon\sigma}^\dagger (\gamma_n^+ a_{n0\sigma} + \gamma_n^- b_{n0\sigma}) + (\gamma_n^+ a_{n0\sigma}^\dagger + \gamma_n^- b_{n0\sigma}^\dagger) d_{\epsilon\sigma} \right\}. \end{aligned} \quad (3.39)$$

Next, we evaluate the term

$$\begin{aligned} & \int_{-1}^1 d\epsilon g(\epsilon) a_{\epsilon\sigma}^\dagger a_{\epsilon\sigma} \\ & = \int_{-1}^1 d\epsilon g(\epsilon) \left\{ \sum_{n,n'} \sum_{p,p'} [(\psi_{np}^+)^* a_{np\sigma}^\dagger + (\psi_{np}^-)^* b_{np\sigma}^\dagger] [\psi_{n'p'}^+ a_{n'p'\sigma} + \psi_{n'p'}^- b_{n'p'\sigma}] \right\} \\ & = \sum_n \sum_{p,p'} \int_{-1}^1 d\epsilon g(\epsilon) [(\psi_{np}^+)^* \psi_{np'}^+ a_{np\sigma}^\dagger a_{np'\sigma} + (\psi_{np}^-)^* \psi_{np'}^- b_{np\sigma}^\dagger b_{np'\sigma}]. \end{aligned} \quad (3.40)$$

The second sum can be split into two cases: $p = p'$ and $p \neq p'$. The former amounts to the quantity

$$\sum_{n,p} \left\{ a_{np\sigma}^\dagger a_{np\sigma} \left[\frac{1}{d_n} \int_{x_n^+} d\epsilon g(\epsilon) \right] + b_{np\sigma}^\dagger b_{np\sigma} \left[\frac{1}{d_n} \int_{x_n^-} d\epsilon g(\epsilon) \right] \right\}.$$

In order to evaluate this integral conforming to Eq. (3.32) we do the following change of variables:

$$\begin{aligned} \frac{\partial \epsilon(g)}{\partial g} &= \frac{1}{\pi h^2} \Gamma(g) \rightarrow \int_{x_n^\pm} dg g(\epsilon) \frac{\partial \epsilon(g)}{\partial g} = \frac{1}{\pi (h_n^\pm)^2} \int_{x_n^\pm} dg g \Gamma(g) \\ &= \int_{x_n^\pm} d\epsilon g(\epsilon) = \frac{1}{\pi (h_n^\pm)^2} \int_{x_n^\pm} dg g \Gamma(g), \end{aligned}$$

so that

$$\frac{1}{d_n} \int_{x_n^\pm} d\epsilon g(\epsilon) = \int_{x_n^\pm} d\epsilon \epsilon \Gamma(\epsilon) \Big/ \int_{x_n^\pm} d\epsilon \Gamma(\epsilon). \quad (3.41)$$

We define this quantity as ξ_n^\pm and the terms for $p = p'$ become

$$\int_{-1}^1 d\epsilon g(\epsilon) a_{\epsilon\sigma}^\dagger a_{\epsilon\sigma} = \sum_{n,p} \left\{ \xi_n^+ a_{np\sigma}^\dagger a_{np\sigma} + \xi_n^- b_{np\sigma}^\dagger b_{np\sigma} \right\}. \quad (3.42)$$

It will only be necessary to evaluate the terms with $p = 0$. From the structure of Eq. (3.40) we can see that the terms with $p \neq 0$ only couple to the impurity through the states

with $p = 0$. The couplings between these states can be considered small— of order $1 - \Lambda^{-1} \rightarrow 0$ as $\Lambda \rightarrow 1$ —and thus neglected. It should be mentioned that in practice the value of Λ is usually taken between 2 and 4, and one may argue whether the value of $1 - \Lambda^{-1}$ is negligible or not. It is important to keep in mind that Λ is simply a parameter of the method, and because of this one should expect that any physical quantities calculated with this method will not depend significantly upon its value: a requirement that can only be verified *a posteriori*. The fact is that this is a well-controlled approximation which produces exceptionally good results in practice. However, if the reader is dissatisfied with this argument, we direct them to Refs. [43] and [44] for more refined methods of discretization that do not rely on a specific value of the discretization parameter.

The discussion above can also be applied to the part with $p \neq p'$ calculated above, and so we are left with a Hamiltonian of the form

$$H = H_{imp} + \sum_n \left\{ \xi_n^+ a_{n0\sigma}^\dagger a_{n0\sigma} + \xi_n^- b_{n0\sigma}^\dagger b_{n0\sigma} \right\} + \frac{1}{\sqrt{\pi}} \sum_n \left\{ d_\sigma^\dagger (\gamma_n^+ a_{n0\sigma} + \gamma_n^- b_{n0\sigma}) + (\gamma_n^+ a_{n0\sigma}^\dagger + \gamma_n^- b_{n0\sigma}^\dagger) d_\sigma \right\}. \quad (3.43)$$

We will drop the subindex $p = 0$ in the future for the sake of convenience. The final step consists of re-writing Eq. (3.43) in the form

$$H = H_{imp} + \sqrt{\frac{\xi_0}{\pi}} \sum_\sigma \left\{ d_\sigma^\dagger c_{0\sigma} + c_{0\sigma}^\dagger d_\sigma \right\} + \sum_{\sigma, n=0}^{\infty} \left\{ \varepsilon_n c_{n\sigma}^\dagger c_{n\sigma} + t_n (c_{n\sigma}^\dagger c_{n+1\sigma} + c_{n+1\sigma}^\dagger c_{n\sigma}) \right\}, \quad (3.44)$$

with the index n corresponding to the number of the site in what will henceforth be called the *NRG chain*. The operators $c_{n\sigma}$ are related to $a_{m\sigma}$ and $b_{m\sigma}$ by a unitary transformation of the form

$$a_\sigma = U^T c_\sigma, \quad (3.45a)$$

$$b_\sigma = V^T c_\sigma, \quad (3.45b)$$

$$c_\sigma = U a_\sigma + V b_\sigma, \quad (3.45c)$$

with the notation

$$a_\sigma = \begin{pmatrix} a_{0\sigma} \\ a_{1\sigma} \\ \vdots \end{pmatrix}, \quad b_\sigma = \begin{pmatrix} b_{0\sigma} \\ b_{1\sigma} \\ \vdots \end{pmatrix}, \quad c_\sigma = \begin{pmatrix} c_{0\sigma} \\ c_{1\sigma} \\ \vdots \end{pmatrix}.$$

From Eq. (3.43) we can directly obtain the matrix elements $U_{0m} = \gamma_m^+ / \sqrt{\xi_0}$ and $V_{0m} = \gamma_m^- / \sqrt{\xi_0}$, and the parameter $t_0 = \sqrt{\xi_0/\pi}$. The remaining matrix elements and the parameters ε_n and t_n , however, have to be obtained by solving the system of equations (3.45a) through (3.45c). The solution to this problem is lengthy and does not provide any further insight into the physics of the problem, and so it will not be discussed here. The interested reader is encouraged to visit Refs. [40] and [45] for a detailed description of the method of solution. It is useful, however, to have the case of a constant hybridization function as a reference. In that case an analytical solution has been found[24] for the system, and it gives the NRG chain parameters

$$t_n = \frac{(1 + \Lambda^{-1})(1 - \Lambda^{-(n+1)})}{2\sqrt{1 - \Lambda^{-(2n+1)}}\sqrt{1 - \Lambda^{-(2n+3)}}}\Lambda^{-n/2}, \quad \varepsilon_n = 0. \quad (3.46)$$

The relevant feature of Eq. (3.46)— which is also valid for a generic density of states— is that the couplings t_n decrease exponentially with the iteration number n . An immediate consequence of this is that, once we diagonalize the Hamiltonian Eq. (3.44) including sites up to $n - 1$, adding the degrees of freedom of site n will only shift the energy levels by an energy approximately one power of Λ smaller than the current energy scale. An even more important feature is that the product $\Lambda^{n/2}t_n$ is of order one for all n , a necessary feature for the RG properties of the Hamiltonian Eq. (3.44), which we discuss below.

3.2.2 Iterative diagonalization and RG flow of the eigenvalues

Let us write the partial Hamiltonian containing the operators only up to the N th site of the NRG chain, as

$$H_N := \Lambda^{(N-1)/2} \left[H_{-1} + \sum_{\sigma, n=0}^N \varepsilon_n c_{n\sigma}^\dagger c_{n\sigma} + \sum_{\sigma, n=0}^{N-1} t_n \left(c_{n\sigma}^\dagger c_{n+1\sigma} + c_{n+1\sigma}^\dagger c_{n\sigma} \right) \right], \quad (3.47)$$

with the definitions

$$H_{-1} := H_{\text{imp}}. \quad (3.48)$$

The full Hamiltonian is recovered as

$$H = \lim_{N \rightarrow \infty} \Lambda^{-(N-1)/2} H_N. \quad (3.49)$$

There are two important reasons for this way of writing the Hamiltonian: first, the pre-factor $\Lambda^{(N-1)/2}$ in Eq. (3.47) serves, as mentioned in the previous section, to eliminate the N -dependence of the last coupling t_{N-1} . Through this rescaling of the energy we are able to directly compare the eigenvalues of a partial Hamiltonian, say H_m , to those of the next one, H_{m+1} . Second, this allows us to relate H_N to $H_N + 1$ as

$$H_{N+1} = \sqrt{\Lambda} H_N + \Lambda^{N/2} \sum_{\sigma} \varepsilon_{N+1} c_{N+1\sigma}^\dagger c_{N+1\sigma} + \Lambda^{N/2} \sum_{\sigma} t_N \left(c_{N\sigma}^\dagger c_{N+1\sigma} + c_{N+1\sigma}^\dagger c_{N\sigma} \right). \quad (3.50)$$

These two points allow us to define the *Renormalization Group transformation*

$$\mathfrak{R}\{H_N\} := H_{N+1} - E_{\text{gnd}}^{N+1}, \quad (3.51)$$

with E_{gnd}^{N+1} the ground state energy of H_{N+1} .

In this scheme, the RG flow is defined by the variation of the lowest eigenvalues of the subsequent Hamiltonians, as shown in Figure 3.4. Two important details can be observed in the figure: first, there are some stages of the flow where the eigenvalues remain constant, connected by other short ones that mark transitions. The former constitute fixed points, as discussed in Section 3.1.3. The second detail is that there is an

energy flow corresponding to odd-numbered iterations, and another, slightly different one, corresponding to even-numbered iterations. The explanation for this comes from the Hamiltonian form $H_N - H_{-1}$, that is, the Hamiltonian of the NRG chain alone. The reason for this is that at any iteration N the Hamiltonian Eq. (3.47) involves $2(N + 1)$ operators $(d_\uparrow, d_\downarrow, \dots, c_{N\uparrow}, c_{N\downarrow})$, which due to spin symmetry within the band result in $N + 1$ distinct energy levels; a number that changes from even to odd every iteration. Then, as a consequence of particle-hole symmetry within the band, we can establish that for every level of positive energy η there must be a corresponding level of energy $-\eta$. In the case of $N + 1$ odd, one of these levels must be $\eta = 0$, whereas for $N + 1$ even there is no such level. Due to this fundamental difference between even and odd iterations, the actual RG transformation—the one that produces a RG flow—is in fact \mathfrak{R}^2 .

The NRG energy flow of the Hamiltonian is obtained by a process of iterative diagonalization. The first two iterations are shown in Fig. 3.5: we begin by diagonalizing the impurity Hamiltonian H_{-1} , and obtaining the sets of eigenvalues and eigenvectors $\{E_i^{(-1)} - E_{\text{gnd}}^{(-1)}\}$ and $\{|i\rangle_{-1}\}$. We also obtain the matrix elements ${}_{-1}\langle i|d_\sigma|i'\rangle_{-1}$ and ${}_{-1}\langle i|d_\sigma^\dagger|i'\rangle_{-1}$, which will be needed for the construction of the next iteration Hamiltonian.

The next step is to build the basis for iteration 0. It is at this stage of the procedure that the symmetries of the Hamiltonian must be taken into consideration to minimize the numerical load in the diagonalization procedure. The system preserves the total charge Q , and in the absence of a magnetic field many choices of H_{-1} are also spherically symmetric, and thus preserve total momentum \vec{S} and the spin projection S_z . For simplicity, however, we use only the preserved quantum numbers Q_N and S_N^z at iteration N , defined as

$$Q_N = \sum_{\sigma} (d_{\sigma}^\dagger d_{\sigma} - 1) + \sum_{\sigma, n=1}^N (c_{n\sigma}^\dagger c_{n\sigma} - 1), \quad (3.52a)$$

$$S_N^z = \frac{1}{2} (d_{\uparrow}^\dagger d_{\uparrow} - d_{\downarrow}^\dagger d_{\downarrow}) + \frac{1}{2} \sum_{n=0}^N (c_{n\uparrow}^\dagger c_{n\uparrow} - c_{n\downarrow}^\dagger c_{n\downarrow}). \quad (3.52b)$$

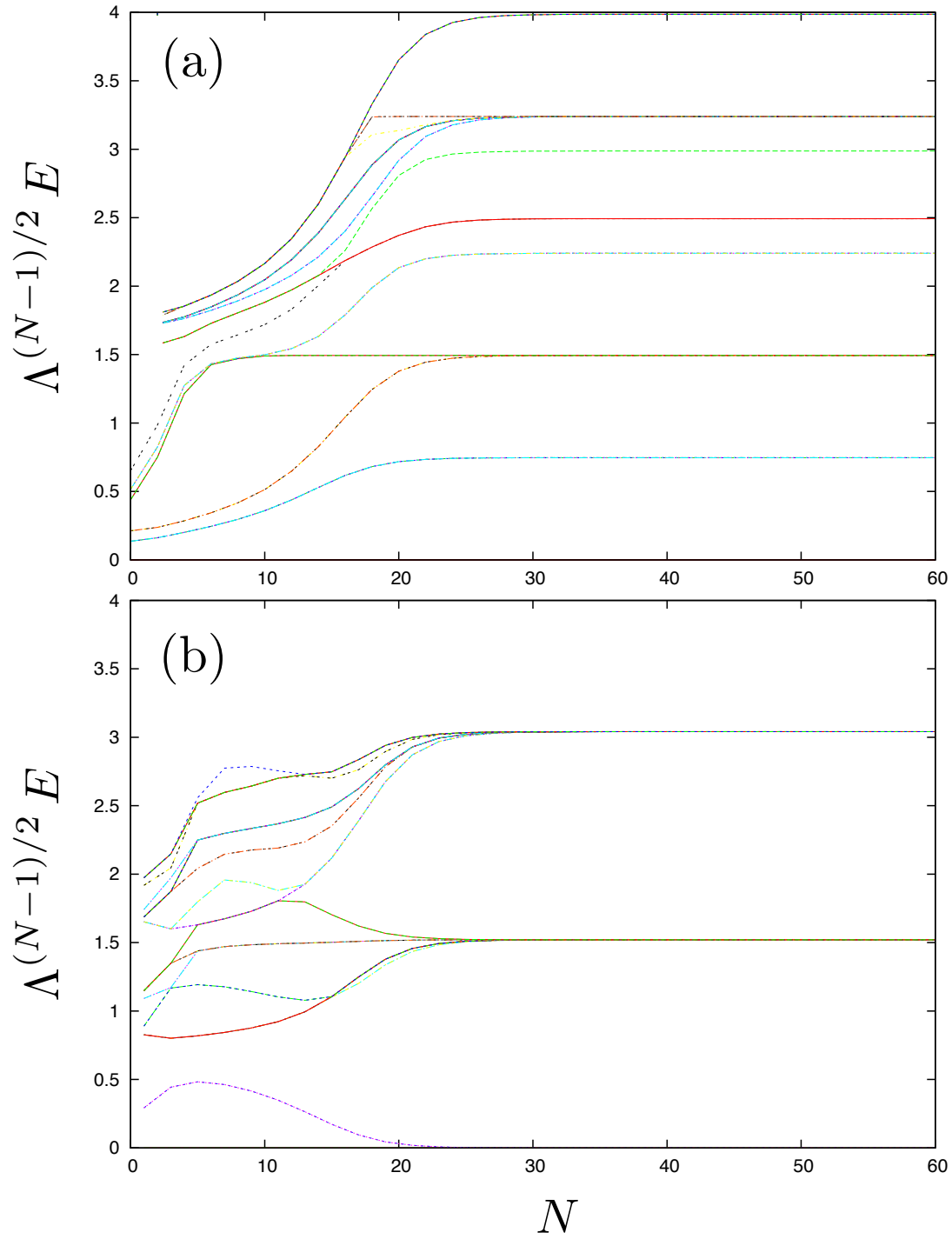


Figure 3.4: Renormalization group flow of the lowest-lying energy levels of the single-impurity Anderson Hamiltonian (see below). (a) Energy levels at iteration N for N even. (b) Energy levels at iteration N for N odd.

The Hamiltonian will be cast in block–diagonal form, each block with a fixed value of charge and spin projection. With this in mind, we change the notation for the eigenstates of the impurity to block form as

$$\{|i\rangle_{-1}\} \longrightarrow \{|Q, S_z; n\rangle_{-1}\},$$

where the index n numbers the states within the block. The basis for the blocks of iteration 0 takes the form

$$\{|b, i\rangle_0\} = \{|\mu\rangle_0 \otimes |Q, S_z; n\rangle_{-1}\}, \text{ with } Q + Q(\mu) = Q(b) \text{ and } S_z + S_z(\mu) = S_z(b). \quad (3.53)$$

The attached site state is given by $|\mu\rangle_0 = |0\rangle_0, |\uparrow\rangle_0, |\downarrow\rangle_0, |\uparrow\downarrow\rangle_0$. The NRG transformation is applied to produce the iteration–0 Hamiltonian in terms of these basis states, which we diagonalize to obtain the new energy spectrum, and the cycle is repeated.

Repeating the procedure will produce an exponentially increasing number of states, which will eventually become unmanageable for any computer for a number of reasons: first, the amount of memory required for keeping the information about the energy states and the necessary matrices increases exponentially with the iteration, N (8×4^N and 8×4^{2N} bytes, respectively, when using double–precision floating point variables). Second, with the exponential growth of the size of the Hamiltonian matrices, the amount of floating–point operations required for their diagonalization also increases, and the same is true for the evaluation of the matrices ${}_N \langle Q_1, S_{z1}; m | c_{N\sigma} | Q_2, S_{z2}; n \rangle_N$. To avoid this problem we truncate the number of states kept from one iteration to the next to maintain a manageable number of states throughout the calculation.

Although the truncation scheme might seem unjustified, the RG transformation maps the Hamiltonian onto an effective free energy valid within a certain energy window, as explained in Section 3.1.3. In this case, the energy scale of validity at iteration N is given by [38] $T_N \sim (1/2)(1 + \Lambda^{-1})\Lambda^{-(N-1)/2}D$. In other words, any expectation values calculated

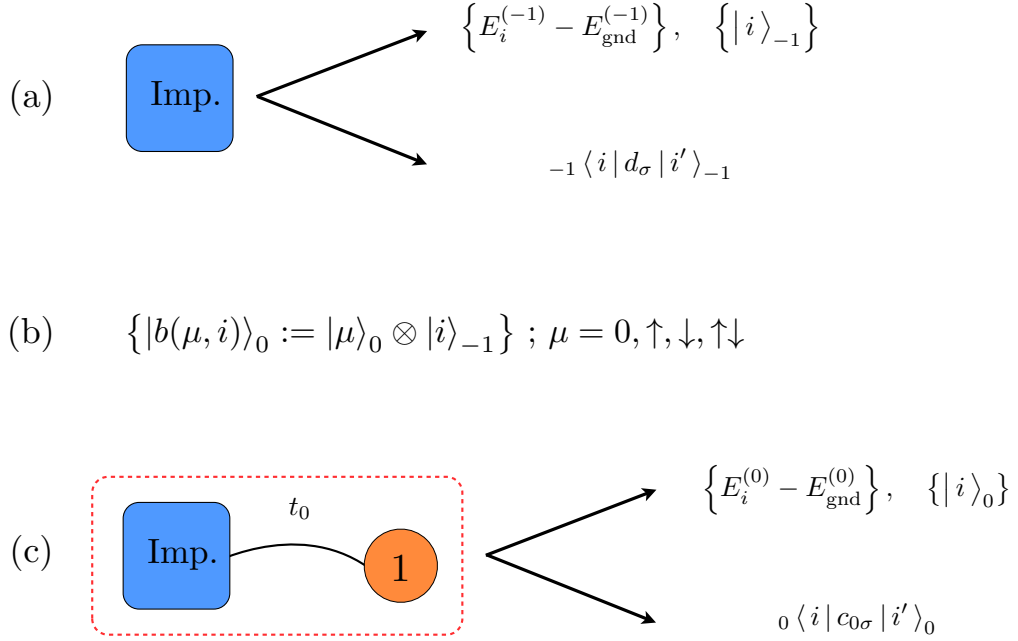


Figure 3.5: First two stages of the iterative diagonalization procedure. (a) The impurity Hamiltonian is diagonalized and the matrix elements of the impurity operators d_σ in the diagonal basis are evaluated. (b) The basis for the next iteration, which includes the impurity states and the first site of the NRG chain, is constructed as direct product states. (c) With this information, the matrix elements of the new iteration Hamiltonian are evaluated, and the process starts over.

over the energy spectrum of iteration N correspond to the behavior of the system at temperature T_N . This allows us to map the iteration N onto a temperature axis, and evaluate the temperature dependence of thermodynamic quantities of the Hamiltonian.

3.3 The Kondo effect revisited

Figure 3.6 presents an example of two thermodynamic quantities calculated with NRG utilizing the notion of temperature discussed above, for the single-impurity Anderson model, where $H_{-1} = \sum_\sigma \varepsilon_d n_{d\sigma} + U n_{d\uparrow} n_{d\downarrow}$, and a flat density of states. The entropy $S(T) = \log Z(T) + \langle H \rangle / T$ in Fig. 3.6(a) clearly depicts the three fixed points of the model: at high temperatures ($T/D \sim 1$), the influence of the band on the impurity is

negligible and the model has only four effective states ($|0\rangle, |\uparrow\rangle, |\downarrow\rangle, |\uparrow\downarrow\rangle$). This is called the *free orbital fixed point* (FOFP), and its signature is an entropy of $S = \log 4$, as shown in Fig. 3.6(a) with a red line intersecting the curve at $T/D \sim |\varepsilon_d|$. The *FOFP* is unstable, and for these parameters the system flows away from it immediately as temperature goes down.

As temperature decreases below the energy scale of U , charge fluctuations are frozen out and the ground state consists of only the two degenerate states $|\uparrow\rangle$ and $|\downarrow\rangle$, producing the plateau at $S = \log 2$ in Fig. 3.6. Because in this limit the system behaves as a spin-1/2 object, this is called the *local moment fixed point* (LMFP). Finally, at lower temperatures the physics of the system is dominated by spin fluctuations. Spin flips of the impurity through electrons hopping between the band and impurity produce a many-body ground state with a spin-singlet structure between the impurity and the band—the Kondo ground state—which dominates below a certain transition energy scale: the Kondo temperature T_K . This is called the *strong coupling fixed point* (SCFP), and its signaled by a vanishing entropy ($S = \log 1$) as $T \rightarrow 0$. The increased resistivity typical of the Kondo effect in bulk systems is a direct consequence of the nature of the system's ground state near or within the strong-coupling regime: while ballistic transport in a bulk system requires electronic traveling states, the singlet nature of the Kondo ground state forces incoming electrons to participate in the virtual spin-flip processes near the impurity, “slowing them down” and forming a virtual bound state.

Figure 3.6(b) shows the vanishing of the effective magnetic moment as the system transitions from a local moment (LMFP) to a spin singlet (SCFP), as the temperature is lowered below T_K . Historically[24], T_K is defined as the temperature at which $\mu^2 = 0.0707(g\mu_B)^2$. The figure shows that, for the present case, $T_K \approx 1.2 \times 10^{-7}D$.

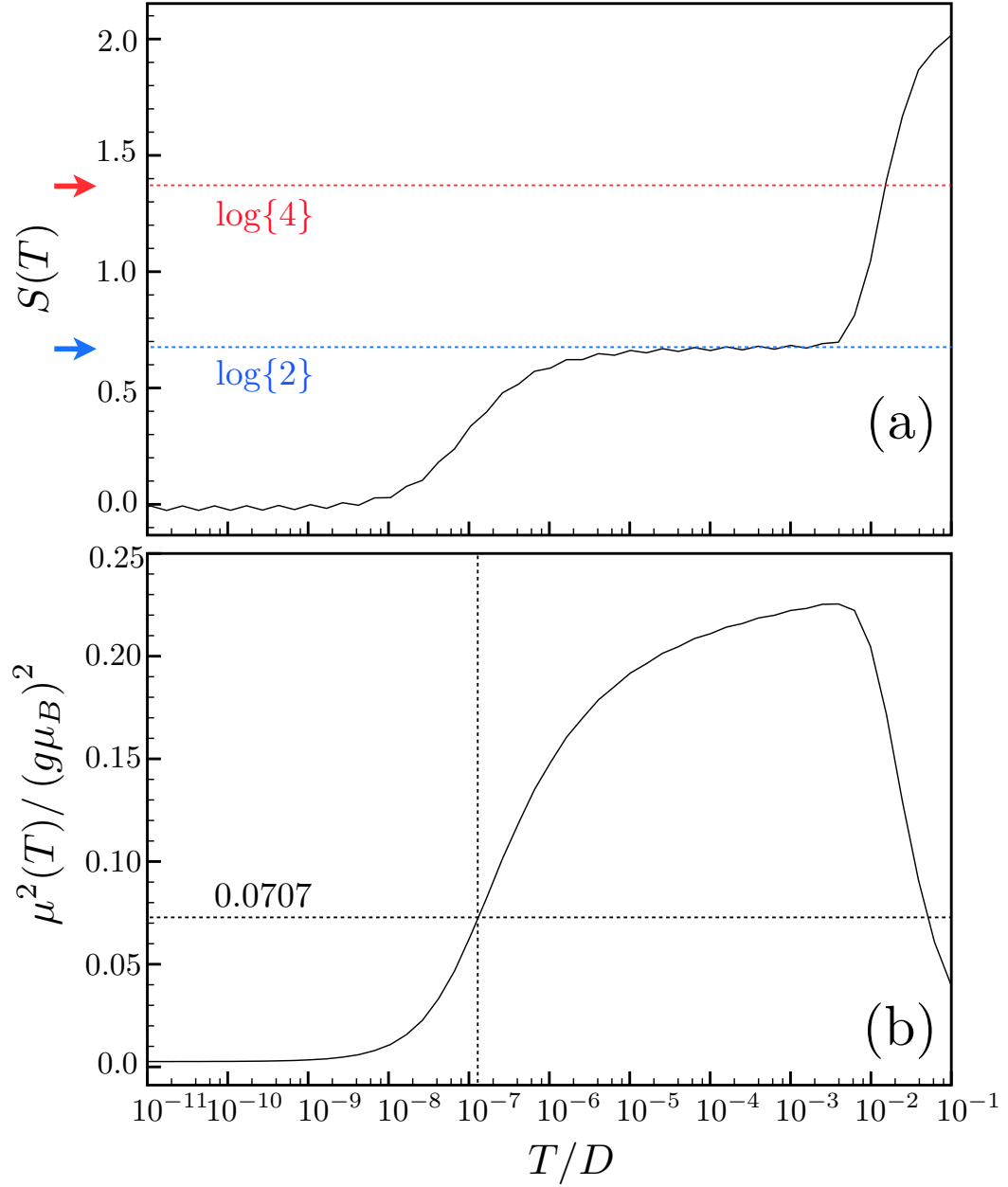


Figure 3.6: (a) Entropy and (b) magnetic-moment-squared of the symmetric, single-impurity Anderson model, as functions of temperature. Calculated with the NRG ($\Lambda = 2.5$) for parameters $\varepsilon_d = -U/2 = -0.025D$ and $\Gamma = 0.002D$. The reference lines in (a) mark the values of the entropy in the FOFP (red) and the LMFP (blue). Notice that, due to parameters, the flow toward the local-moment regime is so fast that the plateau of the free-orbital regime does not form.

In nanoscopic systems in the Kondo regime, electronic transport through the impurity depends entirely on the low-energy, single-particle excitations of the Kondo ground state. The dynamic quantity associated to these excitations is known as the local spectral density $\rho_d(\omega)$, defined by

$$G_d^\pm(\varepsilon) = \int d\omega \frac{\rho_d(\omega)}{\omega - \varepsilon \pm i\delta}, \quad (3.54)$$

where $\delta \rightarrow 0$ is positive, and $G_d^\pm(\varepsilon)$ are the advanced and retarded Green's functions at the impurity for superscript + and -, respectively.[46]. The spectral density in a many-body system is an analogue to the density of states in the single-particle case, and in our system it can be directly related to the conductance through the impurity (see below). We can obtain the spectral density from the NRG calculation using the energy spectra evaluated at every iteration, and the matrix elements of the impurity operator $\langle \psi(B, i) | d_\sigma | \psi(B', i') \rangle$, by writing $\rho_d(\omega)$ in the Lehmann representation:

$$\begin{aligned} \rho_d(\omega) = \sum_{\sigma} \sum_{B, i; B', i'} |\langle \psi(B, i) | d_\sigma | \psi(B', i') \rangle|^2 \\ \times \frac{(e^{-E(B, i)/T} + e^{-E(B', i')/T})}{Z(T)} \delta(\omega - [E(B, i) - E(B', i')]). \end{aligned} \quad (3.55)$$

Here, $|\psi(B, i)\rangle$ and $E(B, i)$ represent the i th eigenstate of block B , and its corresponding energy⁵. Many methods have been proposed to make use of the N th iteration eigenstates in the formula Eq. (3.55); we use the method presented in Ref. [41]. Figure 3.7 shows the spectral density for the single-impurity Anderson model for the same parameters of Fig. 3.6. The model parameters present themselves in the curve as indicated by the dashed lines: the peaks at $\omega \sim \pm U/2$ are called the Hubbard peaks, and they correspond to the charge excitations from half-filling of the impurity to empty and full. The peak in the middle is the Kondo peak, and its width is approximately given by the Kondo temperature T_K , as shown in the inset.

⁵ The temperature is introduced by interpreting Eq. (3.54) as a finite-temperature Green's function. See Ref. [47], Chapter 3.

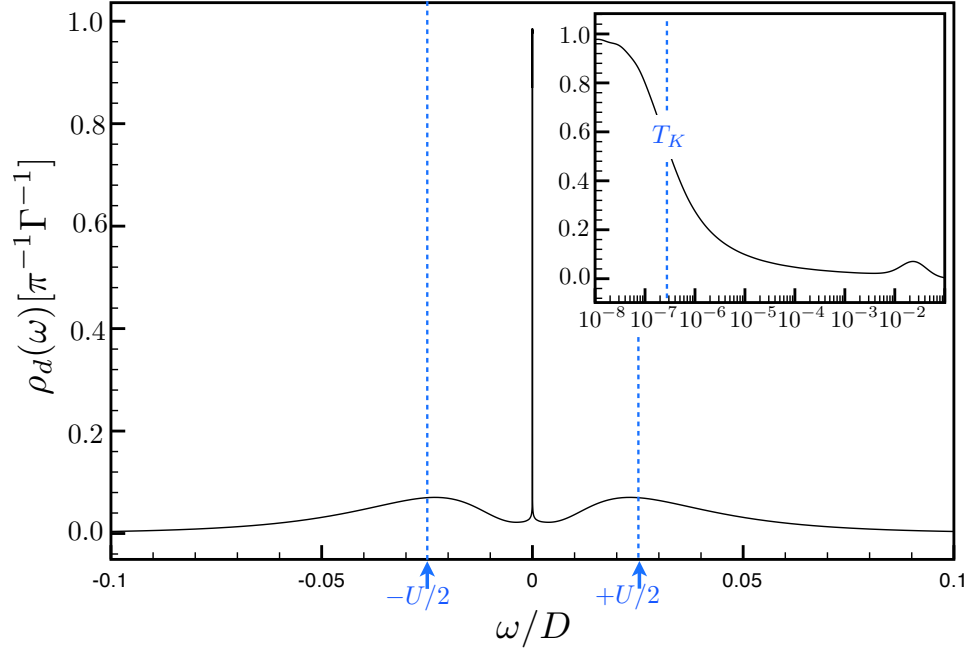


Figure 3.7: NRG results ($\Lambda = 2.5$) for the local spectral density at the impurity site for the single-impurity Anderson model, with parameters $\varepsilon_d = -U/2 = -0.025D$ and $\Gamma = 0.002D$. The inset is the same curve, with the abscissa in a logarithmic scale. We remind the reader of the convention that places the Fermi level as the zero of energy: $\varepsilon_F = 0$.

Finally, the Kondo peak has an amplitude $(\pi\Gamma)^{-1}$, as expected from the Friedel sum rule[48]. At zero temperature, the conductance is given in units of the conductance quantum (G_0) by the amplitude of the spectral density at the Fermi level, in units of $(\pi\Gamma)^{-1}$. The Kondo peak is thus directly responsible for the enhanced conductance typical of nanscopic system in the Kondo regime, as it opens a conduction channel through the impurity which would otherwise be in a Coulomb blockade regime.

This concludes our review of the Kondo effect, studied by the NRG technique. The physical quantities introduced above will be thoroughly discussed in Sections 4.3 and 4.4, in the context of our original work.

4 DYNAMICAL MAGNETIC ANISOTROPY IN A SPIN-1 MOLECULAR JUNCTION

As we discussed in Sec. 2, the Kondo effect appears when an anti-ferromagnetic interaction arises between the impurity's magnetic moment and the spins of the electrons in the metallic band. When this happens s -band electrons, for example, will screen at most a total spin of $\hbar/2$ out of the total impurity spin[48], S_d . If $S_d > \hbar/2$, there will be a net unscreened magnetic moment of $S_d - 1/2$, and the system will have very specific thermodynamic and transport signatures, dependent on the value of S_d [49]. Examples of this situation have been observed in molecular systems[7, 8] and heavy fermion systems[48].

The Kondo effect in molecular junctions has the potential to be very rich in phenomenology, due to the many available molecular geometries. The electronic structure of the molecule is strongly related to the symmetries of the ligand field, the distribution of atomic orbitals, spin-orbit effects, etc., all of which should be incorporated in a realistic model of the molecular system. In this chapter, we present our study of a remarkable experiment by Parks *et al.*, of the spin-1 molecule $\text{Co}(\text{tpy-SH})_2$ (4'-mercapto-2, 2':6', 2''-terpyridine) in a break junction setup, which can be stretched by mechanical means. The experimental setup is depicted in Fig. 4.1a, where the molecule is deposited between two metallic leads, on top of a substrate that can be bent by pushing a screw against it from below, causing the junction to open, thus stretching the molecule in the middle.

The overall symmetry of the molecular field produces a spin-1 triplet ground state[8] formed out of two degenerate d -orbitals of the cobalt atom at the center of the molecule. Because of the octahedral symmetry, all three directions “seem” equivalent to the molecular spin vector, but this is not the case when the molecule is deformed. A

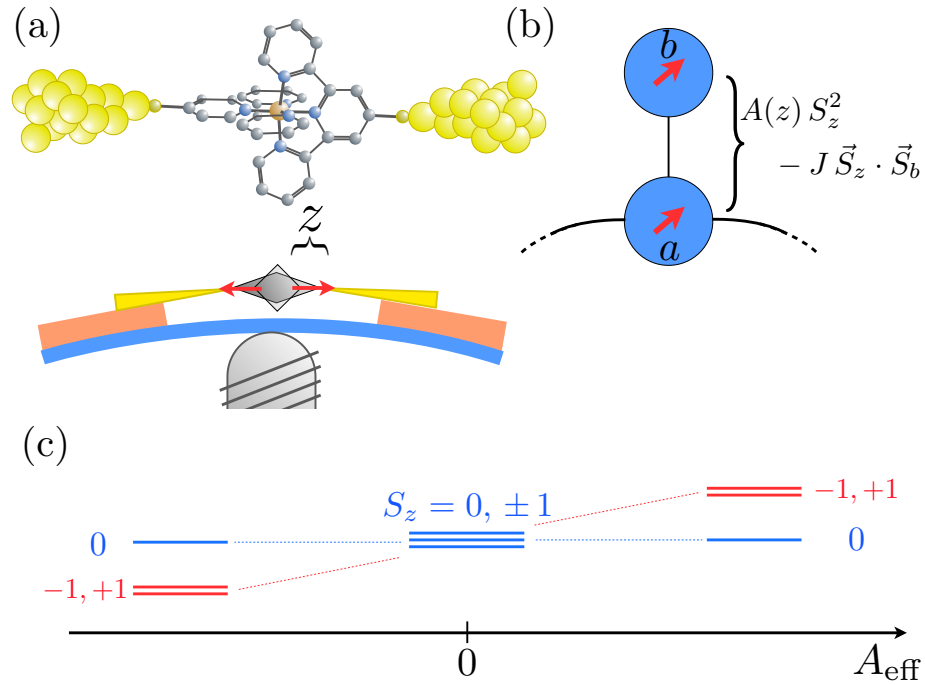


Figure 4.1: (a) The molecule Co(tpy-SH) between metallic leads. (b) The cobalt atom at the center of the molecule has a spin-1 ground state due to Hund's rule, which in our model is enforced by a ferromagnetic interaction between two atomic d -levels. (c) Stretching and compression of the molecule result in an effective magnetic anisotropy, which splits the triplet ground state, raising or lowering the states with $S_z \neq 0$ with respect to the state of $S_z = 0$. (Extracted from Ref. [12])

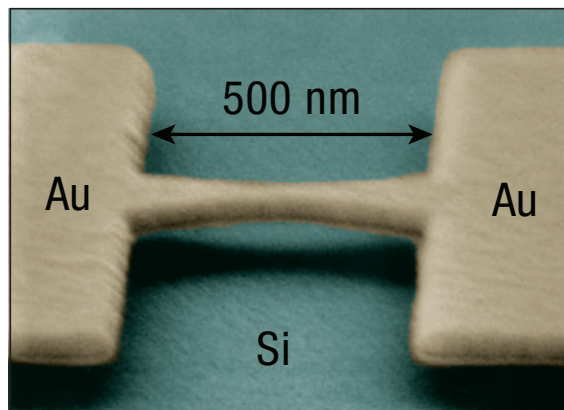


Figure 4.2: SEM image of the break junction setup (extracted from Ref. [8], with permission of the American Association for the Advancement of Science).

symmetry breaking of this kind for a generic molecule is known to introduce spin–orbit effects[50, 51], and to split or even sometimes produce orbital degeneracies[52–54]; a general model for the molecular junction must include all of these effects. For this specific setup, the z -axis can be singled out by stretching or compressing the molecule along that direction (Fig. 4.1a), and the distorted ligand field lifts the degeneracy of the spin–1 triplet through spin–orbit effects[55], that is, the energy of the system is different when the spin is pointing along the z -axis than when it points along some direction on the transverse plane. Stretching, however, does not distinguish between the positive and negative directions of the z -axis, so this effect can be modeled by introducing an energy term of the form

$$A_0 S_z^2, \quad (4.1)$$

into the Hamiltonian of the system. Here, S_z is the molecular spin’s z -projection⁶ and the factor A_0 depends on the stretching. This term will split the former triply–degenerate ground state into two: a state with $S_z = 0$, and the doublet $S_z = \pm 1$ (Fig. 4.1c). When $A_0 > 0$, the ground state will be the $S_z = 0$ state, while for $A_0 < 0$ the ground state will be the doublet. Trifold degeneracy is recovered when $A_0 = 0$.

When placed in the center of a break junction (Figure 4.2), these different ground states will yield distinct electronic transport signatures (see Fig. 1 in Ref. [55]). This case is discussed by Cornaglia *et al.*, in Ref. [55], where they predict that the break junction system displays a Kondo ground state at zero stretching— in which case $A_0 = 0$ —, as indicated by the enhanced zero–bias conductance through the molecule⁷. This is in fact a spin–1 Kondo state with associated Kondo temperature T_K^0 , which means that the magnetic moment of the molecule is only partially screened.

⁶ In our notation, $S_z = \sigma_z/\hbar$, with σ_z the traditional Pauli operator: $\sigma_z |\uparrow\rangle = \hbar/2 |\uparrow\rangle$, and $\sigma_z |\downarrow\rangle = -\hbar/2 |\downarrow\rangle$. In this convention, A_0 has units of energy.

⁷ In Section 2.2 it was mentioned that the onset of Kondo correlations is strongly dependent on the degeneracy of the spin–up and spin–down states of the spin–1/2 impurity. In this case, the degeneracy is between the three states of the spin–1 triplet. These two cases correspond to distinct universality classes[56], hence the distinction between spin–1/2 and spin–1 Kondo effects.

The anisotropy is then tuned by stretching the molecule. As determined by Cornaglia *et al.*, and verified experimentally by Parks *et al.*, stretching introduces a positive anisotropy ($A_0 > 0$), putting the system in what is called a hard-axis regime, due to the fact that it costs more energy to have the spin vector point along the transport axis. In this situation the doublet is lifted away from the ground state of $S_z = 0$. This prevents spin-flip scattering from taking place, due to the energy cost of reaching either of the $|S_z| = 1$ states, and the Kondo effect is destroyed. When the splitting is much smaller than T_K^0 , however, a new screening channel opens by effect of the anisotropy coupling

$$A_0 S_z^2 = \frac{3}{4} A_0 + A_0 (S_z^a S_z^b - S_x^a S_x^b - S_y^a S_y^b) \iff S_d = 1. \quad (4.2)$$

Eq. (4.2) describes an anisotropic form of the s - d model that, according to the interpretation given in Ref. [55], will couple the remaining unscreened magnetic moment to the Fermi liquid of the original spin-1 Kondo ground state[48] and achieve full screening with a second-stage Kondo temperature $T_K^{0*} < T_K^0$, given by

$$T_K^* = c_1 T_K^0 e^{-2c_2 \sqrt{\frac{T_K^0}{A_{\text{Net}}}}}, \quad (4.3)$$

with A_{Net} the net anisotropy of the system, and $c_1, c_2 \sim 1$ fitting constants that depend on the system parameters.

These regimes can be identified also through the zero-bias conductance of the system, $G(T)$, in terms of the spectral density of the molecular level (see Eq. (3.54)). While the hard-axis regime puts the system in a Coulomb blockade (see discussion in Section 4.3) and hopping of electrons into the molecular level can only occur by thermal excitation, the two Kondo phases open an electronic state at the Fermi level allowing for unitary transport at zero temperature (see Section 2). These results were first presented in Fig. 1 of Ref. [55], where conductance is calculated as a function of temperature: For large anisotropy ($A_0 \gg T_K^0$), conductance dies out as $T \rightarrow 0$, whereas the curves for small anisotropy ($A_0 \lesssim T_K^0$) go to $G_0 = 2e^2/h$.

4.1 Molecular vibrations and dynamic anisotropy

To this point, only the Kondo regimes and the hard-axis regime have been discussed. An easy-axis regime of $A_0 < 0$ is expected when the molecule is compressed. In the present experimental setup, compression of the molecule can only occur at deposition, when the break junction is open and the molecule gets trapped in between the leads. By subsequently closing the junction, the molecule can be compressed, putting the system in an easy-axis regime before deliberately stretching the molecule. However, no signatures of this situation are observed in the results of Ref. [8].

Our contribution to the study of this molecular system consisted in the analysis of an extension to the molecular model, which incidentally presents another way in which the easy-axis regime could be produced. The large size of the molecule as compared to atomic scales, and the many degrees of freedom of its structure make it a flexible, dynamic object, posing the possibility of electro-mechanical effects, other than the static anisotropy discussed above. We proposed that molecular vibrations play an important role in its electronic properties, and introduced a model that incorporates them into the Hamiltonian in the form of an effective dynamical anisotropy term of the form of Eq. (4.1). In fact, as will be discussed below, one of the achievements of our study is the ability to incorporate the effect of this spin-vibron interaction as a correction to the static anisotropy.

Our model is shown in Fig. 4.1b. We represent the cobalt's d -orbitals as two, identical levels of energy $\varepsilon < 0$, only one of which hybridizes with the metallic leads. Let us call the hybridizing level “ a ”, and the hanging level “ b ”. We choose this configuration over other possibilities, e.g., both levels hybridizing with the leads, because they are equivalent in the sense that they are single-channel models that can be related by means of a level rotation of the Hamiltonian[55]. As a convention, we set the Fermi level as the zero of energy ($\varepsilon_F = 0$) and assume the metallic band from the leads to have a half-bandwidth D . That is, the band contains electronic states of energies ranging from $-D$ to D .

Our model for vibrations consists of a single vibrational (phonon) mode of frequency ω_0 along the transport axis. As will become obvious later, several phonon modes and even a phonon dispersion will lead to the same qualitative results.

The Hamiltonian for this system contains several terms. For clarity, we show them separately. First, the molecule's Hamiltonian is given by

$$H_M = H_0 + \left(A_0 + A_1 \left[a + a^\dagger \right] \right) S_z^2 + \omega_0 a^\dagger a, \quad (4.4)$$

where a and a^\dagger are phonon annihilation and creation operators, ω_0 is the phonon energy, and A_1 is the spin–vibron coupling. The term H_0 is given by

$$H_0 = \sum_{i=a,b} (\varepsilon n_i + U n_{i\uparrow} n_{i\downarrow}) - J \vec{S}_a \cdot \vec{S}_b, \quad (4.5)$$

where $n_i = n_{i\uparrow} + n_{i\downarrow}$, is the total number operator of level $i (= a, b)$, and \vec{S}_i is its spin operator. This term models the molecular levels, enforcing single occupation by means of the large Coulomb interaction U , where $D \gg U \gg |\varepsilon|$. The Hund's rule of strength $J > 0$ that fixes the required spin–1 ground state is modeled as a ferromagnetic term. Because the Kondo effect results from many–body spin fluctuations, we set $J < U$ so that spin excitations occur at lower temperatures than charge excitations. This is not a stringent requirement, however, because the spin–1 configuration can only arise at half filling—that is, for a fixed charge of one electron per impurity—and thus the large J itself enforces the desired charge configuration as the ground state (this was also verified through the NRG calculations).

The low–lying eigenstates of H_0 are the triplet

$$|T, +1\rangle := |\uparrow_a \uparrow_b\rangle, \quad |T, -1\rangle := |\downarrow_a \downarrow_b\rangle, \quad |T, 0\rangle := \frac{1}{\sqrt{2}} (|\uparrow_a \downarrow_b\rangle + |\downarrow_a \uparrow_b\rangle), \quad (4.6)$$

with corresponding energies

$$E^0(T, \pm 1) = E^0(T, 0) = 2\varepsilon - \frac{J}{4}. \quad (4.7)$$

These are the most important at low temperature, but for completeness we show the higher-energy states as well: the other state at single electron occupancy in each level (half-filling) is the singlet state

$$|S, 0\rangle := \frac{1}{\sqrt{2}}(|\uparrow_a \downarrow_b\rangle - |\downarrow_a \uparrow_b\rangle) \quad ; \quad E(S, 0) = 2\varepsilon + \frac{3J}{4}. \quad (4.8)$$

Higher- and lower-occupation states have higher energies, and they are shown in Table 4.1.

State	Energy
$ 0_a, 0_b\rangle$	$E(0_a, 0_b) = 0$
$ \sigma_a, 0_b\rangle$	$E(\sigma_a, 0_b) = \varepsilon$
$ 0_a, \sigma_b\rangle$	$E(0_a, \sigma_b) = \varepsilon$
$ \uparrow\downarrow_a, 0_b\rangle$	$E(\uparrow\downarrow_a, 0_b) = 2\varepsilon + U$
$ 0_a, \uparrow\downarrow_b\rangle$	$E(0_a, \uparrow\downarrow_b) = 2\varepsilon + U$
$ \uparrow\downarrow_a, \sigma_a\rangle$	$E(\uparrow\downarrow_a, \sigma_a) = 3\varepsilon + U$
$ \sigma_a, \uparrow\downarrow_b\rangle$	$E(\sigma_a, \uparrow\downarrow_b) = 3\varepsilon + U$
$ \uparrow\downarrow_a, \uparrow\downarrow_b\rangle$	$E(\uparrow\downarrow_a, \uparrow\downarrow_b) = 4\varepsilon + 2U$

Table 4.1: Higher energy states of the Hamiltonian H_0 , given by Eq. (4.5).

To understand the phonon terms in Eq. (4.4), consider a generic, elongation-dependent anisotropy $A(z)$. Provided the elongation is small, this function can be expanded in a Taylor series up to first order in z as

$$A(z) \approx A_0 + C z, \quad (4.9)$$

The dimensions of the coefficient C being energy, divided by length. The stretching z can be put in terms of the phonon operators as

$$z = \sqrt{\frac{\hbar^2}{2m_e\omega_0}} (a + a^\dagger), \quad (4.10)$$

with m_e the electronic mass, and defining $A_1 := \sqrt{\hbar^2/(2m_e\omega_0)} C$, Eq. (4.4) follows.

The leads have not been consider yet, but it is instructive to begin by solving the molecular Hamiltonian exactly. In fact, everything in H_M is already diagonal, save for the term $A_1 (a + a^\dagger) S_z^2$, which couples the fermionic and bosonic degrees of freedom of the problem. The difficulty that this term poses is that the bosonic sector of the Hilbert space of this Hamiltonian is infinite-dimensional, and so the matrix that represents this term is of infinite size, preventing us from diagonalizing it directly. In order to circumvent this difficulty, we resort to a unitary transformation.

The reader can immediately verify that the unitary operator

$$\mathcal{U} := \exp \left\{ -\frac{A_1}{\omega_0} S_z^2 (a - a^\dagger) \right\}, \quad (4.11)$$

diagonalizes the problem as

$$\tilde{H}_M := \mathcal{U} H_M \mathcal{U}^\dagger = H_0 + \tilde{A} S_z^2 + \omega_0 b^\dagger b, \quad (4.12)$$

with the renormalized anisotropy

$$\tilde{A} := A_0 - \frac{A_1^2}{\omega_0}, \quad (4.13)$$

and the displaced phonon operator $b = a + (A_1/\omega_0) S_z^2$. It is clear from Eq. (4.13) that the effective anisotropy is negative in the absence of stretching ($A_0 = 0$), putting the molecule in the easy-axis regime. This dynamic correction to the anisotropy is larger for smaller values of ω_0 ; as a reference, reported values for longitudinal modes of a free terpyridine molecule like the one studied here are within the range of 3 to 6 meV[57].

The low-energy eigenstates of the molecular Hamiltonian are

$$|T, \pm 1; \tilde{n}\rangle = |T, \pm 1\rangle |\tilde{n}\rangle, \quad |T, 0; n\rangle = |T, 0\rangle |n\rangle, \quad (4.14)$$

with corresponding energies

$$E(T, \pm 1; \tilde{n}) = 2\varepsilon - \frac{J}{4} + \tilde{A} + n\omega_0, \quad E(T, 0; n) = 2\varepsilon - \frac{J}{4} + n\omega_0. \quad (4.15)$$

The rounded ket $|m\rangle$ is the phonon state of occupation m , and we define

$$|\tilde{n}\rangle := e^{\frac{A_1}{\omega_0}(a-a^\dagger)} |n\rangle. \quad (4.16)$$

Again, for completeness, we list the rest of the states in Table 4.2.

State	Energy
$ 0_a, 0_b; n\rangle$	$E(0_a, 0_b; n) = n\omega_0$
$ \sigma_a, 0_b\rangle e^{\frac{A_1}{4\omega_0}(a-a^\dagger)} n\rangle$	$E(\sigma_a, 0_b; n) = \varepsilon + \frac{\sigma_a}{4}\tilde{A} + n\omega_0$
$ 0_a, \sigma_b\rangle e^{\frac{A_1}{4\omega_0}(a-a^\dagger)} n\rangle$	$E(0_a, \sigma_b) = \varepsilon + \frac{\sigma_b}{4}\tilde{A} + n\omega_0$
$ \uparrow\downarrow_a, 0_b; n\rangle$	$E(\uparrow\downarrow_a, 0_b; n) = 2\varepsilon + U + n\omega_0$
$ 0_a, \uparrow\downarrow_b; n\rangle$	$E(0_a, \uparrow\downarrow_b; n) = 2\varepsilon + U + n\omega_0$
$ \uparrow\downarrow_a, \sigma_b\rangle e^{\frac{A_1}{4\omega_0}(a-a^\dagger)} n\rangle$	$E(\uparrow\downarrow_a, \sigma_b; n) = 3\varepsilon + U + \frac{\sigma_a}{4}\tilde{A} + n\omega_0$
$ \sigma_a, \uparrow\downarrow_b\rangle e^{\frac{A_1}{4\omega_0}(a-a^\dagger)} n\rangle$	$E(\sigma_a, \uparrow\downarrow_b; n) = 3\varepsilon + U + \frac{\sigma_b}{4}\tilde{A} + n\omega_0$
$ \uparrow\downarrow_a, \uparrow\downarrow_b; n\rangle$	$E(\uparrow\downarrow_a, \uparrow\downarrow_b; n) = 4\varepsilon + 2U + n\omega_0$

Table 4.2: Higher energy states of the Hamiltonian H_M , given by Eq. (4.12). In our notation, the symbol σ represents \uparrow and \downarrow when it represent spin projection, and $+1$ and -1 in formulas, respectively.

The transformation Eq. (4.11) has a physical interpretation. In order to get to it, we write the momentum operator from our phonon operators as

$$p = -i \sqrt{\frac{m\omega_0}{2}} (a - a^\dagger). \quad (4.17)$$

The argument of the exponential function in Eq. (4.11) can be written as

$$-i \frac{A_1}{\omega_0} S_z^2 \cdot \sqrt{\frac{2}{m_e \omega_0}} p \equiv -\frac{i}{\hbar} \delta x \cdot p,$$

where the pre-factor δx has dimensions of length. We immediately recognize the translation operator[58]

$$T(\delta x) = \exp \left\{ -\frac{i}{\hbar} \delta x \cdot p \right\}, \quad (4.18)$$

which means that the spin-vibron coupling effectively deforms the molecule, giving rise to the negative anisotropy contribution in Eq. (4.13).

The energy of each of these states is raised by the phonon occupation, so when analyzing the problem of transport at zero temperature, the most relevant of these states will be those of average occupation $\langle n \rangle = 0$. Comparing Eqs. (4.7) and (4.15), we see the splitting of the triplet due to the effective anisotropy term. The degeneracy can be recovered by increasing the static anisotropy up to $A_0 = A_1^2/\omega_0$ in order to make $\tilde{A} = 0$, and the hard-axis regime is reached by increasing it further, to positive values of \tilde{A} .

Once we have gained intuition on the atomic limit we can begin analyzing the break junction setup. Electrons of momentum \vec{k} and spin projection σ in the metallic band of the left (right) lead are represented by the fermionic operators $c_{L\vec{k}\sigma}$ ($c_{R\vec{k}\sigma}$) and $c_{L\vec{k}\sigma}^\dagger$ ($c_{R\vec{k}\sigma}^\dagger$). We add the diagonal term

$$H_E = \sum_{\alpha=L,R} \sum_{\vec{k}\sigma} \varepsilon_{\alpha\vec{k}} c_{\alpha\vec{k}\sigma}^\dagger c_{\alpha\vec{k}\sigma}, \quad (4.19)$$

where $\varepsilon_{L\vec{k}}$ ($\varepsilon_{R\vec{k}}$) is the band dispersion of the left (right) lead. The coupling between the molecule and the metallic band is given by

$$H_{M-E} = \sum_{\alpha=L,R} \sum_{\vec{k}\sigma} \left(V_\alpha d_{a\sigma}^\dagger c_{\alpha\vec{k}\sigma} + V_\alpha^* c_{\alpha\vec{k}\sigma}^\dagger d_{a\sigma} \right), \quad (4.20)$$

with the operators $d_{a\sigma}$ and $d_{a\sigma}^\dagger$ corresponding to level a . We simplify our calculation by assuming that the leads are identical ($\varepsilon_{L\vec{k}} = \varepsilon_{R\vec{k}} = \varepsilon_{\vec{k}}$) and that they have the same couplings to the molecule. We can also require that $V_L = V_R = V$ be real, so that $V^* = V$.

Being identical, the leads can only couple to the molecule in the symmetric combination

$$c_{\vec{k}\sigma} = \frac{1}{\sqrt{2}} (c_{L\vec{k}\sigma} + c_{R\vec{k}\sigma}). \quad (4.21)$$

If we define the complementary anti-symmetric operators

$$c_{\mathcal{A},k\sigma} := \frac{1}{\sqrt{2}} (c_{Lk\sigma} - c_{Rk\sigma}), \quad (4.22)$$

the diagonal term can be written as

$$H_E = \sum_{\vec{k}\sigma} \varepsilon_k (c_{k\sigma}^\dagger c_{k\sigma} + c_{\mathcal{A}k\sigma}^\dagger c_{\mathcal{A}k\sigma}). \quad (4.23)$$

The anti-symmetric operators contribute only an energy shift, since they do not hybridize with the molecule, and we may thus omit the second term of Eq. (4.23) in our calculations. The hybridization term becomes

$$H_{M-E} = \sqrt{2} V \sum_{\vec{k}\sigma} (d_{a\sigma}^\dagger c_{\vec{k}\sigma} + c_{\vec{k}\sigma}^\dagger d_{a\sigma}). \quad (4.24)$$

Furthermore, we can define the continuum-limit operator

$$c_\sigma = \frac{1}{N_k} \sum_{\vec{k}} c_{\vec{k}\sigma} \rightarrow \frac{1}{2D} \int_{-D}^{\varepsilon_F=0} d\varepsilon c_{\varepsilon\sigma}, \quad (4.25)$$

and its Hermitean conjugate, which respectively destroy and create an electronic state with components throughout all momenta. Here, $N_k \rightarrow 2D$ is the normalization coefficient of the band. In terms of this new operator, the hybridization term can be written as

$$H_{M-E} \frac{V}{\sqrt{2D}} \sum_{\sigma} (d_{a\sigma}^\dagger c_\sigma + c_\sigma^\dagger d_{a\sigma}). \quad (4.26)$$

One might be deceived into thinking that the Hamiltonian can now be diagonalized in terms of only four band operators. This is not the case, because it is impossible to simultaneously diagonalize the term Eq. (4.23) in terms of the operators c_σ and c_σ^\dagger .

We can keep the effective anisotropy picture by applying the unitary transformation Eq. (4.11) to the hybridization term (see Appendix A.1), resulting in the full transformed Hamiltonian

$$\tilde{H} = H_0 + H_E + \tilde{A} S_z^2 + \omega_0 b^\dagger b + \sum_{\sigma} \left(\tilde{V}_{\sigma} c_{\sigma}^{\dagger} d_{a\sigma} + \text{H. c.} \right), \quad (4.27)$$

with the definition

$$\tilde{V}_{\sigma} := \sqrt{2} V \exp \left\{ \frac{A_1}{4\omega_0} (a - a^{\dagger}) [1 - 2n_{a\bar{\sigma}} + 4\sigma S_z^b] \right\}, \quad (4.28)$$

where $n_{a\bar{\sigma}}$ represents the number operator of the opposite spin to σ in level a ; S_z^b is the spin projection operator of level b , and $\sigma = \pm 1$ for \uparrow / \downarrow , respectively. It is immediately obvious that the simple interpretation of the transformed Hamiltonian Eq. (4.12) does not carry well into Eq. (4.27) due to the new hybridization. It is not clear what the effect of the term given in Eq. (4.28) will be on the states of the new Hilbert space $\{\mathcal{H}_M \otimes \mathcal{H}_E\}$, but with some calculations we can determine that it basically introduces different hopping amplitudes between the band and the state $|T, 0\rangle$, than those between the band and the states $|T, \pm 1\rangle$, the latter being greater by a factor of the order of $\exp\{(A_1/\omega_0)^2\}$. This result is derived in Appendix A.2.

We can expect that this anisotropic hybridization will affect the splitting within the triplet as a further correction to \tilde{A} . In order to obtain an explicit form for this anisotropy we perform a Schrieffer–Wolff transformation[28]. This type of canonical transformation has proved useful for mapping Hamiltonians of the Anderson model family, like Eq. (4.24), onto Kondo–type Hamiltonians, which are well understood and whose parameters can be interpreted in a straightforward manner. This calculation is performed for our model, in the following section.

4.2 Mapping onto an anisotropic Kondo Hamiltonian

Let us assume that the system has been stretched so that for the isolated molecule the effective anisotropy is $\tilde{A} = 0$, and that we connect the molecule to the metallic leads. The total Hamiltonian for the molecule–leads system is given by

$$H = H_M + H_E + H_{M-E}. \quad (4.29)$$

The ground state of the decoupled Hamiltonian $H_0 + H_E$ is the molecular triplet with the full Fermi sea of the leads; we must determine exactly how this will change due to the hybridization between the two systems. Let us apply a canonical transformation to Eq. (4.29), in the form

$$\mathcal{U}_{S-W} = e^{i s}, \quad (4.30)$$

with s some Hermitean operator. The transformed Hamiltonian is

$$\begin{aligned} H_K := e^{i s} H e^{-i s} &= (H_M + H_E) + H_{M-E} + i ([s, H_M + H_E] + [s, H_{M-E}]) \\ &\quad - \frac{1}{2} [s, [s, H_M + H_E]] + \dots \end{aligned} \quad (4.31)$$

Knowing that it is processes of order s^2 that dominate the regime of high correlations, we may choose to eliminate all terms involving only one power of the generator s by setting

$$H_{M-E} = -i [s, H_M + H_E], \quad (4.32)$$

which leaves us with

$$H_K = (H_M + H_E) + \frac{i}{2} [s, H_{M-E}] + \mathcal{O}(s^3). \quad (4.33)$$

This procedure is known as a Schrieffer–Wolff transformation[28]. The following step is to determine the form of the generator s in the basis of the uncoupled molecule and leads. From Eq. (4.32) we obtain the generic matrix elements

$$\begin{aligned} \langle \alpha' | H_{M-E} | \alpha \rangle &= -i \langle \alpha' | [s, H_M + H_E] | \alpha \rangle \\ &= -i (\langle \alpha' | s | \alpha \rangle E_\alpha - E_{\alpha'} \langle \alpha' | s | \alpha \rangle), \end{aligned} \quad (4.34)$$

and finally

$$s_{\alpha\alpha'} = -i \frac{\langle \alpha' | H_{\text{M-E}} | \alpha \rangle}{E_{\alpha'} - E_{\alpha}}. \quad (4.35)$$

From this form of the generator we can obtain a general form of the corrections to the decoupled Hamiltonian $H_0 + H_E$. The diagonal elements are

$$\langle \alpha | \frac{i}{2} [s, H_{\text{M-E}}] | \alpha \rangle = \sum_{\beta} \frac{|\langle \beta | H_{\text{M-E}} | \alpha \rangle|^2}{E_{\alpha} - E_{\beta}}, \quad (4.36)$$

whereas non-diagonal elements are given by

$$\begin{aligned} \langle \alpha' | \frac{i}{2} [s, H_{\text{M-E}}] | \alpha \rangle = & \frac{1}{2} \sum_{\beta} \left\{ \frac{\langle \alpha' | H_{\text{M-E}} | \beta \rangle \langle \beta | H_{\text{M-E}} | \alpha \rangle}{E_{\alpha'} - E_{\beta}} \right. \\ & \left. + \frac{\langle \beta | H_{\text{M-E}} | \alpha \rangle \langle \alpha' | H_{\text{M-E}} | \beta \rangle}{E_{\alpha} - E_{\beta}} \right\}, \quad \alpha' \neq \alpha. \end{aligned} \quad (4.37)$$

Because our goal is to evaluate the low-temperature properties of the system, we limit ourselves to the sub-basis given by the states of half-filling, plus the states connected to them by $H_{\text{M-E}}$. They are listed in Table 4.2, along with their energies. There, we have defined the band states

$$|\sigma\rangle := c_{\sigma}^{\dagger} |\Omega\rangle = c_{\sigma}^{\dagger} \prod_{k < k_F} c_{k\uparrow}^{\dagger} c_{k\downarrow}^{\dagger} |0\rangle, \quad (4.38)$$

where the operator c_{σ}^{\dagger} is defined by Eq. (4.25). We number the states in the table in order to simplify the notation in subsequent calculations.

We now evaluate the diagonal elements of the term $(i/2) [s, H_{\text{M-E}}]$. For concreteness, we work in the electron-hole symmetric case of $\varepsilon = -U/2$, and we remind the reader that $\varepsilon_F = 0$. The detailed calculation is shown in Appendix A.3, but here we only show the resulting energy shift matrices:

$$\delta(T, +1; \tilde{n}) =$$

	$ \Omega\rangle T, +1; \tilde{n}\rangle$	$ \downarrow\rangle T, +1; \tilde{n}\rangle$	$ \uparrow\downarrow\rangle T, +1; \tilde{n}\rangle$	
$\langle T, +1; \tilde{n} \langle\Omega $	$2V^2 \sum_{m=0}^{\infty} \frac{ \langle\tilde{n} m\rangle ^2}{-\frac{U}{2}-\frac{J}{4}+(n-m)\omega_0}$	0	0	(4.39a)
$\langle T, +1; \tilde{n} \langle\downarrow $	0	$4V^2 \sum_{m=0}^{\infty} \frac{ \langle\tilde{n} m\rangle ^2}{-\frac{U}{2}-\frac{J}{4}+(n-m)\omega_0}$	0	
$\langle T, +1; \tilde{n} \langle\uparrow\downarrow $	0	0	$2V^2 \sum_{m=0}^{\infty} \frac{ \langle\tilde{n} m\rangle ^2}{-\frac{U}{2}-\frac{J}{4}+(n-m)\omega_0}$	

$$\delta(T, -1; \tilde{n}) =$$

	$ \Omega\rangle T, -1; \tilde{n}\rangle$	$ \uparrow\rangle T, -1; \tilde{n}\rangle$	$ \uparrow\downarrow\rangle T, -1; \tilde{n}\rangle$	
$\langle T, -1; \tilde{n} \langle\Omega $	$2V^2 \sum_{m=0}^{\infty} \frac{ \langle\tilde{n} m\rangle ^2}{-\frac{U}{2}-\frac{J}{4}+(n-m)\omega_0}$	0	0	(4.39b)
$\langle T, -1; \tilde{n} \langle\uparrow $	0	$4V^2 \sum_{m=0}^{\infty} \frac{ \langle\tilde{n} m\rangle ^2}{-\frac{U}{2}-\frac{J}{4}+(n-m)\omega_0}$	0	
$\langle T, -1; \tilde{n} \langle\uparrow\downarrow $	0	0	$2V^2 \sum_{m=0}^{\infty} \frac{ \langle\tilde{n} m\rangle ^2}{-\frac{U}{2}-\frac{J}{4}+(n-m)\omega_0}$	

	$ \Omega\rangle T, 0; n\rangle$	$ \uparrow\rangle T, 0; n\rangle$	$ \downarrow\rangle T, 0; n\rangle$	$ \uparrow\downarrow\rangle T, 0; n\rangle$	
$\delta(T, 0; n) = \langle T, 0; n \langle\Omega $	$\frac{2V^2}{-\frac{U}{2}-\frac{J}{4}}$	0	0	0	
$\langle T, 0; n \langle\uparrow $	0	$\frac{2V^2}{-\frac{U}{2}-\frac{J}{4}}$	0	0	(4.39c)
$\langle T, 0; n \langle\downarrow $	0	0	$\frac{2V^2}{-\frac{U}{2}-\frac{J}{4}}$	0	
$\langle T, 0; n \langle\uparrow\downarrow $	0	0	0	$\frac{2V^2}{-\frac{U}{2}-\frac{J}{4}}$	

We can also write these as operators in the form

$$\delta(T, 1; \tilde{n}) = \sum_{m=0}^{\infty} \frac{-2V^2 |(\tilde{n}| m)|^2}{\frac{U}{2} + \frac{J}{4} + (m-n)\omega_0} |T, 1; \tilde{n}\rangle \langle T, 1; \tilde{n}| \left(1 + 2n_{k_F} - n_{k_F}^2\right), \quad (4.40a)$$

$$\delta(T, -1; \tilde{n}) = \sum_{m=0}^{\infty} \frac{-2V^2 |(\tilde{n}| m)|^2}{\frac{U}{2} + \frac{J}{4} + (m-n)\omega_0} |T, -1; \tilde{n}\rangle \langle T, -1; \tilde{n}| \left(1 + 2n_{k_F} - n_{k_F}^2\right), \quad (4.40b)$$

$$\delta(T, 0; n) = \frac{-2V^2}{\frac{U}{2} + \frac{J}{4}} |T, 0; n\rangle \langle T, 0; n| \mathbf{1}_{4 \times 4}. \quad (4.40c)$$

The energy shift for the states involving the molecular doublet and a single electron in the band at the Fermi level is double that of the cases with zero or double occupation in the band. This is because in the former states electrons can hop from the leads to the molecule, and vice versa, whereas in the latter the electron can only hop in one direction. The lower energy states involving the doublet will thus have single occupation in the leads at the Fermi level.

In order to sort the shifted states from lower to higher energy, we need to evaluate the term $|(\tilde{n}| m)|^2$. The ground state has $\langle n \rangle = 0$, and all states with $n > 0$ are phonon excitations, so the important term to be calculated is

$$|(\tilde{n}| m)|^2 = \left(\frac{A_1}{\omega_0}\right)^{2m} \frac{e^{-\left(\frac{A_1}{\omega_0}\right)^2}}{m!}. \quad (4.41)$$

This is exponentially smaller than 1, for $|A_1/\omega_0| > 1$, and in general the shift

$\delta(T, \pm 1; \tilde{0}) < \delta(T, 0; 0)$. The different energy shifts give rise to a new anisotropy term

$$A_d := 2V^2 \left(\frac{1}{\frac{U}{2} + \frac{J}{4}} - \sum_{m=0}^{\infty} \frac{2|(\tilde{n}| m)|^2}{\frac{U}{2} + \frac{J}{4} + m\omega_0} \right) > 0, \quad (4.42)$$

due to the phonon-induced anisotropic hybridization. This anisotropy separates the 4-fold degenerate ground state with zero molecular spin projection, from the 2-fold degenerate

Label	State	Energy
1, n	$ \Omega\rangle T, +1; \tilde{n}\rangle$	$E(T, +1; \tilde{n}) = 2\varepsilon - \frac{J}{4} + \varepsilon_F n \omega_0$
2, n	$ \downarrow\rangle T, +1; \tilde{n}\rangle$	$E(T, +1; \tilde{n}) = 2\varepsilon - \frac{J}{4} + \varepsilon_F n \omega_0$
3, n	$ \uparrow\downarrow\rangle T, +1; \tilde{n}\rangle$	$E(T, +1; \tilde{n}) = 2\varepsilon - \frac{J}{4} + 2\varepsilon_F + n \omega_0$
4, n	$ \Omega\rangle T, -1; \tilde{n}\rangle$	$E(T, -1; \tilde{n}) = 2\varepsilon - \frac{J}{4} + \varepsilon_F + n \omega_0$
5, n	$ \uparrow\rangle T, -1; \tilde{n}\rangle$	$E(T, -1; \tilde{n}) = 2\varepsilon - \frac{J}{4} + \varepsilon_F + n \omega_0$
6, n	$ \uparrow\downarrow\rangle T, -1; \tilde{n}\rangle$	$E(T, -1; \tilde{n}) = 2\varepsilon - \frac{J}{4} + 2\varepsilon_F + n \omega_0$
7, n	$ \Omega\rangle T, 0; n\rangle$	$E(T, 0; n) = 2\varepsilon - \frac{J}{4} + \varepsilon_F + n \omega_0$
8, n	$ \uparrow\rangle T, 0; n\rangle$	$E(T, 0; n) = 2\varepsilon - \frac{J}{4} + \varepsilon_F + n \omega_0$
9, n	$ \downarrow\rangle T, 0; n\rangle$	$E(T, 0; n) = 2\varepsilon - \frac{J}{4} + \varepsilon_F + n \omega_0$
10, n	$ \uparrow\downarrow\rangle T, 0; n\rangle$	$E(T, 0; n) = 2\varepsilon - \frac{J}{4} + \varepsilon_F + n \omega_0$
11, n	$ \sigma\rangle 0_a, \sigma_b\rangle n\rangle$	$E(0_a, \sigma_b) = \varepsilon + \varepsilon_F + n \omega_0$
12, n	$ \bar{\sigma}\rangle 0_a, \sigma_b\rangle n\rangle$	$E(0_a, \sigma_b) = \varepsilon + \varepsilon_F + n \omega_0$
13, n	$ \uparrow\downarrow\rangle 0_a, \sigma_b\rangle n\rangle$	$E(0_a, \sigma_b) = \varepsilon + \varepsilon_F + n \omega_0$
14, n	$ \Omega\rangle \uparrow\downarrow_a, \sigma_b\rangle n\rangle$	$E(\uparrow\downarrow_a, \sigma_b; n) = 3\varepsilon + U + n \omega_0$
15, n	$ \uparrow\rangle \uparrow\downarrow_a, \sigma_b\rangle n\rangle$	$E(\uparrow\downarrow_a, \sigma_b; n) = 3\varepsilon + U + \varepsilon_F + n \omega_0$
16, n	$ \downarrow\rangle \uparrow\downarrow_a, \sigma_b\rangle n\rangle$	$E(\uparrow\downarrow_a, \sigma_b; n) = 3\varepsilon + U + \varepsilon_F + n \omega_0$

Table 4.3: List of states in the sub-basis considered in the calculation of the Kondo Hamiltonian.

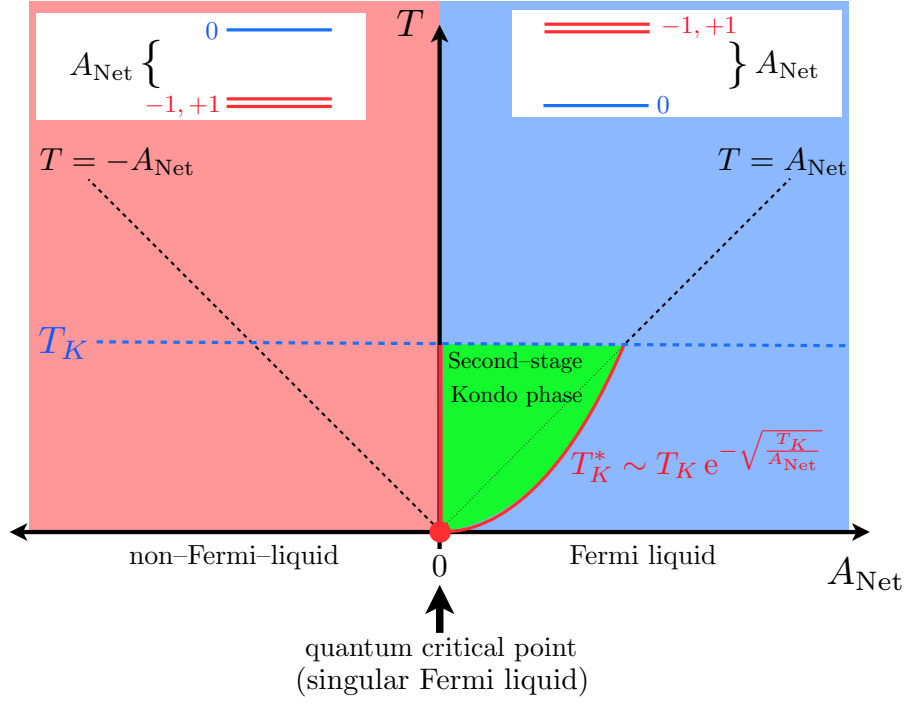


Figure 4.3: Phase diagram of the spin-1 molecular system, with dynamic anisotropy. The red region represents a non-Fermi-liquid phase where transport is dominated by inelastic scattering of electrons off the molecular doublet. The blue region represents normal Fermi liquid behavior, and the green region corresponds to the singular Fermi liquid phase of the second-stage Kondo state. Red lines indicate quantum criticality.

states of the molecular doublet with single occupation at the Fermi level. This contribution introduces a small shift toward the hard-axis regime into the system's net effective anisotropy

$$A_{\text{eff}} = A_0 - \frac{A_1^2}{\omega_0} + A_d. \quad (4.43)$$

One last contribution to the anisotropy will arise from the non-diagonal corrections, as we will now see: The non diagonal corrections can be written as operators in the following way:

$$O_z = J_K^{\parallel} s_z S_z, \quad (4.44a)$$

$$O_{\text{flip}} = J_K^{\perp} (s_x S_x + s_y S_y), \quad (4.44b)$$

with s_x, s_y, s_z the spin operators of the molecule, S_x, S_y, S_z the spin operators of the band, and the Kondo coupling constants

$$J_K^\parallel := \sum_{m=0}^{\infty} \frac{4V^2 \left| \langle m | \tilde{0} \rangle \right|^2}{\frac{U}{2} + \frac{J}{4} + m\omega_0}, \quad J_K^\perp := e^{-\left(\frac{A_1}{\omega_0}\right)^2 / 2} J_K^0, \quad (4.45)$$

with $J_K^0 = 4V^2 / (U/2 + J/4)$ the Kondo coupling of the system without phonons. This Kondo Hamiltonian is anisotropic, in the sense that there are two different Kondo couplings $J_K^\parallel \neq J_K^\perp$, corresponding to the transport axis and the transverse plane, respectively. As pointed out in Ref. [49], there is a direct correspondence between anisotropic Kondo couplings and magnetic anisotropy. By means of NRG calculations, they show that our case of $J_K^\parallel > J_K^\perp > 0$ will give rise to a negative contribution to the net anisotropy, $\delta A < 0$. The shift, however, is small ($\lesssim T_K^0$) and has not been evaluated analytically to the best of our knowledge.

The total Hamiltonian can finally be written as

$$H_K = H_0 + H_E + \omega_0 b^\dagger b + A_{\text{eff}} S_z^2 + J_K^\parallel S_z S_z + J_K^\perp (s_x S_x + s_y S_y). \quad (4.46)$$

Our achievements so far are the following:

1. We have mapped a generic, Anderson-type Hamiltonian with both a static and a phonon-dependent anisotropy term, into a Kondo-type Hamiltonian with anisotropic couplings and a magnetic anisotropy term.
2. Because Kondo Hamiltonians have been so extensively studied, we understand the effects of the spin-vibron coupling that we introduced: first, that the Kondo temperature of the system will be reduced because J_K^\parallel and J_K^\perp are exponentially smaller than J_K^0 . Second, that there will be a net dynamic anisotropy $A_{\text{Net}} = A_{\text{eff}} + \delta A$.
3. As we discussed earlier, the anisotropy will tune the ground state of the system, leading to different quantum phases, and naturally quantum phase transitions.

From this work, the phase diagram of Fig. 4.3 was obtained. The second Kondo stage at $A_{\text{Net}} \ll T_K$ served as confirmation that in fact our final model Eq. (4.46) is correct. By determining the Kondo temperature $T_K < T_K^0$ of the system with phonons, we verified Eq. (4.3) to convince ourselves that no other effect— at least no effect capable of destroying the fragile second Kondo stage— was taking place. We substituted T_K^0 with T_K , as obtained from our NRG calculations, and evaluated A_{Net} to substitute into the equation. The result is shown in Fig. 4.4(c), and it clearly shows that our results fit the form Eq. (4.3).

Now that we have a clear picture of the Hamiltonian, we can study electronic transport through the system.

4.3 Conductance calculations

As mentioned earlier, a system of this kind can be studied by means of standard transport measurements. In this section we will show that each one of the quantum phases driven by the net anisotropy A_{Net} presents clear signatures in the system's zero bias conductance that can be resolved by experiments similar to those of Ref. [8].

Coherent transport through the system occurs at zero bias when a sharp molecular level coincides with the band's Fermi level. If the molecular level is at higher or lower energy, transport is only possible if the energy gap $|\varepsilon - \varepsilon_F|$ is closed by applying a bias voltage V_b to the molecule, which would lift its energy levels to $\varepsilon + V_b$, or if temperature excitations allow for the electrons to hop to or from the level.

Our study considers only the latter case. We have obtained finite temperature results from our NRG calculations following the method proposed by Bulla *et al.*, in Refs. [40, 41]. The conductance through the system is given by the formula[59, 60]

$$\frac{G(T)}{G_0} = \pi\Gamma \int_{-\infty}^{\infty} d\omega \left(-\frac{\partial f(\omega, T)}{\partial \omega} \right) \rho_a(\omega), \quad (4.47)$$

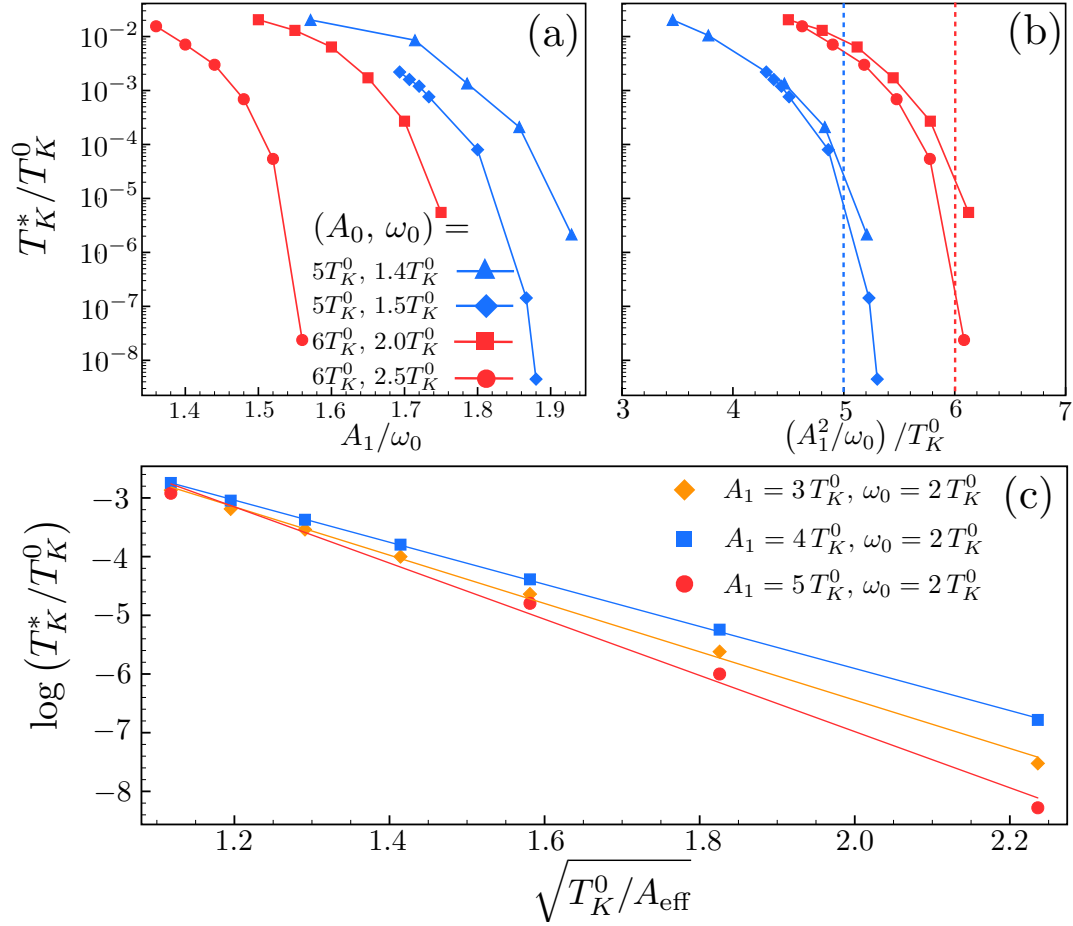


Figure 4.4: (a) Second-stage Kondo temperature T_K^* obtained by means of NRG calculations for different anisotropies, keeping A_0 constant. For $A_1/\omega_0 = 0$, the net anisotropy is positive but small, giving rise to the second stage of screening at temperatures of only $0.1 T_K^0$. The fast fall of the curves with increasing A_1/ω_0 indicates that A_{Net}/ω_0 is being shifted toward zero, and then negative values. (b) The value of the shift can be estimated as the distance between the respective dotted lines and the asymptotes that the curves follow. (c) Fitting the values of T_K^* to the form of Eq. (4.3). The applicability of this equation in all the cases shown is verified by the fact that the curves are straight lines.

where $G_0 = 2e^2/h$ is the quantum of conductance, $\Gamma = \pi |V|^2 / 2D$ is the hybridization between the molecule and the leads, $f(\omega, T)$ is the Fermi–Dirac distribution

$$f(\omega, T) = \frac{1}{\exp\{(\omega - \varepsilon_F)/T\} + 1}, \quad (4.48)$$

for energy ω and temperature T , and $\rho(\omega) = \sum_{\sigma} \rho_a^{\sigma}(\omega)$ is the total spectral density at level a . A clarification on units is in order: throughout this document we treat the temperature as an energy scale measured in energy units (specifically, in terms of the half–bandwidth D), and the Boltzmann constant k_B will not appear in our formulas. By specifying a temperature in units of D and D in electron–volts, the temperature can be obtained in Kelvins as $T \cdot D / (8.6173 \times 10^{-5})$. That is, obtaining $T_K^0 = 10^{-5} D$ with a bandwidth of $D = 10 \text{ eV}$, we have $T_K^0 = 1.1604 \text{ K}$, which is reasonable for a spin–1 Kondo effect.

It is also important to mention that Γ , rather than V , is the relevant energy unit from the point of view of electronic transport. This is because Γ gives the broadening of the molecular levels due to the hybridization with the band; the relative size of this broadening and the energy gap $|\varepsilon - \varepsilon_F|$ determines the conductance through Eq. (4.47).

In order to evaluate the conductance through Eq. (4.47) we evaluated the spectral density by means of NRG calculations (see Chapter 3). The NRG runs were performed with discretization parameter $\Lambda = 2.5$, and we kept approximately 1200 states after every iteration (more were kept when truncating at 1200 broke any symmetries of the Hamiltonian). The system was kept in the electron–hole symmetric case of $\varepsilon = -U/2 = -5\Gamma$, with hybridization $\Gamma = 0.005 D$, and we used a Hund’s rule strength of $J = 0.2\Gamma$. Our conclusions remain valid for other parameters, as long as we stay in the Kondo regime ($\varepsilon < 0$, $\Gamma < |\varepsilon|$, $U \gtrsim |\varepsilon|$). We verified this with numerical calculations.

The bosonic sector of the Hilbert space is infinite–dimensional, and we need to truncate it to an appropriate value for the numerical calculation. We choose to work in the regime of $\omega_0 \gtrsim T_K^0$ and $A_1/\omega_0 < 1$. Transition amplitudes from zero to n phonon

occupation are given by Eq. (4.41), which is a Poisson distribution[61] that peaks at $n = A_1/\omega_0 < 1$, suggesting a cutoff at $n \sim 1$. We ran multiple tests to verify this assertion, and found that a maximum occupation 3 phonons correctly describes the behavior of the system, as indicated by full convergence of the NRG calculations.

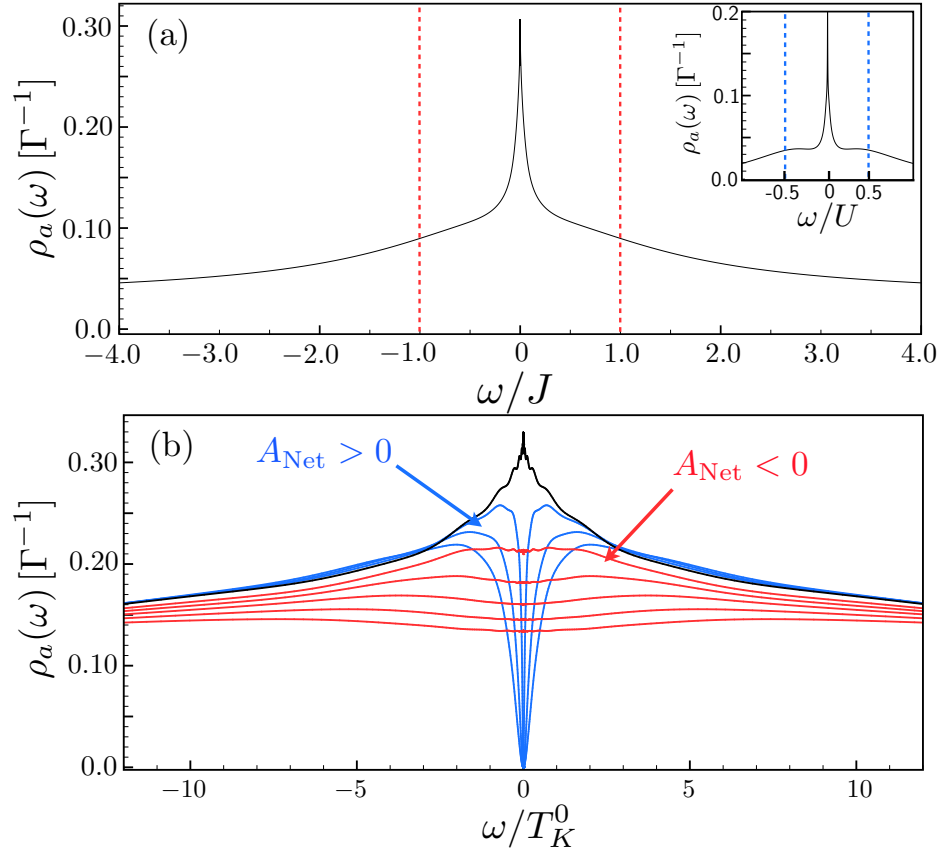


Figure 4.5: Total spectral density at the molecular level a . (a) For the case of $A_0 = A_1 = 0$, the spin-1 Kondo effect has a Kondo temperature $T_K^0 = 1 \times 10^{-5} D$, for the current parameters. (b) Keeping $A_0 = \omega_0 = 5 T_K^0$, we vary A_1 from $2 T_K^0$ to $11 T_K^0$, tuning the value of A_{Net} from positive (blue curves) to negative values (red curves). The black curve shows the Kondo effect for $A_{\text{Net}} = 0$. Extracted from Ref.[12].

We start by obtaining the reference energy scale T_K^0 , corresponding to the case of $A_0 = A_1 = 0$. We do so from the curve of the spectral density, shown in Fig. 4.5(a). The

different energy scales can be appreciated in the figure: The dotted red lines are placed at energies $\omega = \pm J$ and they coincide with two bumps, corresponding to excitations from the triplet to the singlet; the blue dotted lines in the inset are placed at $\omega = \pm U$, coinciding with “bumps” corresponding to charge excitations. The sharp peak at $\omega = \varepsilon_F = 0$ is a signature of the Kondo state, and its width gives us a value of $T_K^0 \approx 1 \times 10^{-5} D$.

We now start tuning A_0 and A_1 . In Fig. 4.5(b) we show how the spectral density changes as we change the anisotropy. The curves shown are for $A_0 = \omega_0 = 5 T_K^0$, and we vary A_1 from $2 T_K^0$ to $11 T_K^0$. The value of A_{Net} is positive for the curves at lower A_1 (blue curves), and as we increase A_1 the net anisotropy goes to zero (black curve) and eventually to negative values (red curves). The same color convention will be used in all future plots.

As can be seen in Fig. 4.5(b), the red curves show a finite amplitude of ρ_a at the Fermi level, meaning that the conductance is finite, although not unitary. Figures 4.6(a) and (b) show conductance curves for this case in red. As depicted in Fig. 4.3, in this (easy-axis) regime the ground state of the molecule is the doublet $|T, \pm 1\rangle$. The electrons in the leads will scatter inelastically off of the doublet, leading to many-particle low-energy excitations, which by definition are not of the Fermi-liquid type[49]: this regime is a non-Fermi liquid.

The blue curves in Figs. 4.5(b), corresponding to the hard-axis regime, show a pseudo-gap⁸ at the Fermi level. Conductance at zero temperature vanishes, as seen in Figs. 4.6(a) and (b), since there are no states available for transport. All charge excitations in this phase are single-particle like: this is a Fermi liquid phase.

As for the case of $A_{\text{Net}} = 0$, the spin-1 Kondo state is known as a singular Fermi liquid, called this way because it exhibits single-particle low energy excitations like a Fermi liquid, but also presents singularities in its density of states, which produce

⁸ A vanishing density of states “at a single point” (for a single energy value) is commonly known as a pseudo-gap, as opposed to a real gap, where the density of states vanishes for a whole range of energies. Examples of pseudo-gaps are found in systems such as high-Tc superconductors[62] and graphene[63].

divergent thermodynamic quantities such as the specific heat. A description of a singular Fermi liquid is out of the scope of this document, and we refer the reader to Ref. [64] for more details on the subject.

The appearance of the Kondo effect produces what is called unitary conductance: the Kondo peak of height $1/(\pi\Gamma)$ at the Fermi level (black curve in Fig. 4.5) maximizes the integral in Eq. (4.47), and the conductance goes to G_0 as $T \rightarrow 0$ (black curve in Figs. 4.6(a) and (b)). It is worthwhile mentioning that the Kondo temperature for Fig. 4.6(b) is $T_K \approx 0.1 T_K^0$.

The conductance-vs.-temperature curves are not easy to obtain in an experimental setup. Typical experiments on these systems are performed at a constant temperature, usually of the order of a few Kelvin. A useful curve to see from the experimentalist's point of view would be that of conductance-vs.-stretching, or equivalently vs. A_0 , at constant temperature. We cut Fig. 4.6(b) at different temperatures indicated by green, orange and purple dotted lines, crossing the conductance curves corresponding to different values of A_0 . The isotherms of corresponding colors, as well as other intermediate cases, are shown in Fig. 4.6(c). It is reasonable to assume the phonon frequency and the spin-vibron coupling to be properties of the system, so we fix them to the value $\omega_0 = A_1 = 5 T_K^0$. We start in the non-Fermi-liquid phase, and by increasing A_0 we approach $A_{\text{Net}} = 0$, which slowly raises the conductance up to the unitary regime. By further increasing A_0 we get into the Fermi liquid phase, and the conductance suddenly drops. As we can see in Fig. 4.6(c), the drop is more sudden at lower temperatures because temperature-driven excitations become less probable.

If a curve of this kind were obtained from the experiment of Parks *et al.*, the maximum of conductance would appear at zero stretching, and thus $A_0 = 0$. In our case, the signature of the spin-vibron coupling is the conductance slowly dropping again as A_0

is lowered further. The dynamic correction to the molecule's anisotropy, $A_1^2/\omega_0 + A_d + \delta A$, is given by the value of A_0 at which the conductance peaks at low temperature.

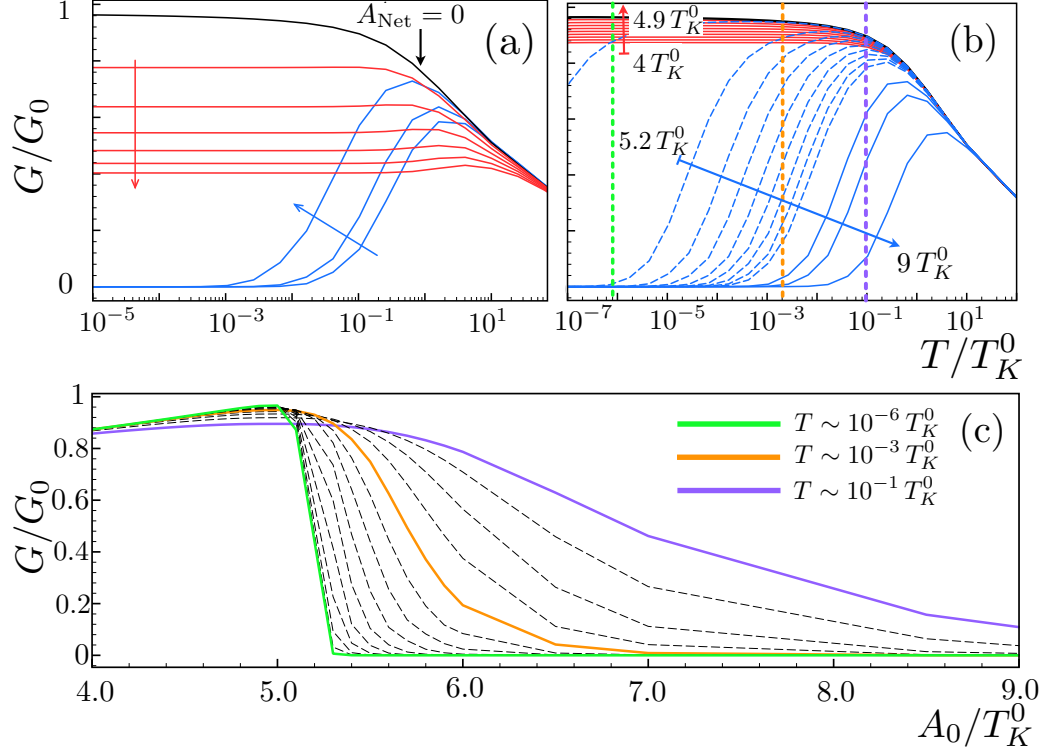


Figure 4.6: (a) Zero-bias conductance as a function of temperature, for different values of the net anisotropy, A_{Net} . Varying A_1 from $2 T_K^0$ through $12 T_K^0$ for fixed $\omega_0 = A_0 = 5 T_K^0$, the net anisotropy goes from positive to negative. (b) Same as (a), but with fixed $A_1 = \omega_0 = 5 T_K^0$, and A_0 going from $4 T_K^0$ to $9 T_K^0$. The net anisotropy goes from negative to positive. This is analogous to what would happen if the molecule were stretched as in the experiment of Ref. [8]. (c) Conductance isotherms, as a function of stretching (A_0). Colored curves correspond to constant temperatures, as indicated by the dotted lines in (b).

4.4 Effective magnetic moment calculations

To conclude this discussion we present our results for the effective magnetic moment of the break junction system. According to Curie's law, the effective magnetic moment

squared is given by

$$\mu^2 := T \chi(T), \quad (4.49)$$

with $\chi(T)$ the magnetic susceptibility at temperature T . In the more common spin-1/2 Kondo effect, the effective anti-ferromagnetic interaction (the Kondo coupling) between the impurity's spin and the band allows for the full band, which can actually be seen as a spin-1/2 fermion as defined in Eq. (4.25), to screen the magnetic moment of $\mu = 1/2$ of the molecule, at zero temperature. This can be seen by plotting μ^2 vs. temperature: as $T \rightarrow 0$, μ^2 drops from a value of about 1/4 at high temperature, to zero right below the spin-1/2 Kondo temperature.

For a spin-1 object the situation is similar, except that at high temperature the system has $\mu^2 \approx 1$, and at below T_K it plateaus at $\mu = 1/4$, because the band can only screen one half of the total magnetic moment. This is shown in Fig. 4.7, where the black, dashed line corresponds to the spin-1 Kondo effect.

The remaining magnetic moment can be associated to an asymptotically free magnetic impurity that remains decoupled from the strongly-coupled Kondo singlet. As mentioned earlier, a small anisotropy $0 < A_{\text{Net}} \lesssim T_K^0$ will open another screening channel by coupling this asymptotically free object to the Kondo singlet, which has Fermi liquid properties. This produces a second stage of Kondo, very similar to a spin-1/2 Kondo effect, but a much lower Kondo temperature, T_K^* . This interpretation was obtained in Ref. [55] by means of a mean-field calculation known as slave-boson mean-field theory. The blue curves in Fig. 4.7 corresponding to the hard-axis regime verify this behavior: while large, positive values of A_{Net} leave a ground state with zero magnetic moment even at $T \gtrsim T_K$, small A_{Net} will open the second screening channel at low temperatures. The corresponding blue curves begin close to the 0.25 plateau at $T \sim T_K$, and fall to zero as the temperature is reduced, indicating that the full magnetic moment has been screened.

The easy-axis regime is very different. When the molecule-band interaction is dominated by inelastic scattering, the magnetic screening is reduced and μ^2 plateaus at values above 0.25. The larger the negative anisotropy is, the higher the plateau will be, with an upper limit of 1 when screening is prevented altogether. This is shown by the red, solid lines in Fig. 4.7.

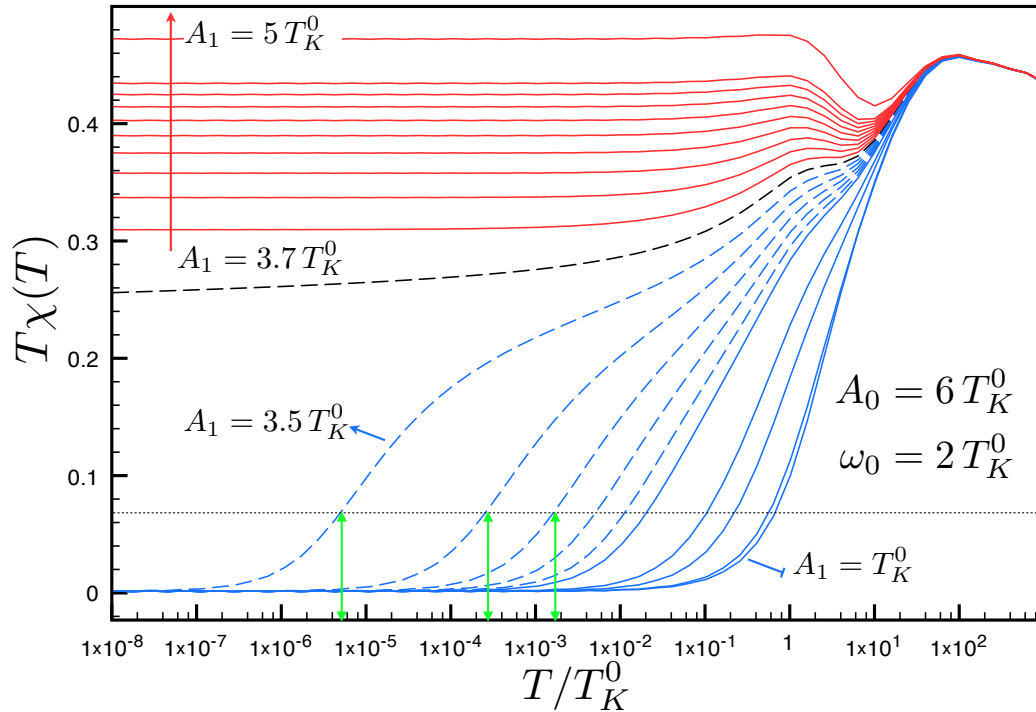


Figure 4.7: Effective magnetic moment squared of the system, as a function of temperature, for fixed $\omega_0 = 2 T_K^0$ and $A_0 = 6 T_K^0$, varying A_1 from T_K^0 to $5 T_K^0$. The second stage of screening is treated as a regular spin-1/2 Kondo effect, and we use Wilson's threshold[24] of $\mu^2 = 0.707$ to define its temperature scale T_K^* . The green arrows show this temperature for their corresponding curves. Extracted from Ref.[12].

Finally, in Figs. 4.8(a) and (c) we map $\mu^2(T = 0)$ as a function of the two molecular parameters, ω_0 and A_1 , for constant A_0 . A clear separation of the two phases is observed: the blue region corresponds to $\mu^2 = 0$, while the red region corresponds to $\mu^2 > 0.25$. The

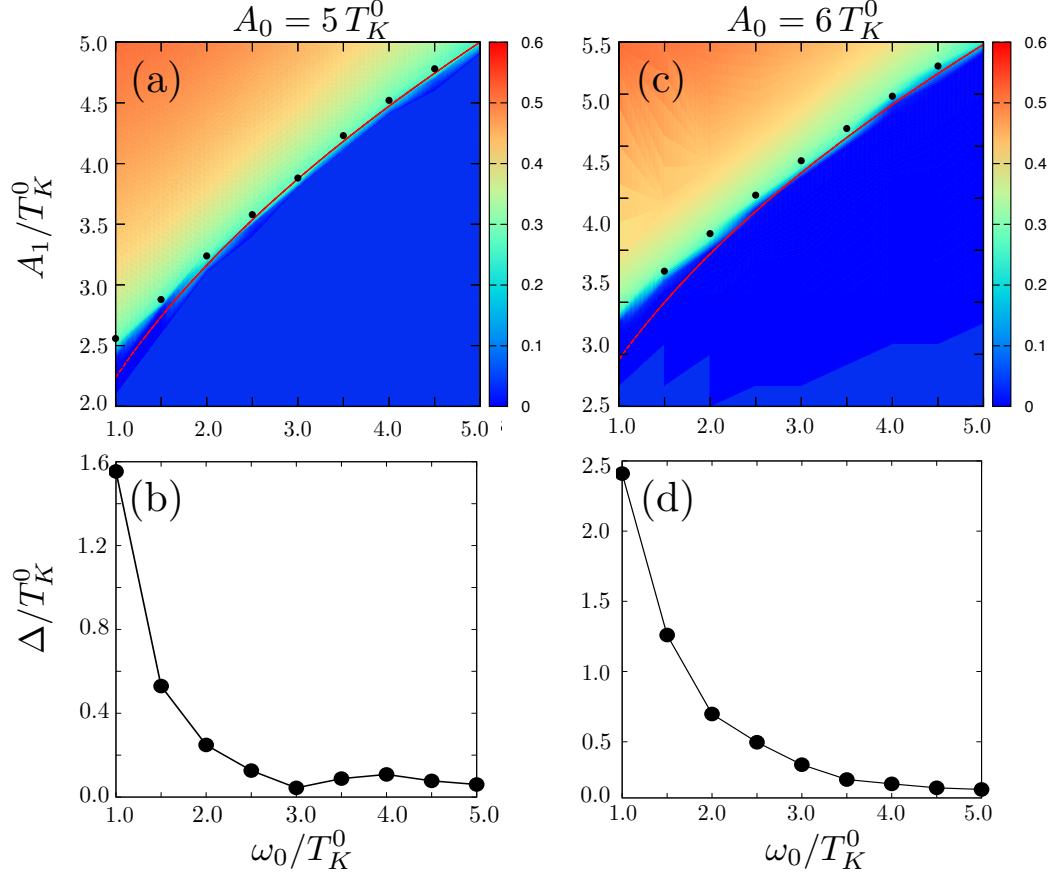


Figure 4.8: Maps of μ^2 as a function of ω_0 and A_1 , for (a) $A_0 = 5 T_K^0$ and (c) $A_0 = 6 T_K^0$. The black dots indicate the value of A_1 at which $A_{\text{Net}} = 0$ for each ω_0 . The red curve indicates the value of A_1 for which $\tilde{A} = 0$. The difference between these two gives the correction $\Delta = A_d + \delta A$, shown in (b) and (d) underneath their corresponding maps. Extracted from Ref.[12].

green crossover line appears at $\mu^2 = 0.25$, when A_{Net} is exactly zero. We define

$\Delta := A_{\text{Net}} - \tilde{A} = A_d + \delta A$, and identify A_{Net} with the green region in the plots. This way, we can evaluate Δ , and we plot it below their corresponding maps in Figs. 4.8(b) and (d). We can appreciate how Δ falls off exponentially with ω_0 , in agreement with Eqs. (4.41) and (4.42).

4.5 Conclusions

In this chapter we have discussed the behavior of a deformable spin-1 molecule deposited in a break junction, and which has a vibration mode along the junction's transport axis. This system exhibits Kondo physics, which we have studied by means of analytical techniques such as Schrieffer-Wolff transformations, as well as NRG calculations. We concluded from this analysis that the spin-vibron coupling in this system reduces the Kondo temperature, introduces corrections to the magnetic anisotropy, and produces an anisotropic hybridization between the band and the ground state of the molecule.

We have obtained an effective anisotropic Kondo Hamiltonian with a magnetic anisotropy term of the form $A_{\text{eff}} S_z^2$, which correctly describes the thermodynamics and transport properties of the system at low temperatures, as verified by our numerical results. We determined that the net anisotropy can be used to tune the ground state, in order to explore three quantum phases: a non-Fermi-liquid phase in the easy-axis regime, a singular Fermi liquid in the Kondo regime, and a Fermi liquid phase in the hard-axis regime. The resulting phase diagram is presented in Fig. 4.3

We have presented signatures of the different phases, from the magnetic properties of the system to its transport features. Conductance curves have been produced, which can serve as guide to experimentalists interested in testing our theory in spin-1 molecules with soft vibrational modes.

5 DECOHERENCE EFFECTS OF A CHARGE DETECTOR ON A NEARBY QUANTUM DOT

5.1 Introduction

One of the prototypical thought experiments invoked when discussing complementarity in quantum mechanics is the double-slit experiment: electrons are fired from an emitter, one by one, through two identical slits and onto a detector. While classical mechanics predicts the detection of electrons only in the vicinity of each slit, the wave nature of electrons manifests itself as an interference pattern all across the detector. On the other hand, if one were to place another detector between the electron source and the double slit in order to ascertain the path of the electron, the interference pattern would be progressively destroyed as the accuracy of the measurement is increased.

With the advances in semiconductor physics during the last few decades, performing this experiment has become possible in materials with the use of what is known as a “which-way” (*welcher Weg*) detector. Figure 5.1 shows the experimental setup of Reference [65], where two paths have been traced in a 2DEG produced in a GaAs-AlGaAs interface, by means of voltages applied through metallic gates deposited on top of the heterostructure. The right path contains an electron detector, consisting of a QD through which the electron must go in order to reach the collector (marked C), and a QPC placed nearby.

In the particle picture, whenever an electron goes through the path on the right, it must “hop” into the QD; the proximity of the QPC allows for the electron in the QD to raise the potential landscape within the QPC, directly affecting its conductance properties, making the electron passing through the QD “visible”[66]. As reported in Ref. [65], the expected destruction of the interference pattern at the collector is observed.

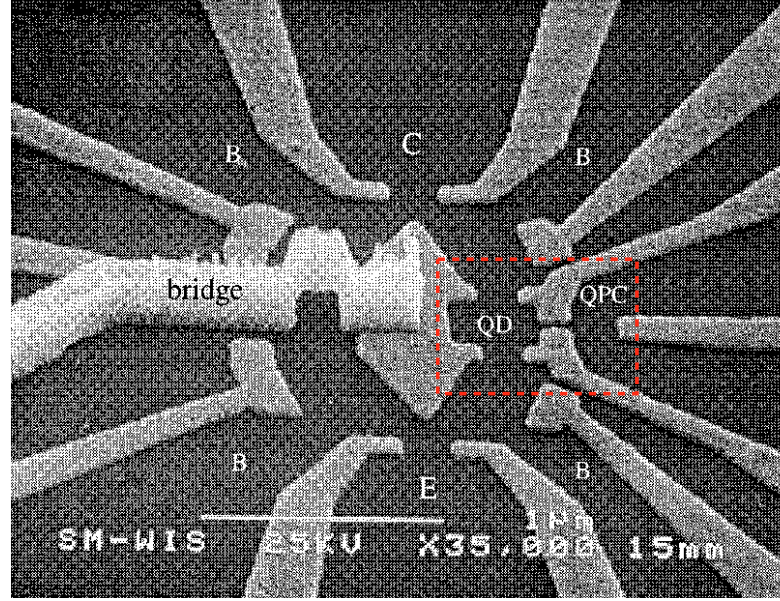


Figure 5.1: Experimental setup of Ref. [65]. The two-slit experiment is performed on a 2DEG produced at the interface of a semiconductor heterostructure, and a “which-way” detector consisting of a QD capacitively coupled to a QPC on one of the paths. (Extracted from Ref. [65], with permission of Nature Publishing Group)

Our attention, however, goes to the detector itself: how does the presence of a nearby QPC affect the ground state of a QD, particularly within the Kondo regime? Theoretical studies of this coupled system[67, 68] predicted a suppression of the unitary conductance characteristic of the Kondo regime, due to shot noise by electrons traveling through the QPC under a bias V_{QPC} through a process known as decoherence[69]. This consists of the destruction of the relative phases of the electronic wave functions due to the interaction with an external system; in this case, the QPC. The suppression α of the conductance G through the QD, defined as $\Delta G := -\alpha G(V_{QPC} = 0)$, is calculated by means of slave-boson mean-field theory to be[67]

$$\alpha = \frac{eV_{QPC}}{8\pi} \frac{(\Delta t)^2/T_K}{t(1-t)}, \quad (5.1)$$

with T_K the Kondo temperature of the QD, e the electronic charge, t the transmission probability through the QPC, and Δt the change in t upon adding an electron to the QD. However, this prediction clashed with experimental evidence presented in Reference [70] by Avinun–Kalish *et al.*, where the measured suppression was a whole order of magnitude larger than predicted by Eq. (5.1), and clearly showed an additional feature at $t \sim 0.7$.

This additional feature raised some interest in the problem, due to the fact that the number $t = 0.7$ is rather special in the study of electronic transport through QPCs. They have a very particular conductance profile due to the lateral confinement, which restricts the transverse wave numbers to a discrete spectrum; as a consequence, the transport channels are separated by energy steps, producing a step–like conductance curve as a function of gate voltage V_g . A cartoon of this situation is shown in Fig. 5.2.

Experiments, however, have consistently shown an unexpected intermediate plateau of conductance $G = 0.7G_0$ right when a vanishing conductance is expected[71] (red dashed lines in Fig. 5.2); this has come to be known as the “0.7 anomaly”. Many explanations have been proposed for this phenomenon, some of which invoke the relevance of electron–electron interactions within the constriction, while others attribute this unexpected behavior to an anomalous enhancement of potential scattering within the QPC, due to certain features of the local density of states[72]. None of these are considered in the derivation of Eq. (5.1).

One of the most widely accepted explanations was proposed by Y. Meir, based on the findings of T. Rejec and Y. Meir[73, 74]: Utilizing first–principle calculations (spin–density–functional theory), they were able to show under fairly general conditions the formation of an impurity–like, localized spin-1/2 electronic state within the constriction which is thought to undergo Kondo screening upon coupling to the metallic terminals of the QPC.

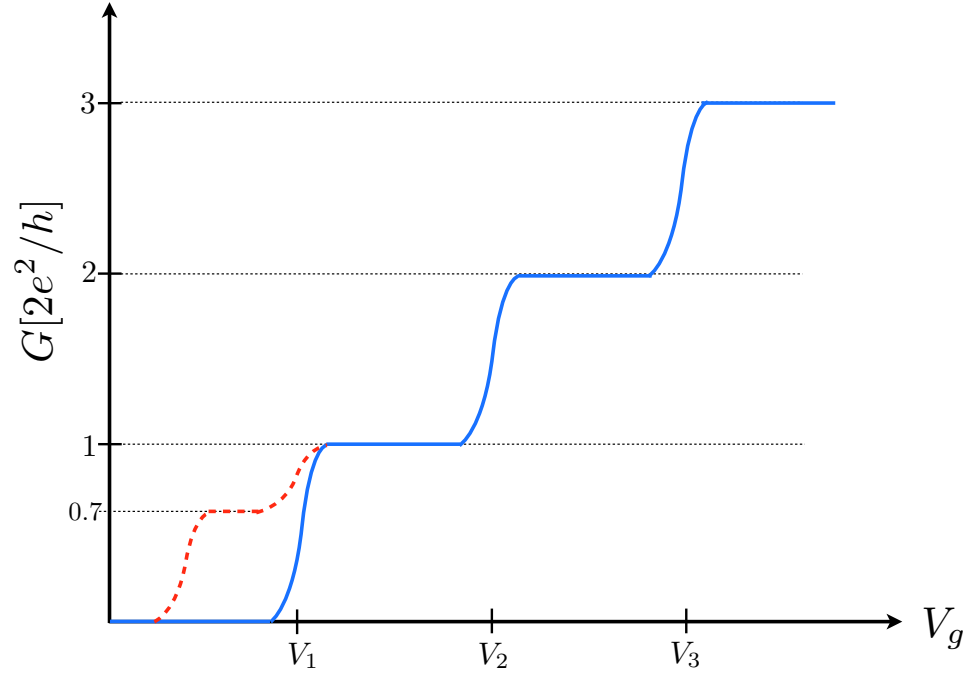


Figure 5.2: Depiction of the zero-bias conductance profile of a typical QPC, as a function of gate voltage. Larger V_g effectively increases the width W of the constriction, changing the number $N \sim 4\pi k_F W$ of transverse modes that can propagate at the Fermi level (k_F is the Fermi momentum). The red dashed line represents the so-called “0.7 anomaly”.

By modeling this localized state through a SIAM with a charge-dependent hybridization, Y. Meir *et al.* were able to show the appearance of an anomalous conductance plateau at approximately $0.7 G_0$, using perturbation theory[75]. They attribute the appearance of this intermediate plateau to the two effective conduction channels— each able to contribute a maximum conductance of $G_0/2$ — produced by the localized state within the QPC, which appear due to the charge-dependent hybridizations: As the gate voltage V_g is increased up to approximately the localized state’s energy, the first channel is filled and the conductance increases by $G_0/2$, while the second channel is only partially filled, leading to an additional fractional conductance contribution of approximately $0.2G_0$, producing the $0.7 G_0$ plateau.

Using the impurity model by Meir *et al.* and the transmission measurements of Avinun-Kalish *et al.*, T. Aono was able to produce a theoretical curve for the conductance suppression due to decoherence from the interaction with the QPC using the perturbative treatment of Ref. [68], correctly reproducing the additional peak in the suppression at $t \sim 0.7$. In Ref. [13], Aono attributes the observed two-peak structure to induced dephasing from the two conduction channels produced by the localized state within the QPC; he presents a suppression given by

$$\alpha = \frac{eV_g}{8\pi} [\alpha_0(t_1) + \alpha_0(t_2)], \quad (5.2)$$

with t_1 and t_2 the transmissions of the two transport channels of the localized state in the QPC, and $\alpha_0(t_i)$ it the dephasing rate of each channel. Aono's findings strongly support Meir's model.

Inspired by these studies, we set out to perform a fully non-perturbative calculation of the effects of a charge-detector QPC on a QD in the Kondo regime, in the small-gate limit for the QPC. By modeling Rejec's and Meir's localized state within the QPC as a secondary QD which couples capacitively to the primary QD, we are able to study the effects of equilibrium quantum fluctuations in the former, on the latter, through zero-bias conductance calculations using the NRG method. Furthermore, we explore different parameter configurations that lead to direct competition between the Kondo ground states of both QDs, leading to quantum phase transitions between the different transport regimes. We perform a fully analytical variational calculation that describes this competition to a good approximation, and provides a deeper insight to the NRG results.

5.2 Variational calculation of the Kondo ground state of the SIAM

In Chapter 3 the effective ground state of the $s - d$ model and the SIAM were described as a *many-body singlet* formed by the localized magnetic moment and the spins from the itinerant electrons in the band. This assertion was proven by the exact

diagonalization of the Kondo Hamiltonian[25, 26], and can be verified by analyzing spin–spin correlation functions between the impurity site and the electronic band, from NRG results.

We are satisfied, however, with the plausibility of the statement: The $s - d$ model is based on a ferro– or antiferromagnetic interaction between the impurity’s spin, and that of the band; the Kondo effect results only from the latter case. For only two spins, the ground state of such interaction would be a singlet. Furthermore, our NRG results for the magnetic susceptibility and entropy (Fig. 3.6) reveal that the ground state in the SCFP has only one effective state, with vanishing magnetic moment.

Following similar arguments, Varma and Yafet proposed a generic variational singlet form for the ground state of the SIAM with infinite U in order to study the magnetic susceptibility of rare–earth compounds[76]. For a single impurity, the ground state has the form

$$|\Psi\rangle = \alpha_0 |\Omega\rangle + \sum_{\sigma, \vec{k}} \alpha_k d_{\sigma}^{\dagger} c_{\vec{k}\sigma} |\Omega\rangle, \quad (5.3)$$

where ε_d is the energy of the impurity level, $|\Omega\rangle$ is the direct product of the Fermi–liquid ground state of the leads and the empty impurity site, given by

$$|\Omega\rangle = \prod_{k < k_F} c_{\vec{k}\uparrow}^{\dagger} c_{\vec{k}\downarrow}^{\dagger} |0\rangle, \quad (5.4)$$

and the coefficients α_0 and $\{\alpha_k\}$ are variational parameters. Each α_k is assumed to depend only upon the magnitude of the momentum because of spherical symmetry. For concreteness, let us work specifically with a QD between two identical metallic terminals—a source and a drain—and we remind the reader that in this situation the operators $c_{\vec{k}\sigma}$ correspond to the symmetric combination of the two (see discussion in Section 4.1). The ground state of Eq. (5.3) contains a many–body singlet (second term), and a finite projection to the state of zero occupation of the d level. We could in principle include an additional term for double occupation, but for the sake of simplicity we have decided to

work in the limit of infinite U , where the probability amplitude for this state vanishes. For our purposes, there is no loss of generality.

The energy of the ground state Eq. (5.3) is obtained by evaluating the expectation value of the SIAM over Eq. (5.3), and is a functional of the variational parameters given by

$$E[\alpha] = \frac{\langle \Psi | H_{\text{SIAM}} | \Psi \rangle}{\langle \Psi | \Psi \rangle} = \frac{2 \sum_{\vec{k} < k_F} \{ (\varepsilon_d - \varepsilon_k) \alpha_k^2 + 2V \alpha_0 \alpha_k \}}{\langle \Psi | \Psi \rangle}. \quad (5.5)$$

This is only the impurity contribution to the system energy; a term $(2 \sum_{k < k_F} \varepsilon_k)$ for the energy of the band has been subtracted in Eq. (5.5). In order for Eq. (5.3) to be the ground state, the variational parameters must be tuned so that $E[\alpha]$ is at its minimum value. We thus require that

$$\frac{\partial}{\partial \alpha_0} E[\alpha] = \frac{\partial}{\partial \alpha_k} E[\alpha] = 0, \quad (5.6)$$

leading to the variational equations

$$\alpha_0 E = 2V \sum_{k < k_F} \alpha_k, \quad (5.7a)$$

$$\alpha_k [E - (\varepsilon_d - \varepsilon_k)] = \alpha_0 V, \quad (5.7b)$$

which put together yield the relation

$$E = 2 \sum_{k < k_F} \frac{V^2}{E - \varepsilon_d + \varepsilon_k}. \quad (5.8)$$

Knowing *a priori* that the band will “dress” the impurity state and renormalize the level energy, we write the ground state energy as

$$E := \varepsilon_d - \Delta, \quad (5.9)$$

with the shift $\Delta > 0$. Equation (5.8) takes the form

$$\varepsilon_d - \Delta = 2 \sum_{k < k_F} \frac{V^2}{\Delta + \varepsilon_k}. \quad (5.10)$$

In order to make progress, we take the continuum limit in momentum and change variables from momentum to energy, leading to

$$\sum_{k < k_F} \rightarrow \int_{-D}^0 \rho(\varepsilon) d\varepsilon,$$

where, just like in Chapter 4, the Fermi energy has been set to $\varepsilon_F = 0$, $D > 0$ is the half-bandwidth of states that couple to the impurity, and the density of states (for a flat band) is $\rho(\varepsilon) = 1/2D$. By considering that $\varepsilon_k < 0$ for all \vec{k} in the sum, we can write

$$\sum_{k < k_F} \frac{2V^2}{\Delta - |\varepsilon_k|} \rightarrow -\frac{V^2}{D} \int_0^D \frac{d\varepsilon}{\varepsilon - \Delta} = \frac{V^2}{D} \log \left\{ \frac{|\Delta|}{|D - \Delta|} \right\}, \quad (5.11)$$

leading to the transcendental equation

$$\varepsilon_d - \Delta = \frac{V^2}{D} \log \left\{ \frac{\Delta}{D - \Delta} \right\}, \quad (5.12)$$

where the absolute values have been removed, since we expect $0 < \Delta \ll D$.

In general, the solution to Eq. (5.12) has to be calculated numerically. But let us treat the case of a Coulomb blockade, with $\varepsilon_d < 0$, $|\varepsilon_d| \gg \Gamma (= \pi V^2/2D)$, and assume that the shift Δ is small compared to $|\varepsilon_d|$, and consequently to D . This last requirement is reasonable, because one would expect that a hybridization Γ of the level to the band would cause an energy shift no larger than Γ itself. In this approximation, Eq. (5.12) can be solved analytically by the function

$$\Delta(\varepsilon_d, V) = D \exp \left\{ -|\varepsilon_d| D/V^2 \right\}. \quad (5.13)$$

Figure 5.3 shows a comparison between the numerical solution to Eq. (5.12) and the analytical approximation Eq. (5.13), for $V = 0.0357 D$ ($\Gamma = 0.002 D$), and $-0.025 D < \varepsilon_d < 0 D$. As expected, they are equivalent for ε_d negative and large enough.

Compare Eq. (5.13) to Eq. (2.6): in the present case of a flat density of states, and in the limit of infinite U , Eq. (2.7) gives $J \sim V^2/\varepsilon_d$. Substituting into Eq. (2.6) we obtain

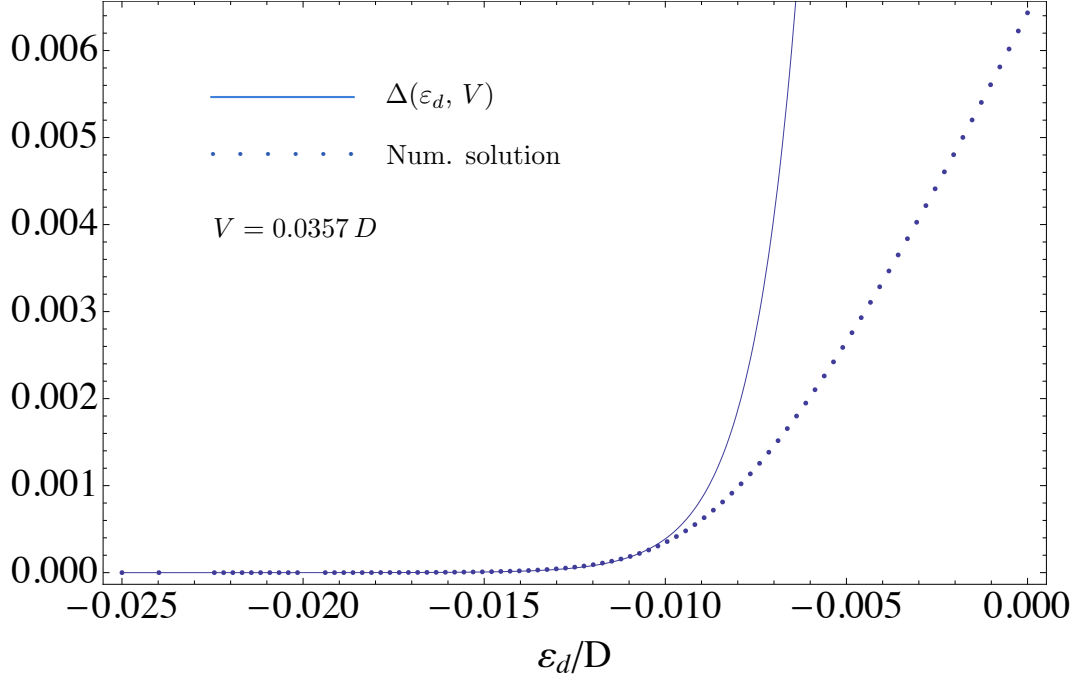


Figure 5.3: Comparison between the numerical solution to Eq. (5.12), and the approximate solution Eq. (5.13). All parameters in units of the half bandwidth D .

precisely Eq. (5.13). The equivalence between the Kondo temperature and the energy shift Δ suggests that the proposed ground state corresponds to the Kondo ground state in this parameter regime.

Armed with the numerical solution to Eq. (5.12), we can solve for all the amplitudes⁹:

$$\alpha_k = \frac{\alpha_0 V}{\varepsilon_k - \Delta}, \quad (5.14a)$$

$$\alpha_0 = \sqrt{\frac{\Delta (\Delta + D)}{\Delta (\Delta + D) + V^2}}. \quad (5.14b)$$

⁹ The full calculation is shown in Appendix B.

With knowledge of the ground state wave function, we are able to calculate any expectation value, including the charge and charge fluctuations of the QD, defined by

$$Q := \langle \Psi | n_d | \Psi \rangle / \langle \Psi | \Psi \rangle = 2 \sum_{k < k_F} \alpha_k^2 \quad (5.15)$$

$$\chi_Q^2 := \left[\langle \Psi | n_d^2 | \Psi \rangle - \langle \Psi | n_d | \Psi \rangle^2 \right] / \langle \Psi | \Psi \rangle = Q - Q^2,$$

with the normalization condition $\langle \Psi | \Psi \rangle = 1$. Figure 5.4(a) shows these expectation values calculated numerically by solving Eq. (5.12) and substituting into Eq. (5.15), and the same quantities evaluated using the NRG. There is a clear difference between the curves obtained with the two methods, particularly obvious in the position of the fluctuations' peaks. This is attributed to the fact that the variational calculation corresponds to the case $U \rightarrow \infty$, whereas in the NRG calculations U is a finite parameter. The interaction U renormalizes the impurity level, bringing it closer to the Fermi energy of the leads; when the renormalized level is in resonance with the Fermi level the charge fluctuations peak. This happens for negative ε_d , and the exact value depends on the strength of the intra-dot Coulomb interaction, U ; hence, the different positions of the peaks in the figure. For larger values of U there is a better agreement between the analytical results and the NRG calculation, as can be seen in the figure.

5.3 Variational calculation of the ground state of two capacitively-coupled QDs

When two QDs, labeled q and d , are placed sufficiently close to each other, it is possible for the electrons occupying their localized states to “feel” each other through electrostatic repulsion, introducing an additional energy cost for the simultaneous occupation of the QDs.

In the same spirit as the Hubbard term for the intra dot Coulomb repulsion, we parameterize the inter dot repulsion via the term

$$u n_q n_d, \quad (5.16)$$

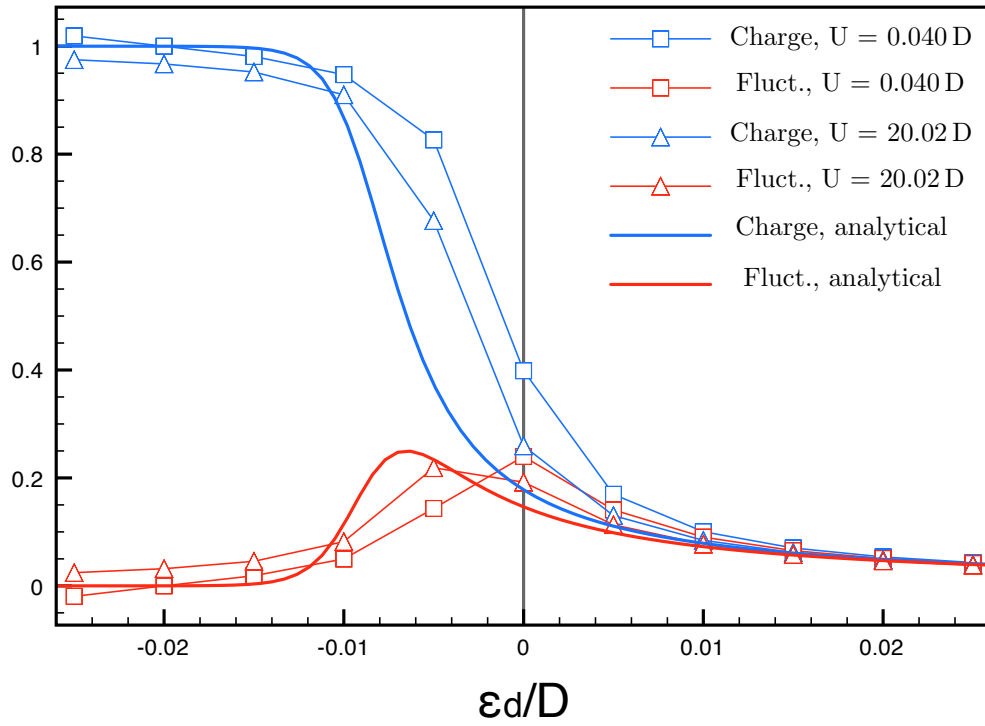


Figure 5.4: Charge and charge fluctuations within a QD, as a function of gate voltage (ϵ_d): comparison between variational solution and NRG results. The NRG results approach the variational solution for $U \gg D$. Parameters: $\Gamma = 0.002 D$.

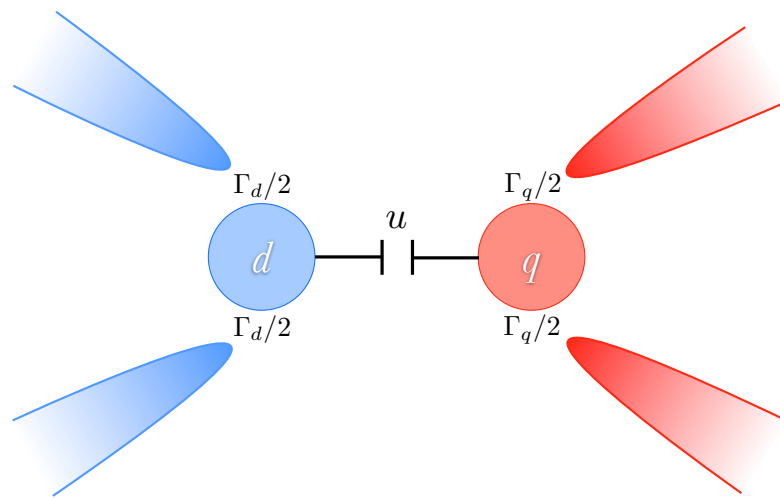


Figure 5.5: Capacitively-coupled quantum dots, d and q .

where the number operator $n_i = \sum_{\sigma} n_{i\sigma}$ corresponds to dot $i = q, d$. The full Hamiltonian for the coupled system is then given by

$$H = H_q + H_d + u n_q n_d, \quad (5.17)$$

with

$$H_q = \varepsilon_q n_q + U_q n_{q\uparrow} n_{q\downarrow} + V_q \sum_{\vec{k}\sigma} \left\{ q_{\sigma}^{\dagger} c_{q\vec{k}\sigma} + \text{H. c.} \right\}, \quad (5.18a)$$

$$H_d = \varepsilon_d n_d + U_d n_{d\uparrow} n_{d\downarrow} + V_d \sum_{\vec{k}\sigma} \left\{ d_{\sigma}^{\dagger} c_{d\vec{k}\sigma} + \text{H. c.} \right\}. \quad (5.18b)$$

The operators d_{σ} and q_{σ} correspond to the level at quantum dot d and q , respectively. We emphasize that each QD is connected to an independent set of metallic leads, whose operators are denoted $c_{i\vec{k}\sigma}$, and there is no charge exchange between them. This Hamiltonian has been studied in the case of $\varepsilon_d = \varepsilon_q$, $U_d = U_q$, $V_d = V_q$ for electron–hole symmetry in Refs. [77–79], in the limits of $u/U_i \ll 1$, $u/U_i = 1$ and $u/U \gg 1$. In this study, however, we are interested in the case of $u \lesssim |\varepsilon_d|, |\varepsilon_q|$, and in general for different parameters of dots q and d : regimes that are very relevant (and more realistic) for experimental situations.

Analogous to Eq. (5.3), we propose a variational ground state

$$|\Psi\rangle := |\psi_q\rangle |\psi_d\rangle = \left[\alpha_0 + \sum_{\vec{k}\sigma} \alpha_k q_{\sigma}^{\dagger} c_{q\vec{k}\sigma} \right] \left[\beta_0 + \sum_{\vec{k}\sigma} \beta_k d_{\sigma}^{\dagger} c_{d\vec{k}\sigma} \right] |\Omega\rangle, \quad (5.19)$$

with

$$|\Omega\rangle := \left[\prod_{k < k_F} c_{q\vec{k}\uparrow}^{\dagger} c_{q\vec{k}\downarrow}^{\dagger} \right] \left[\prod_{k' < k_F} c_{d\vec{k}'\uparrow}^{\dagger} c_{d\vec{k}'\downarrow}^{\dagger} \right] |0\rangle. \quad (5.20)$$

For our purposes, we can assume that the two sets of leads are identical, and thus both have the same Fermi momentum, k_F . Evaluating the variational coefficients of Eq. (5.19) would not only give us physical insight into the system ground state: Although the NRG method is highly reliable for obtaining a full description of the ground state, as we will see below, the two–channel version required to treat both impurities requires a large amount

of computer resources, and the intuition gained from this variational calculation saved us valuable computing time.

Again, in the spirit of Eq. (5.5), we evaluate the energy functional of the state Eq. (5.19) and obtain

$$E[\alpha, \beta] := \frac{2 \sum_{k < k_F} \{(\varepsilon_q - \varepsilon_k) \alpha_k^2 + 2V \alpha_0 \alpha_k\}}{\langle \psi_q \rangle} + \frac{2 \sum_{k < k_F} \{(\varepsilon_d - \varepsilon_k) \beta_k^2 + 2V \beta_0 \beta_k\}}{\langle \psi_d \rangle} \\ + u \frac{(2 \sum_{k < k_F} \alpha_k^2)(2 \sum_{k < k_F} \beta_k^2)}{\langle \psi_q \rangle \langle \psi_d \rangle}. \quad (5.21)$$

The impurity energy terms have the exact same form as in the single-impurity problem, so we can abbreviate Eq. (5.21) as

$$E[\alpha, \beta] = E_q[\alpha] + E_d[\beta] + \tilde{u}[\alpha, \beta], \quad (5.22)$$

with the definition

$$\tilde{u} = u \frac{(2 \sum_{k < k_F} \alpha_k^2)(2 \sum_{k < k_F} \beta_k^2)}{\langle \psi_q \rangle \langle \psi_d \rangle}. \quad (5.23)$$

The variational equations for the coupled system are

$$2V_q \sum_{k' < k_F} \alpha_{k'} = \alpha_0 (E_q + \tilde{u}), \quad (5.24a)$$

$$\alpha_0 V_q = \alpha_k \left[E_q - (\varepsilon_q - \varepsilon_k) - u \frac{\alpha_0^2 (2 \sum_{k' < k_F} \beta_k^2)}{\langle \Psi \rangle} \right], \quad (5.24b)$$

$$2V_d \sum_{k' < k_F} \beta_{k'} = \beta_0 (E_d + \tilde{u}), \quad (5.24c)$$

$$\beta_0 V_d = \beta_k \left[E_d - (\varepsilon_d - \varepsilon_k) - u \frac{\beta_0^2 (2 \sum_{k' < k_F} \alpha_k^2)}{\langle \Psi \rangle} \right]. \quad (5.24d)$$

From the point of view of one of the QDs, the charge of the other acts as an external gate that raises the energy levels in the same way as a gate voltage, the effect of this being a shift in the ground state energy of the QD. Bearing this in mind and looking at Eqs.

(5.24b) and (5.24d), we propose a relation similar to Eq. (5.7b) for each of the QDs:

$$\alpha_k = \frac{\alpha_0 V_q}{\varepsilon_k - \varepsilon_q + E_q - \Lambda_q}, \quad (5.25a)$$

$$\beta_k = \frac{\beta_0 V_d}{\varepsilon_k - \varepsilon_d + E_d - \Lambda_d}, \quad (5.25b)$$

where the terms Λ_i contains the energy shift from the remote gate, while the Kondo energy scale of each dot is encoded in E_i . We substitute Eqs. (5.25a) and (5.25b) into Eqs. (5.24a) and (5.24c), respectively, and by taking the continuum limit for the flat band case we obtain the equations

$$\frac{V_q^2}{D} \log \left\{ \frac{\varepsilon_q - E_q + \Lambda_q}{\varepsilon_q - E_q + D + \Lambda_q} \right\} = E_q + u \frac{X_q X_d}{(1 + X_q)(1 + X_d)}, \quad (5.26a)$$

$$\frac{V_d^2}{D} \log \left\{ \frac{\varepsilon_d - E_d + \Lambda_d}{\varepsilon_d - E_d + D + \Lambda_d} \right\} = E_d + u \frac{X_q X_d}{(1 + X_q)(1 + X_d)}, \quad (5.26b)$$

where we introduce the short-hand notation

$$\alpha_0^2 X_q := 2 \sum_{k < k_F} \alpha_k^2 \longrightarrow X_q = \frac{V_q^2}{(\varepsilon_q - E_q + \Lambda_q)(\varepsilon_q - E_q + D + \Lambda_q)}, \quad (5.27)$$

and the corresponding expression for X_d .

Equations (5.26a) and (5.26b) contain a total of four unknowns (E_i and Λ_i). In order to solve the system, we make use of the constraint

$$\Lambda_d = u \frac{X_q}{(1 + X_q)(1 + X_d)}, \quad (5.28a)$$

$$\Lambda_q = u \frac{X_d}{(1 + X_q)(1 + X_d)}, \quad (5.28b)$$

coming from comparing the ansatz Eqs. (5.25a) and (5.25b) to variational equations (5.24b) and (5.24d). With this, the mutual capacitance contribution to the energy can be written as

$$\tilde{u} = \Lambda_d X_d = \Lambda_q X_q, \quad (5.29)$$

casting the system of equations in the form

$$\frac{V_q^2}{D} \log \left\{ \frac{\varepsilon_q - E_q + \Lambda_q}{\varepsilon_q - E_q + D + \Lambda_q} \right\} = E_q + u \Lambda_q X_q, \quad (5.30a)$$

$$\frac{V_d^2}{D} \log \left\{ \frac{\varepsilon_d - E_d + \Lambda_d}{\varepsilon_d - E_d + D + \Lambda_d} \right\} = E_d + u \Lambda_d X_d. \quad (5.30b)$$

Putting together Eqs. (5.28a) and Eqs. (5.28b) we obtain

$$X_d^2 + X_d \left(1 + \frac{\Lambda_q - u}{\Lambda_d} \right) + \frac{\Lambda_q}{\Lambda_d} = 0, \quad (5.31)$$

and a similar equation for X_q by simply exchanging the labels q and d . We have two possible branches for the solution of Eq. (5.31), given by

$$X_d^\pm = -\frac{1}{2} \left(1 + \frac{\Lambda_q - u}{\Lambda_d} \right) \pm \frac{1}{2} \sqrt{\left(1 + \frac{\Lambda_q - u}{\Lambda_d} \right)^2 - 4 \frac{\Lambda_q}{\Lambda_d}}. \quad (5.32)$$

Because X_i^\pm have the physical meaning of charge (or rather, the expectation value of a number operator), we demand that the solution be real and positive, yielding the conditions

$$u + \Lambda_q + 2\sqrt{u\Lambda_q} < \Lambda_d < u + \Lambda_q - 2\sqrt{u\Lambda_q} \quad ; \quad \Lambda_d, \Lambda_q \geq 0. \quad (5.33)$$

Secondly, X_i^\pm must simultaneously satisfy Eq. (5.27), which means that the ground state energies must be given by

$$E_i^\pm = \varepsilon_i + \Lambda_i + \frac{D}{2} \pm \sqrt{\left(\frac{D}{2} \right)^2 + \frac{V_i^2}{X_i^\pm}}, \quad (5.34)$$

which is always real-valued for real and positive X_i^\pm . Finally, we want the logarithms in Eqs. (5.30a) and (5.30b) to be well defined, and so both the numerator and denominator must be of the same sign. We can immediately eliminate the possibility of both being negative, because that would imply that $|\varepsilon_i - E_i + \Lambda_i| > D$. In order for both to be positive, we require

$$E_i < \varepsilon_i + \Lambda_i, \quad \text{and} \quad E_i < \varepsilon_i + D + \Lambda_i. \quad (5.35)$$

Now that E_i are written as functions only of Λ_i , we finally have a system of two coupled equations for two unknowns, albeit not one that is extremely well behaved.

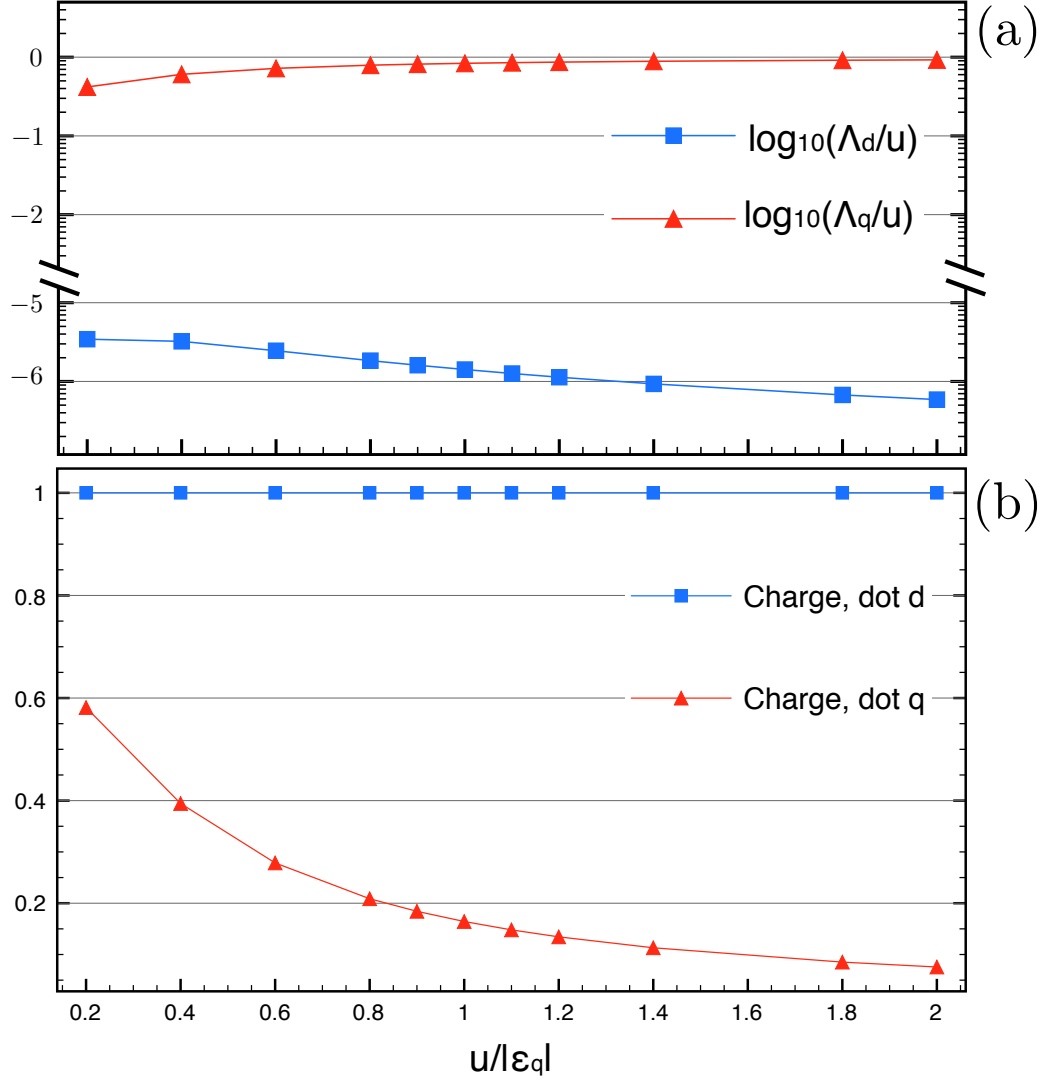


Figure 5.6: (a) Solutions to Eqs. (5.30a) and (5.30b), for fixed QD parameters and varying u . Parameters are: $\varepsilon_d = -0.025 D$, $\varepsilon_q = -0.010 D$, $\Gamma_q = \Gamma_d = 0.002 D$; $u \in [0, 2|\varepsilon_q|]$. (b) Variational calculation of the charge in dots d and q (blue and red, respectively).

Equations (5.30a) and (5.30b) can be solved by means of numerical methods; in Figure 5.6(a) we show the solutions for the case of two QDs with fixed parameters

$\varepsilon_d = -0.025 D$, $\varepsilon_q = -0.010 D$, $\Gamma_q = \Gamma_d = 0.002 D$, varying the capacitive coupling

$u \in [0, 2|\varepsilon_q|]$ (solutions found in the branch of X_i^+ and E_i^-). There is a noticeable trend for

$\Lambda_q \rightarrow u$ and $\Lambda_d \rightarrow 0$, as u is increased; that is, for larger u , dot d acts less as a dynamical object and more as a distant gate on q . Being that u reaches $2|\varepsilon_q|$, this gate in fact raises the energy level in dot q above the Fermi level and depletes it, as can be seen in Figure 5.6(b).

The analytical results can be compared to NRG calculations. Figure 5.7 shows side by side the spectral densities of both QDs for these parameters (in the NRG calculation, $U_d = U_q = 0.05 D$), and the gating on q can be appreciated through the increasing asymmetry of the curves in (b). The Hubbard bands (see Section 3.3) represent the energy of the impurity at single (left) and double (right) occupation, shifted and dressed by the interactions. Thus, the shifting of the negative peak toward positive values with increasing u suggests the presence of a gate voltage, which for large u is basically equal to u , according to the solutions presented in Figure 5.6. The Hubbard peak at $\omega \approx 0.01 D = \varepsilon_q + u$ is in perfect agreement with this picture. The inset in Figure 5.7(b) shows the same curves for $\omega/D > 0$ in a logarithmic scale in order to appreciate the SCFP value of the spectral density. When the gated level $\varepsilon_q + \Lambda_q < 0$ and $|\varepsilon_q + \Lambda_q| \gg \Gamma_q$, q is in the Kondo regime, but as soon as q enters the mixed-valence regime ($|\varepsilon_q + \Lambda_q| \sim \Gamma_q$) the charge fluctuations within the dot begin to quench the Kondo effect, lowering the Kondo temperature T_K^q and reducing the amplitude of the Kondo peak, as can be seen in the figure.

As for dot d , a gating effect is appreciated for small u which shifts the left Hubbard band slightly to the right, as indicated by the dashed arrows. Notice, however, that the curve tends to return to its original shape of $u = 0$ (bold black line), for $u > 0.008 D$; that is, when the gating effect begins to deplete dot q . The curve does not quite get there, however, indicating a small residual asymmetry due to the coupling to dot q . We notice also that for $u > 0.008 D$ the distance between the Hubbard peaks becomes smaller than $U_d = 0.050 D$. This gives us an opportunity to discuss the level structure of the problem in

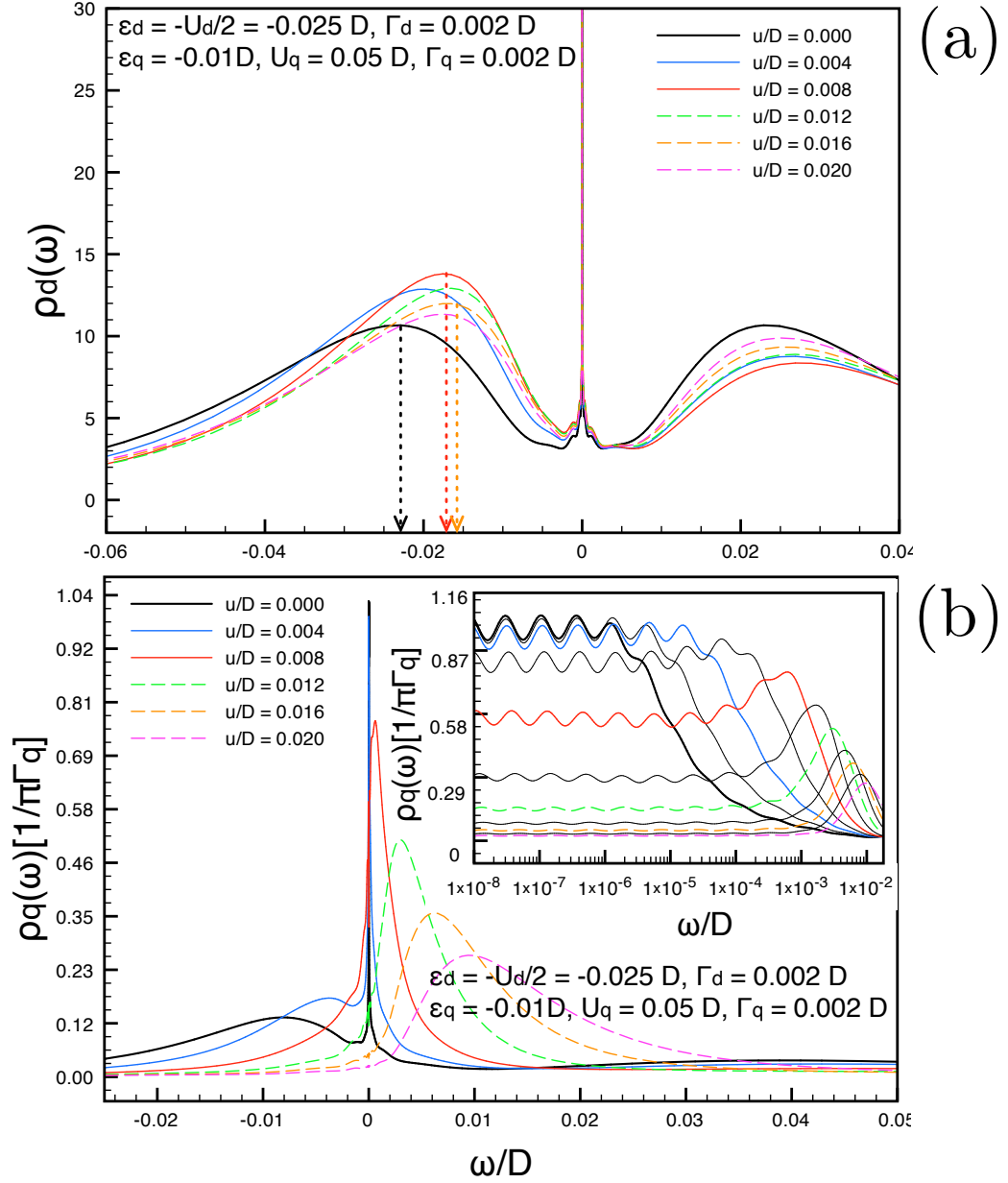


Figure 5.7: Spectral densities for QDs d and q ((a) and (b), respectively) for the parameters of Fig. 5.6, evaluated using NRG. At zero temperature, this amplitude is equivalent to the zero-bias conductance, in units of $2e/h^2$. The inset in (b) shows the spectral density of dot q in a logarithmic scale for positive ω . The oscillations in the curves for small ω are due to the discreteness of the states considered in the NRG calculation.

some detail[77, 78]: At the energy scale of the Hubbard peaks the system is close to the FOFP, and so the system can be discussed in terms of the Hamiltonian with $\Gamma_i = 0$; the level structure as a function of u is shown in Figures 5.8 and 5.9, where each state is labeled by the occupancy of the dots as $(n_d - 1, n_q - 1)$.

In the limit of small u the ground state is the usual $(0, 0)$, but as u increases we observe a transition to the ground state $(0, -1)$ for $u = 0.010 D$. The charge excitations between $n_d = 0$ and 1 go from a characteristic energy scale of $0.025 D - u$ which resembles the effect of a gate, to a constant value of $0.015 D$, in excellent agreement with the position of the left Hubbard peak in in Fig. 5.7(a). Meanwhile, the charge excitations between $n_d = 1$ and 2 have an energy of $0.025 D + u$ for $u < 0.005 D$, and $0.035 D - u$ for larger u , also in agreement with the positions of the right Hubbard peak in the figure.

5.4 Quantum charge fluctuations of dot q and their effects on dot d

As we have seen in the previous section, varying the capacitive coupling strength u induces a quantum phase transition (QPT) for dot q — which has a shallower level than dot d —, taking it from a Kondo regime ($u \ll |\varepsilon_q|$, $|\varepsilon_q| \gg \Gamma_q$) into a mixed-valence regime, and finally raising it above the Fermi level. We can also fix the parameter u and study the behavior of the coupled system as a function of the level energy ε_q . An example is shown in Figure 5.10, where we solve the variational equations for the same parameters of Fig. 5.6, but for fixed $u = 1 \times 10^{-4} D$, $1 \times 10^{-3} D$, and $1 \times 10^{-2} D$.

We can see that the curves for Λ_d and Λ_q in Fig. 5.10 coincide for $\varepsilon_q = \varepsilon_d = -0.025 D$, that is, when the subsystems are identical: a good consistency check. As the level in dot q is raised, Λ_q increases by several orders of magnitude, whereas Λ_d decreases dramatically. In order to appreciate what happens when we increase ε_q , consider Eqs. (5.9) and (5.13): For an individual dot, a positive infinitesimal change $\delta\varepsilon$ changes the

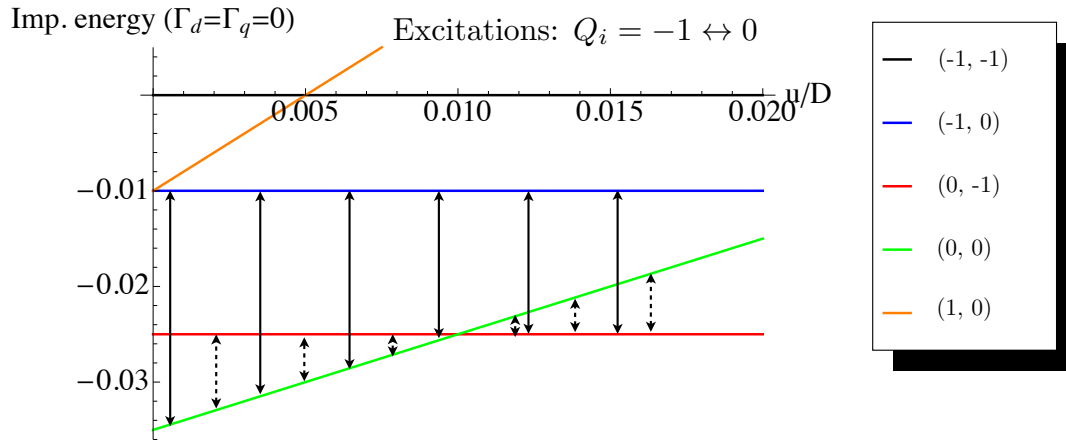


Figure 5.8: Level structure of the double dot system in the FOFP (impurity contribution), for parameters $U_d = U_q = 0.05 D$, $\varepsilon_d = -U_d/2$, $\varepsilon_q = -0.01 D$. Solid (dashed) arrows indicate the low-energy charge excitations of dot d (q) that contribute to the spectral density for $\omega < 0$.

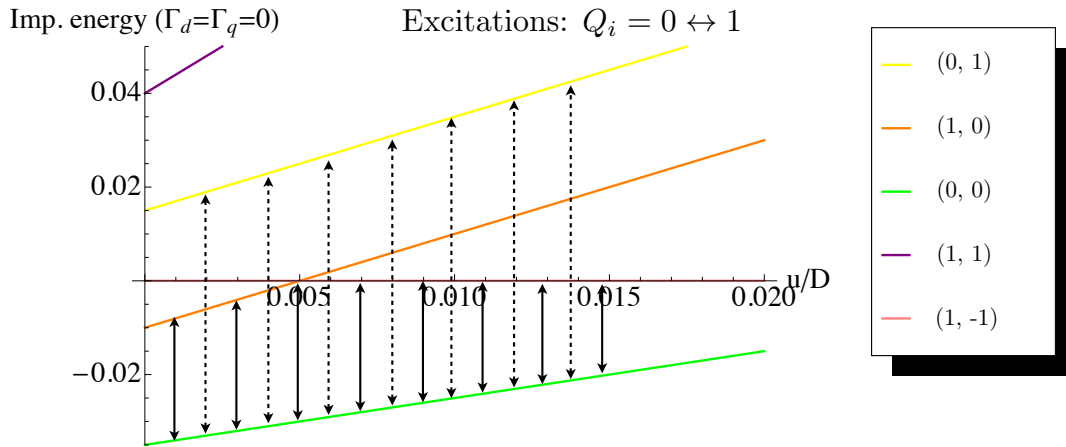


Figure 5.9: Level structure of the double dot system in the FOFP (impurity contribution), for parameters $U_d = U_q = 0.05 D$, $\varepsilon_d = -U_d/2$, $\varepsilon_q = -0.01 D$. Solid (dashed) arrows indicate the low-energy charge excitations of dot d (q) that contribute to the spectral density for $\omega > 0$.

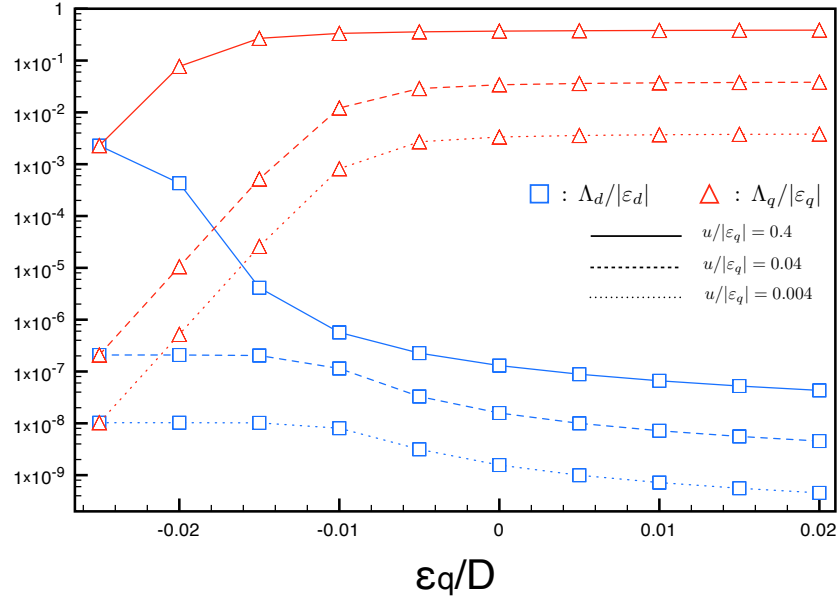


Figure 5.10: Solutions to the variational equations as a function of ε_q , for three different values of u . Blue squares correspond to Λ_d , red triangles to Λ_q , and the type of line indicates the value of u . Parameters: $U_d = U_q = 0.05 D$, $\varepsilon_d = -U_d/2$, $\Gamma_d = \Gamma_q = 0.002 D$ and $u = 1 \times 10^{-4} D$, $1 \times 10^{-3} D$, $1 \times 10^{-2} D$. Parameters given in terms of $|\varepsilon_d| = |\varepsilon_q| = 0.025 D$.

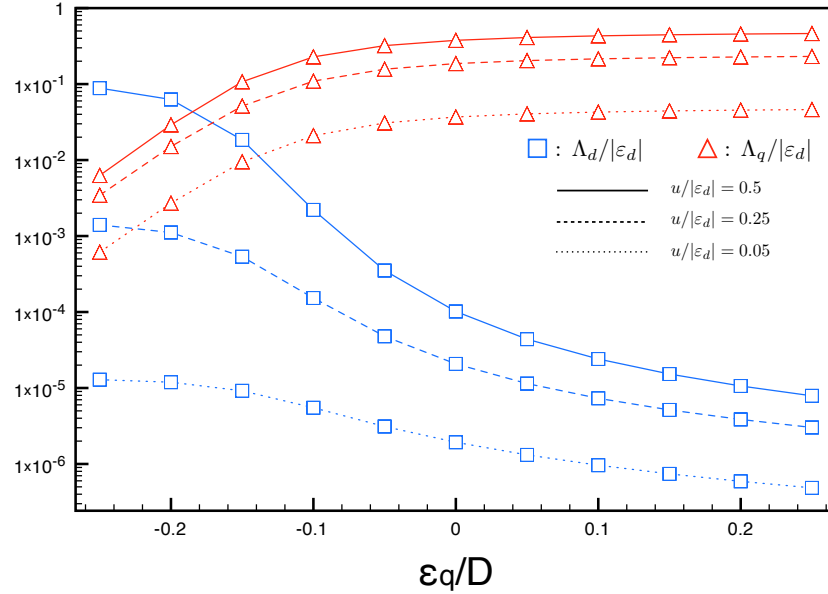


Figure 5.11: Same as Fig. 5.10, but for parameters: $U_d = 0.04 D$, $U_q = 0.50 D$, $\varepsilon_d = -U_d/2$, $\Gamma_d = 0.002 D$, $\Gamma_q = 0.05 D$ and $u = 1 \times 10^{-3} D$, $5 \times 10^{-3} D$, $1 \times 10^{-2} D$.

ground state energy by an amount

$$\delta E(|\varepsilon|) = -\delta\varepsilon \frac{D^2}{V^2} \exp\{-|\varepsilon|D/V^2\}. \quad (5.36)$$

The ground state energy is clearly reduced the most when $|\varepsilon|$ is smaller. When the level shift to one of the dots comes from the capacitive interaction with the other QD ($\delta\varepsilon_i = \Lambda_i$), we can conclude that it is more favorable for the system to have a larger shift in whichever level is closer to the Fermi level, in this case ε_q .

This competition becomes somewhat more interesting in the case shown in Figure 5.11, where the dots are no longer identical. Results in the figure correspond to parameters $\varepsilon_d = -U_d/2 = -0.02 D$, $\Gamma_d = 0.002 D$, $U_q = 0.5 D$, $\Gamma_q = 0.05 D$ ($V_q \approx 0.178 D$), and the Kondo temperatures with $u = 0$ are $T_K^d \approx 1 \times 10^{-6} D$ and $T_K^q \approx 2 \times 10^{-3} D$. Although the starting point is no longer two identical QDs, the argument above is still valid: the trend when moving ε_q closer to the Fermi level is the same, showing a crossing in the level shifts for a u -dependent value of ε_q .

This parameter regime is particularly interesting to us, due to the fact that this difference in energy scales between d and q is typical of a QD and the localized level predicted by Meir, *et al.* in QPCs (see Ref. [74]). The experimental results reported in Ref. [70] show a suppression of up to 25% of the QD conductance for a QPC under a small voltage bias, and gate-tuned to a conductance of approximately $0.7 G_0$, suggesting that (i) the QPC is within the conductance plateau associated with the “0.7” anomaly, and (ii) that in this regime the dephasing rate on the QD due to their coupling reaches a maximum. Reference [13] presents an analysis of the experiment in terms of the model of Ref. [75] to second order in perturbation theory, which shows good qualitative agreement with the data, strongly supporting (i) and (ii).

Our model with the set of parameters of Figure 5.11 becomes relevant to the study of this experimental setup, with q representing the QPC. Figure 5.12 shows NRG results for

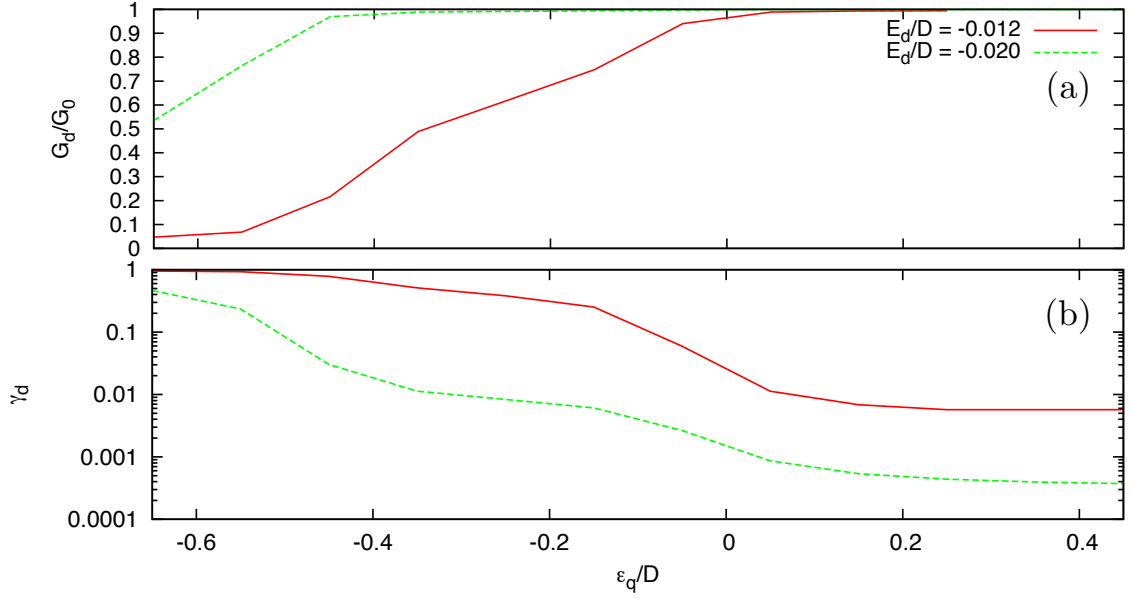


Figure 5.12: (a) Zero-bias conductance of QD d at low temperatures, as a function of the dot q level ε_q . (b) Suppression to the conductance ($\gamma_d := 1 - G_d/G_0$). Parameters: $U_d = 0.04 D$, $\varepsilon_d = -0.020 D$ and $-0.012 D$, $U_q = 0.5 D$, $\Gamma_d = 0.002 D$, $\Gamma_q = 0.05 D$; $u = 0.001 D$, $0.010 D$.

the zero-bias conductance through dot d , as a function of ε_q . The effect of the interaction with dot q for a capacitive coupling $u \sim |\varepsilon_d|$ is very evident through the suppression profile shown in Fig. 5.12(b): when the level of q is above the Fermi level and the charge vanishes, the remote gating is reduced, and d remains in the Kondo regime. As ε_q goes negative and the charge in q increases, the capacitive coupling begins to suppress the conductance of d , reaching a maximum suppression when q is doubly occupied. As shown in Eq. (5.36), a larger remote gating is more economic energetically when the dot level is shallower; the consequence is that the level of dot d experiences a stronger shift in the case of $\varepsilon_d = -0.012 D$, where the suppression is much more significant.

The opposite situation, where the level ε_q is fixed and ε_d is varied, is presented in Figure 5.13, and the same effect is present, although the suppressions are much smaller due to parameters.

The NRG results of Fig. 5.12 are in good qualitative agreement with the predictions of the variational method (Fig. 5.11) within the validity region of the latter— that is, within the Kondo regime—, and remarkably even outside of it, for positive ε_q . The vanishing of Λ_d as ε_q approaches zero from “below” satisfactorily explains the return of d to the usual Kondo regime.

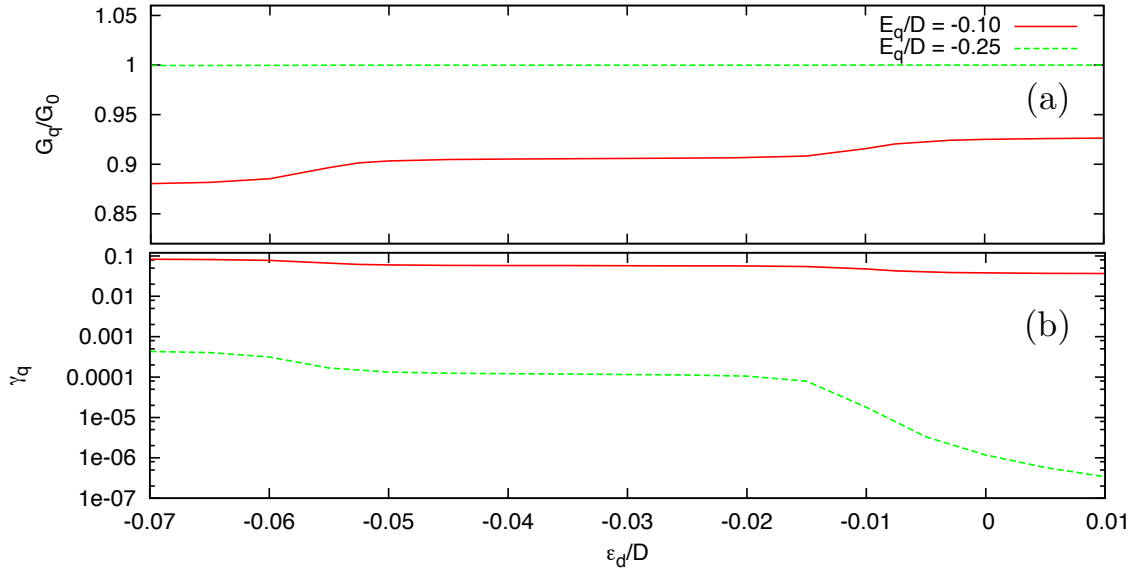


Figure 5.13: (a) Zero-bias conductance of QD q at low temperatures, as a function of the dot d level ε_d . (b) Suppression to the conductance ($\gamma_q := 1 - G_q/G_0$). Parameters: $U_d = 0.04 D$, $U_q = 0.5 D$, $\varepsilon_q = -0.10 D$ and $\varepsilon_q = -0.25 D$, $\Gamma_d = 0.002 D$, $\Gamma_q = 0.05 D$; $u = 0.001 D$, $0.010 D$.

Another interesting experiment consists in exploring the conductance of dot d as a function of ε_d , for ε_q fixed. Dephasing from a QPC charge detector in the “0.7 anomaly” regime has been measured in this manner through its suppression of the unitary conductance of the QD within the Kondo regime (see Figure 3 of Ref. [70]), but an important question to ask is whether decoherence is the only mechanism that can induce this suppression in this capacitively-coupled system.

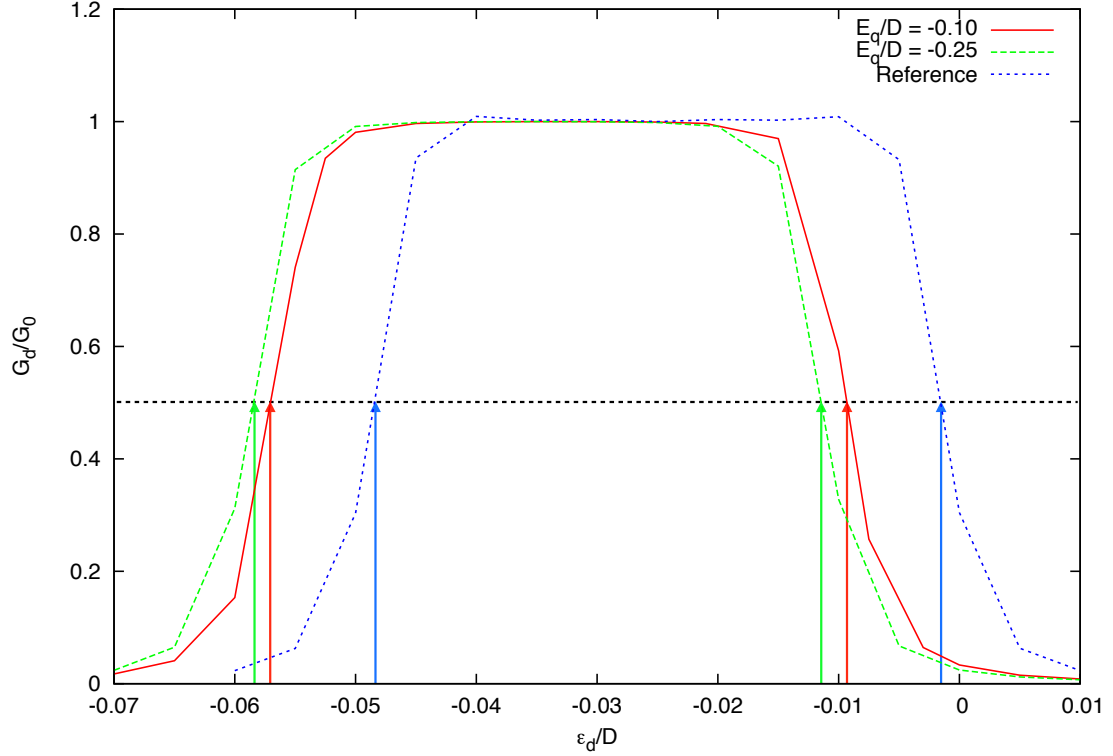


Figure 5.14: Zero-bias conductance of QD d at low temperatures, as a function of the dot level ε_d . The blue curve corresponds to q in the symmetric case $\varepsilon_q = -U_q/d = -0.25 D$, and the red curve to $\varepsilon_q = -0.10 D$. Black dashed curve is a reference, evaluated for $u = 0$. The red curve shows a conductance suppression, and a reduced width of the region of enhanced conductance. Parameters: $U_d = 0.04 D$, $U_q = 0.5 D$, $\Gamma_d = 0.002 D$, $\Gamma_q = 0.05 D$; $u = 0.010 D$.

Results from our NRG calculations are presented in Figure 5.14. The dashed, blue curve serves as a reference: it shows unitary conductance through d , typical of the Kondo effect, when $u = 0$. Conductance is enhanced for $-U_d \lesssim \varepsilon_d \lesssim 0$, when the average occupation of dot d is $\langle n_d \rangle \approx 1$, in agreement with the Friedel sum rule[48]

$$G_d/G_0 = \sum_{\sigma} \sin^2 \{ \pi \langle n_{d\sigma} \rangle \}. \quad (5.37)$$

Switching on the capacitive coupling to $u = 0.01 D \sim |\varepsilon_d|$, we immediately appreciate the external gating from q , as the full curve is displaced to the left. Notice that this displacement for the curve corresponding to $\varepsilon_q = -U_q/2$ (green curve)—when q is deep

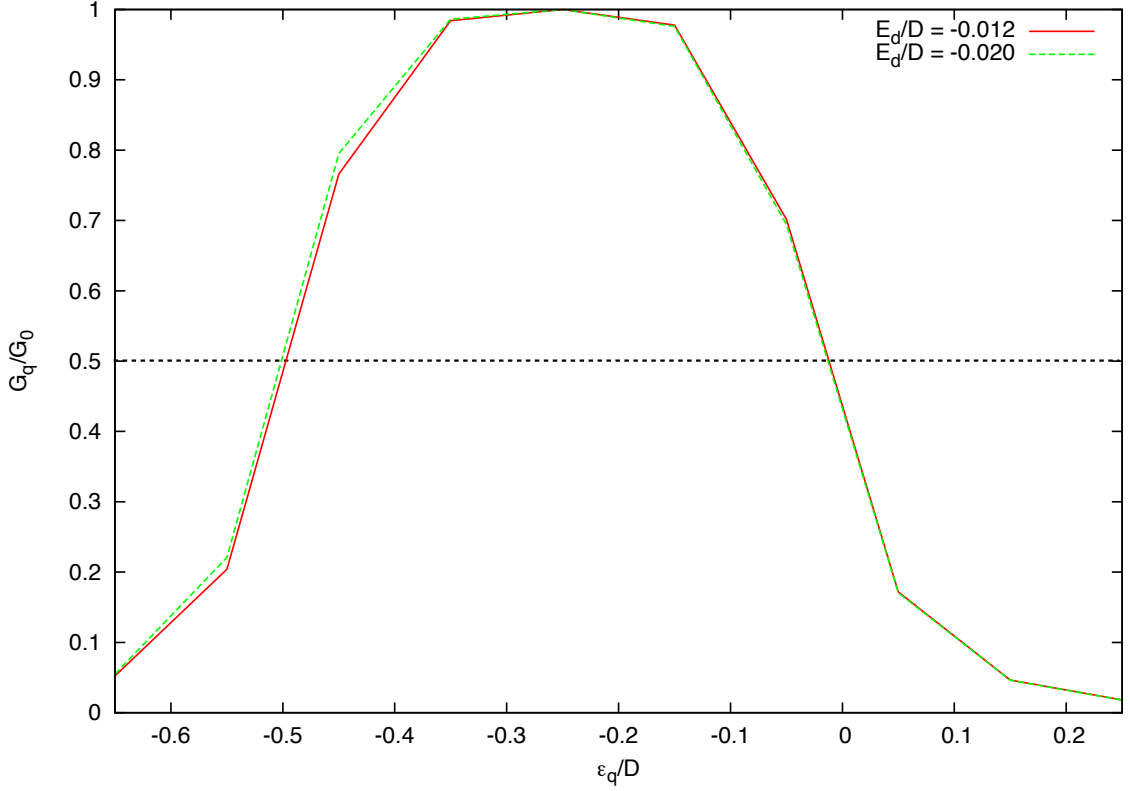


Figure 5.15: Zero-bias conductance of q at low temperatures, as a function of the dot level ε_q , for dot d in the symmetric case (green) and close to mixed-valence, but still in the Kondo regime (red). Parameters: $U_d = 0.04 D$, $\varepsilon_d = -0.020 D$ and $-0.012 D$, $U_q = 0.5 D$, $\Gamma_d = 0.002 D$, $\Gamma_q = 0.05 D$; $u = 0.010 D$.

in the Kondo regime—is in fact u , whereas in the case of $\varepsilon_q = 0.1 D \gtrsim \Gamma_q$ (red curve) the shift is smaller. The explanation is that the shallower level in the latter case is more susceptible to be shifted up by remote gating (Λ_q), thus reducing the gating on dot d (Λ_d).

Almost imperceptible is the fact that the width of the region of enhanced conductance for the red curve is about 2% wider than in the other two curves. We cannot at this point be certain that this widening is not due to precision, and have yet to find a more dramatic example; however, this effect is not entirely surprising because one would expect the inter-dot competition to be more subtle for values of ε_d and ε_q where both levels are near

the edges of the Kondo regime. In this situation, it is possible that the increase of Λ_d that usually lowers the energy be at odds with the increase of Λ_q , which may lower it even more. The shift Λ_d may thus be reduced, and the region widened.

5.5 Conclusions

We studied the effects of a capacitive coupling between two quantum dots within the Kondo regime on their equilibrium transport properties at low temperatures, by means of the numerical renormalization group technique. Through a variational study of the many-body ground state of the pair of quantum dots, we were able to reliably estimate the gating effects produced by the electrostatic repulsion between the quantum dots, as a function of the coupling strength and the individual parameters of the dots.

Our results show that in the case of quantum dots with similar parameters, tuning of the capacitive coupling strength can induce a quantum phase transition out of the Kondo regime in the dot with a shallower level. In the case of a constant coupling strength, we find that the induced gate in the dots may appreciably reduce their zero-bias conductances; we verified this for similar and for different quantum dot parameters, and studied the behavior of the conductances as functions of the dot energy levels.

We believe that this study is relevant for the interpretation of experiments on the dephasing effects of charge detection in quantum dots using nearby quantum point contacts. This dephasing is expected to produce a suppression of the zero bias conductance of the quantum dot, which experiments have shown to be significant, and consistent with the QPC model by Meir, *et al.* By evaluating the full ground state of the system, we are able to predict a conductance suppression not related to dephasing that must be factored into the analysis of the experimental results.

5.6 Future work on capacitively-coupled quantum dots

To further adapt our study to the real QD–QPC system, we will incorporate the charge-dependent hybridization to the QPC impurity model, shown in Ref. [75] to reproduce the “0.7” conductance anomaly. The necessary change to Eq. (5.18a) is

$$H_q \longrightarrow \varepsilon_q n_q + U_q n_{q\downarrow} n_{q\uparrow} + \sum_{\vec{k}\sigma} \left\{ V_q^{01} (1 - n_{d\bar{\sigma}}) d_{\sigma}^{\dagger} c_{\vec{k}\sigma} + V_q^{12} n_{d\bar{\sigma}} d_{\sigma}^{\dagger} c_{\vec{k}\sigma} + \text{H. c.} \right\}, \quad (5.38)$$

where $\bar{\sigma}$ represents the state with opposite spin projection to σ , and the couplings V_q^{01} and V_q^{12} give the hopping amplitude when the dot is empty and singly occupied, respectively. By incorporating this to the single-impurity NRG calculation, we have found a conductance plateau with features similar to the “0.7” anomaly. This result is presented in Figure 5.16. With this modification to the two-impurity NRG code, we will repeat the analysis presented in this chapter for the QD–QPC model. We expect to see a significantly different behavior due to distinct capacitive interactions of the QD with each individual charge state of the QPC.

Other interesting results are expected for a spin-1 QD of the type presented in Chapter 4, where we believe that the capacitive coupling to the QPC can induce a transition in the QD ground state, from an underscreened Kondo state to a regular spin-1/2 Kondo state. This transition may be produced by (i) a different capacitive coupling between the QPC and each of the two molecular levels, and (ii) a difference in the local energies of the molecular levels. Our interest in this problem stems from the fact that it may allow us to explore a quantum phase transition between ground states with qualitatively different low-temperature magnetic properties by means of a simple electrostatic interaction: an attractive possibility by virtue of its intrinsic physical significance, and potential for practical applications.

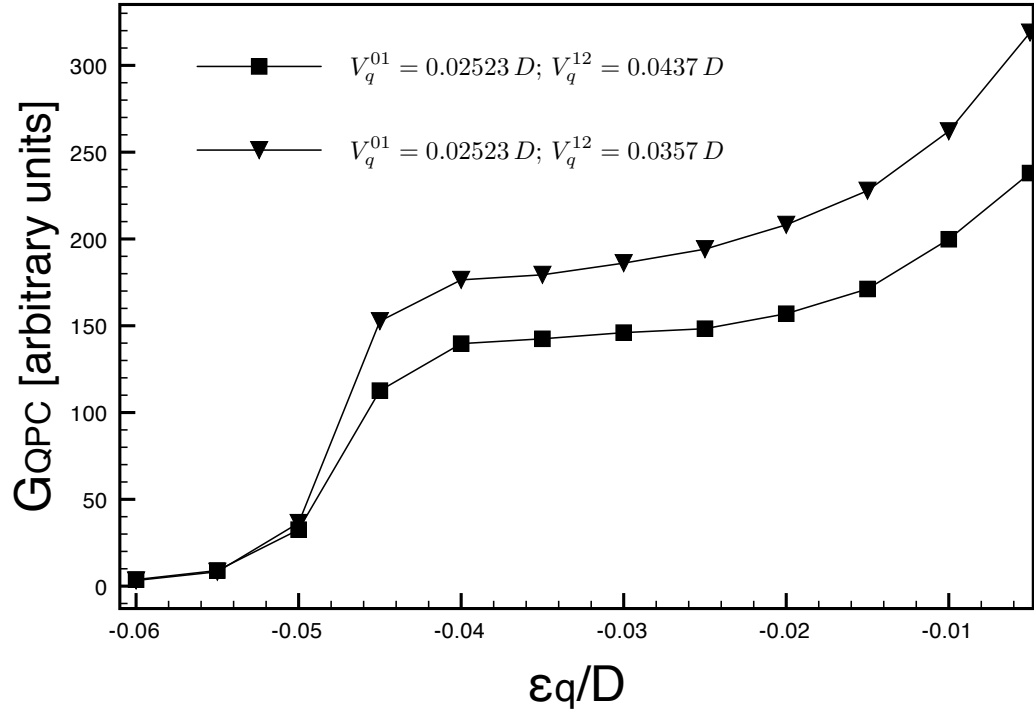


Figure 5.16: Conductance through dot q as a function of the energy level ε_q for $U_q = 0.05 D$. The curves correspond to the charge-dependent couplings to the band $V_q^{01} = 0.0357 D$, $V_q^{12} = 0.02523 D$, and $V_q^{01} = 0.04370 D$, $V_q^{12} = 0.0357 D$, corresponding to hybridizations $\Gamma_q^{01} = 0.002 D$, $\Gamma^{12} = 0.001 D$, and $\Gamma_q^{01} = 0.003 D$, $\Gamma^{12} = 0.001 D$.

6 FINAL REMARKS AND OUTLOOK

The research work presented here is our contribution to the ongoing effort to learn about the unique phenomena that can be found in complex quantum systems. Despite having already been studied for decades, quantum impurity systems are still a subject of great interest today; especially so because we have achieved a deep understanding of their behavior, and they serve now also as a probe for the study of the novel and exotic nanostructured materials and devices discovered in recent years.

There are many possible configurations of quantum impurities yet to be studied, where new and exciting quantum phases may be found. In addition, time dependent phenomena and out-of-equilibrium behavior in quantum impurities are still not well understood, and adequate tools for the calculation of physical properties have yet to be perfected. There is still much work to do, and I believe that the experience gained through the work presented here has served as a solid preparation for it.

In addition to the research plans mentioned in Section 5.6, we will in the near future participate in a research effort to study the transport properties of interacting quantum dots, coupled to Majorana fermions at the end of a Kitaev chain[80]. Majorana fermions are exotic particles with the notorious property of being their own anti-particle; never observed in nature, but predicted to exist in condensed matter systems such as topological insulators, and at the boundary between nano-wires and superconductors, due to the “leak” of the superconducting states into the nano-wire[81, 82]. Our research in that area is aimed at (i) achieving a theoretical understanding of the influence of these exotic particles on the transport properties of quantum impurities, and (ii) on the highly-correlated Kondo ground state, in the interacting case; (iii) we strive to predict conclusive signatures of the existence of Majorana fermions in condensed matter systems that may be recognized in experiments, and (iv) to develop robust calculation tools based

on the NRG and other many-body techniques that allow us to explore increasingly complex systems involving these exotic phases of matter.

Almost 50 years have passed since Jun Kondo's discovery of the mysterious behavior of quantum impurities in metals, and his first glimpse at the rich variety of phenomena that engaged some of the brightest minds of the last century. The insight into the mysterious behavior of many-body systems achieved so far, and the powerful calculation techniques developed through the decades provide us today with the tools for the study of increasingly complex quantum systems, that surprise us with ever more exciting features.

We live in a privileged time where atoms can be seen, pushed around and put together in complex geometries; molecules can be manipulated, their quantum properties explored and even modified at will. We live in a time of hope, when the most exotic states of matter ever imagined— particles that have been predicted but never found in nature— may soon be brought into existence by researchers all over the world, put in contact with probes of all sorts in order to unveil their secrets, and to make them interact with other states of matter in a clever way, in hopes of finding a new mesmerizing phenomenon that will capture our imagination for centuries to come.

BIBLIOGRAPHY

- [1] G. Binnig and H. Rohrer, “Scanning tunneling microscopy,” *IBM Journal of Research and Development*, vol. 30, no. 4, p. 355, 1986.
- [2] C. Bai, *Scanning tunneling microscopy and its applications*. Springer, 1992.
- [3] R. C. Jaeger, *Introduction to microelectronic fabrication*, vol. V of *Modular series on solid state devices*. Prentice Hall, 2nd ed., 1998.
- [4] D. Goldhaber-Gordon, H. Shtrikman, D. Mahalu, D. Abusch-Magder, U. Meirav, and M. A. Kastner, “Kondo effect in a single-electron transistor,” *Nature*, vol. 391, pp. 156–159, Jan 1998.
- [5] W. J. de Haas, J. H. de Boer, and G. J. van d  n Berg, “The electrical resistance of gold, copper and lead at low temperatures,” *Physica*, vol. 1, p. 1115, 1934.
- [6] G. J. Van Den Berg, “Anomalies in dilute metallic solutions of transient elements,” *Prog. in Low Temp. Phys.*, vol. 4, pp. 194–264, 1964.
- [7] N. Roch, S. Florence, V. Bouchiat, W. Wernsdorfer, and F. Balestro, “Quantum phase transition in a single-molecule quantum dot,” *Nature*, vol. 453, pp. 633–637, 2008.
- [8] J. J. Parks, A. R. Champagne, T. A. Costi, W. W. Schum, A. N. Pasupathy, E. Neuscamman, S. Flores-Torres, P. S. Cornaglia, A. A. Aligia, C. A. Balseiro, G. K. L. Chan, H. D. Abru  a, and D. C. Ralph, “Mechanical control of spin states in spin-1 molecules and the underscreened Kondo effect,” *Science*, vol. 328, pp. 1370–1373, 2010.
- [9] V. Iancu, A. Deshpande, and S.-W. Hla, “Manipulating kondo temperature via single molecule switching,” *Nano Lett.*, vol. 6, p. 820, 2006.
- [10] V. Iancu, A. Deshpande, and S.-W. Hla, “Manipulation of the Kondo effect via two-dimensional molecular assembly,” *Phys. Rev. Lett.*, vol. 97, p. 266603, 2006.
- [11] S. Sachdev, *Quantum Phase Transitions*. Cambridge University Press, 2011.
- [12] D. A. Ruiz-Tijerina, P. S. Cornaglia, C. A. Balseiro, and S. E. Ulloa, “Dynamical magnetic anisotropy and quantum phase transitions in a vibrating spin-1 molecular junction,” *Phys. Rev. B*, vol. 86, p. 035437, Jul 2012.
- [13] T. Aono, “Dephasing in a quantum dot coupled to a quantum point contact,” *Phys. Rev. B*, vol. 77, p. 081303(R), 2008.
- [14] P. Drude, “On the electronic theory of metals (zur Elektronentheorie der Metalle),” *Ann. Phys.*, vol. 306, no. 3, pp. 566–613, 1900.

- [15] P. Drude, “On the electronic theory of metals; II. galvanomagnetic and thermomagnetic effects (zur Elektronentheorie der Metalle; II. teil. galvanomagnetische und thermomagnetische Effecte,” *Ann. Phys.*, vol. 308, no. 11, pp. 369–402, 1900.
- [16] W. J. De Haas and J. De Boer, “The electrical resistance of platinum at low temperatures,” *Physica*, vol. 1, pp. 609–616, 1934.
- [17] W. J. De Haas and J. De Boer, “The electrical resistance of gold, copper and lead at low temperatures,” *Physica*, vol. 1, pp. 1115–1124, 1934.
- [18] J. Kondo, “Resistance minimum in dilute magnetic alloys,” *Prog. Theor. Phys.*, vol. 32, p. 37, 1964.
- [19] C. Zener, “Interactions between the d shells in the transition metals,” *Phys. Rev.*, vol. 87, p. 440, 1951.
- [20] T. Kasuya, “A theory of metallic ferro- and anti ferromagnetism on Zewer’s model,” *Prog. Theor. Phys.*, vol. 16, p. 45, 1956.
- [21] K. Yosida, “Magnetic properties of Cu-Mn alloys,” *Phys. Rev.*, vol. 106, p. 893, 1957.
- [22] K. Yosida, “Anomalous electrical resistivity and magnetoresistance due to an $s - d$ interaction in Cu-Mn alloys,” *Phys. Rev.*, vol. 107, p. 396, 1957.
- [23] P. Phillips, *Advanced solid state physics*. Perseus Books, 2008.
- [24] K. G. Wilson, “The renormalization group: critical phenomena and the Kondo problem,” *Rev. Mod. Phys.*, vol. 47, pp. 773–840, Oct 1975.
- [25] P. B. Wiegmann, “Exact solution of the s - d exchange model at $t=0$ (Точное решение s - d обменной модели при $t=0$.),” *JETP Lett.*, vol. 7, no. 31, pp. 364–370, 1980.
- [26] N. Andrei, “Diagonalization of the Kondo Hamiltonian,” *Phys. Rev. Lett.*, vol. 45, p. 379, 1980.
- [27] A. A. Abrikosov, “Electron scattering on magnetic impurities in metals and anomalous resistivity effects (О рассеянии электронов металле на магнитных примесных атомах и особенности поведения сопротивления),” *Fizika*, vol. 2, no. 1, pp. 21–37, 1965.
- [28] J. R. Schrieffer and P. A. Wolff, “Relation between the Anderson and Kondo hamiltonians,” *Phys. Rev.*, vol. 149, pp. 491–492, 1966.
- [29] S. M. Cronenwett, T. H. Oosterkamp, and L. P. Kouwenhoven, “A tunable Kondo effect in quantum dots,” *Science*, vol. 281, pp. 540–544, 1998.

- [30] I. Herbut, *A modern approach to critical phenomena*. Cambridge University Press, 2007.
- [31] L. P. Kadanoff, “Scaling laws for Ising models near t_c ,” *Physics*, vol. 2, no. 6, 1966.
- [32] L. D. Landau and E. M. Lifshitz, *Course of theoretical physics vol.5: Statistical physics I*. Nauka Moscow, 1976.
- [33] M. Kardar, *Statistical physics of fields*. Cambridge University Press, 2007.
- [34] M. Plischke and B. Bergersen, *Equilibrium statistical physics*. World Scientific, 2006.
- [35] P. W. Anderson, “A poor man’s derivation of scaling laws for the Kondo problem,” *J. Phys. C: Solid State*, vol. 3, p. 2436, 1970.
- [36] A. Altland and B. Simmons, *Condensed matter field theory*. Cambridge University Press, 2006.
- [37] M. Srednicki, *Quantum field theory*. Cambridge University Press, 2007.
- [38] H. R. Krishna-murthy, J. W. Wilkins, and K. G. Wilson, “Renormalization-group approach to the Anderson model of dilute magnetic alloys I. Static properties for the symmetric case,” *Phys. Rev. B*, vol. 21, p. 1003, 1980.
- [39] H. R. Krishna-murthy, J. W. Wilkins, and K. G. Wilson, “Renormalization-group approach to the Anderson model of dilute magnetic alloys II. Static properties for the asymmetric case,” *Phys. Rev. B*, vol. 21, p. 1044, 1980.
- [40] R. Bulla, T. A. Costi, and T. Pruschke, “Numerical renormalization group method for quantum impurity systems,” *Rev. Mod. Phys.*, vol. 80, pp. 395–450, 2008.
- [41] R. Bulla, T. A. Costi, and D. Vollhardt, “Finite-temperature numerical renormalization group study of the Mott transition,” *Phys. Rev. B*, vol. 64, p. 045103, 2001.
- [42] R. Bulla, T. Pruschke, and A. C. Hewson, “Anderson impurity in pseudo-gap Fermi systems,” *J. Phys.: Condens. Matter*, vol. 9, pp. 10463–10474, 1997.
- [43] W. C. Oliveira and L. N. Oliveira, “Generalized numerical renormalization-group method to calculate the thermodynamical properties of impurities in metals,” *Phys. Rev. B*, vol. 49, p. 986, 1994.
- [44] V. L. Campo and L. N. Oliveira, “Alternative discretization in the numerical renormalization-group method,” *Phys. Rev. B*, vol. 72, p. 104432, 2005.
- [45] K. Chen and C. Jayaprakash *Phys. Rev. B*, vol. 21, p. 1003, 1980.

- [46] E. N. Economou, *Green's functions in quantum physics*. Springer, 2006.
- [47] A. A. Abrikosov, L. P. Gorkov, and I. E. Dzyaloshinski, *Methods of quantum field theory in statistical physics* (Методы квантовой теории поля в статистической физике). М.: Fizmatgiz, 1962.
- [48] A. C. Hewson, *The Kondo problem to heavy fermions*. Cambridge University Press, 1993.
- [49] R. Žitko, R. Peters, and T. Pruschke, “Properties of anisotropic magnetic impurities on surfaces,” *Phys. Rev. B*, vol. 78, p. 224404, 2008.
- [50] T. E. Walker and W. G. Richards, “Calculation of spin–orbit coupling constants in diatomic molecules from Hartree–Fock wave functions,” *Phys. Rev.*, vol. 177, p. 100, 1969.
- [51] C. A. Masmanidis, H. H. Jaffe, and R. L. Ellis, “Spin–orbit coupling in organic molecules,” *J. Phys. Chem.*, vol. 79, pp. 2052–2061, 1975.
- [52] L. Arrachea, A. A. Aligia, and G. E. Santoro, “Microscopic theory of vibronic dynamics in linear polyenes,” *Phys. Rev. B*, vol. 67, p. 134307, 2003.
- [53] A. A. Aligia and T. Kroll, “Effective Hamiltonian for transition-metal compounds: Application to $na_x\text{CoO}_2$,” *Phys. Rev. B*, vol. 81, p. 195113, 2010.
- [54] E. Minamitani, N. Tsukahara, D. Matsukana, Y. Kim, N. Takagi, and M. Kawai, “Symmetry–driven novel Kondo effect in a molecule,” *Phys. Rev. Lett.*, vol. 109, p. 086602, 2012.
- [55] P. S. Cornaglia, P. Roura-Bas, A. A. Aligia, and C. A. Balseiro, “Quantum transport through a stretched spin-1 molecule,” *Europhys. Lett.*, vol. 93, p. 47005, 2011.
- [56] F. Mallet, J. Ericsson, D. Mailly, S. Üllübayır, D. Reuter, A. Melnikov, A. D. Wieck, T. Micklitz, A. Rosch, T. A. Costi, L. Saminadayar, and C. Bäuerle, “Scaling of the low–temperature dephasing rate in Kondo systems,” *Phys. Rev. Lett.*, vol. 97, p. 226804, 2006.
- [57] M. Presselt, B. Dietzek, M. Schmitt, J. Popp, A. Winter, M. Chiper, C. Friebe, and U. S. Schubert, “Zinc(II) bisterpyridine complexes: the influence of the cation on the π -conjugation between terpyridine and the lateral phenyl substituent,” *J. Phys. Chem. C*, vol. 112, pp. 18651–18660, 2008.
- [58] J. J. Sakurai, *Modern Quantum Mechanics*. Addison–Wesley Publishing Company, 1994.
- [59] A.-P. Jauho, N. S. Wingreen, and Y. Meir, “Time–dependent transport in interacting and noninteracting resonant–tunneling systems,” *Phys. Rev. B*, vol. 50, p. 5528, 1994.

- [60] H. Pastawski, “Classical and quantum transport from generalized Landauer-Büttiker equations. II. Time-dependent resonant tunneling,” *Phys. Rev. B*, vol. 46, p. 4053, 1992.
- [61] A. C. Hewson and D. Meyer, “Numerical renormalization group study of the Anderson–Holstein impurity model,” *J. Phys.: Condens. Matter*, vol. 14, pp. 427–445, 2002.
- [62] J. González, M. A. Martín-Delgado, G. Sierra, and A. H. Vozmediano, *Quantum electron liquids and High- T_c superconductivity*, vol. 38 of *Lecture notes in physics: N.s. M. Monographs*. Springer, 1995.
- [63] M. I. Kastnelson, *Graphene: carbon in two dimensions*. Cambridge University Press, 2012.
- [64] P. Mehta, N. Andrei, P. Coleman, L. Borda, and G. Zarand, “Regular and singular Fermi-liquid fixed points in quantum impurity models,” *Phys. Rev. B*, vol. 72, p. 014430, 2005.
- [65] E. Buks, R. Schuster, M. Heiblum, D. Mahalu, and V. Umansky, “Dephasing in electron interference by a “which-path” detector,” *Nature*, vol. 391, p. 871, February 1998.
- [66] I. L. Aleiner, N. S. Wingreen, and Y. Meir, “Dephasing and the orthogonality catastrophe in tunneling through a quantum dot: the “which path?” interferometer,” *Phys. Rev. Lett.*, vol. 79, no. 19, pp. 3740–3743, 1997.
- [67] A. Silva and S. Levitt, “Peculiarities of the controlled dephasing of a quantum dot in the kondo regime,” *Europhys. Lett.*, vol. 62, pp. 103–109, April 2003.
- [68] K. Kang, “Decoherence of the kondo singlet via a quantum point contact detector,” *Phys. Rev. Lett.*, vol. 95, p. 206808, 2005.
- [69] A. Stern, Y. Aharonov, and Y. Imry, “Phase uncertainty and loss of interference: a general picture,” *Phys. Rev. A*, vol. 41, pp. 3436–3448, 1990.
- [70] M. Avinun-Kalish, M. Heiblum, A. Silva, D. Mahalu, and V. Umansky, “Controlled dephasing of a quantum dot in the kondo regime,” *Phys. Rev. Lett.*, vol. 92, no. 15, p. 156801, 2004.
- [71] K. J. Thomas, J. T. Nicholls, N. J. Appleyard, M. Y. Simmons, M. Pepper, D. R. Mace, W. R. Tribe, and D. A. Ritchie, “Interaction effects in a one-dimensional constriction,” *Phys. Rev. B*, vol. 58, no. 8, p. 4846, 1998.
- [72] F. Bauer, J. Heyder, E. Schubert, E. Borowsky, D. Taubert, B. Brugnolo, D. Schuh, W. Wegscheider, J. von Delft, and S. Ludwig, “Microscopic origin of the “0.7-anomaly” in quantum point contacts,” *Nature*, vol. 501, pp. 73–78, 2013.

- [73] T. Rejec and Y. Meir, “Magnetic impurity formation in quantum point contacts,” *Nature*, vol. 442, August 2006.
- [74] Y. Meir, “The theory of the “0.7 anomaly” in quantum point contacts,” *J. Phys.: Condens. Matt.*, vol. 20, p. 164208, 2008.
- [75] Y. Meir, K. Hirose, and N. S. Wingreen, “Kondo model for the “0.7 anomaly” in transport through a quantum point contact,” *Phys. Rev. Lett.*, vol. 89, no. 19, p. 196802, 2002.
- [76] C. M. Varma and Y. Yafet, “Magnetic susceptibility of mixed–valence rare–earth compounds,” *Phys. Rev. B*, vol. 13, no. 7, pp. 2950–2954, 1976.
- [77] M. R. Galpin, D. E. Logan, and H. R. Krishna-murthy, “Renormalization group study of capacitively coupled double quantum dots,” *J. Phys.: Condens. Matt.*, vol. 18, p. 6545, 2005.
- [78] M. R. Galpin, D. E. Logan, and H. R. Krishna-murthy, “Dynamics of capacitively coupled double quantum dots,” *J. Phys.: Condens. Matt.*, vol. 18, p. 6571, 2005.
- [79] M. R. Galpin, D. E. Logan, and H. R. Krishna-murthy, “Quantum phase transitions in capacitively coupled double quantum dots,” *Phys. Rev. Lett.*, vol. 94, p. 186406, 2005.
- [80] Y. A. Kitaev, “Unpaired Majorana fermions in quantum wires,” *Phys.-Usp.*, vol. 44, p. 131, 2001.
- [81] Y. Oreg, G. Refael, and F. von Oppen, “Helical liquids and Majorana bound states in quantum wires,” *Phys. Rev. Lett.*, vol. 105, p. 177002, 2010.
- [82] R. M. Lutchyn, J. D. Sau, and S. Das Sarma, “Majorana fermions and topological phase transition in semiconductor–superconductor heterostructures,” *Phys. Rev. Lett.*, vol. 105, p. 077001, 2010.

APPENDIX A: DETAILED CALCULATIONS ON THE DYNAMICAL ANISOTROPY OF SPIN-1 MOLECULAR SYSTEMS.

A.1 Applying the translation operator to the hybridization term

The translation operator is given by

$$T = \exp \left\{ \frac{A_1}{\omega_0} S_z^2 (a^\dagger - a) \right\}, \quad (\text{A.1})$$

and the transformed hybridization term is given by

$$\tilde{H}_{\text{M-E}} = T^\dagger H_{\text{M-E}} T = \sqrt{2} V \sum_{\vec{k}, \sigma} \left(T^\dagger d_{a\sigma}^\dagger T c_{\vec{k}\sigma} + c_{\vec{k}\sigma}^\dagger T^\dagger d_{a\sigma} T \right), \quad (\text{A.2})$$

where we have made use of the fact that the operators T and T^\dagger have no effect on the band degrees of freedom. To calculate $T^\dagger d_{a\sigma}^\dagger T$ and $T^\dagger d_{a\sigma} T$ we make use of the following commutation relations (see Appendix A.4):

- $[n_{i\alpha}, d_{a\sigma}] = -d_{i\alpha} \delta_{i,a} \delta_{\alpha,\sigma},$
- $[n_{i\alpha}, d_{a\sigma}^\dagger] = d_{i\alpha}^\dagger \delta_{i,a} \delta_{\alpha,\sigma},$
- $[n_{i\alpha} n_{j\beta}, d_{a\sigma}] = -n_{i\alpha} d_{j\beta} \delta_{j,a} \delta_{\beta,\sigma} - d_{i\alpha} \delta_{i,a} \delta_{\alpha,\sigma} n_{j\beta},$
- $[n_{i\alpha} n_{j\beta}, d_{a\sigma}^\dagger] = n_{i\alpha} d_{j\beta}^\dagger \delta_{j,a} \delta_{\beta,\sigma} + d_{i\alpha}^\dagger \delta_{i,a} \delta_{\alpha,\sigma} n_{j\beta},$

With this we obtain the following commutators:

$$[S_z^2, d_{a\sigma}^\dagger] = \frac{1}{4} d_{a\sigma}^\dagger [1 - 2n_{a\bar{\sigma}} + 4\sigma S_z^b], \quad (\text{A.3})$$

$$[S_z^2, d_{a\sigma}] = -\frac{1}{4} d_{a\sigma} [1 - 2n_{a\bar{\sigma}} + 4\sigma S_z^b]. \quad (\text{A.4})$$

Using Equations (A.23) and (A.24) we find that

$$T^\dagger d_{a\sigma}^\dagger T = d_{a\sigma}^\dagger \exp \left\{ -\frac{A_1}{4\omega_0} (a^\dagger - a) [1 - 2n_{a\bar{\sigma}} + 4\sigma S_z^b] \right\}, \quad (\text{A.5})$$

$$T^\dagger d_{a\sigma} T = d_{a\sigma} \exp \left\{ \frac{A_1}{4\omega_0} (a^\dagger - a) [1 - 2n_{a\bar{\sigma}} + 4\sigma S_z^b] \right\}. \quad (\text{A.6})$$

The full transformed hybridization term Eq. (4.27) can be written as

$$\tilde{H}_{\text{M-E}} = \sum_{\vec{k}\sigma} \left(\tilde{V}_\sigma^\dagger d_{a\sigma}^\dagger c_{\vec{k}\sigma}^\dagger + \tilde{V}_\sigma c_{\vec{k}\sigma}^\dagger d_{a\sigma} \right), \quad (\text{A.7})$$

with

$$\tilde{V}_\sigma(n_{a\bar{\sigma}}, S_z^b) \equiv \sqrt{2} V e^{\frac{A_1}{4\omega_0} (a - a^\dagger) [1 - 2n_{a\bar{\sigma}} + 4\sigma S_z^b]}. \quad (\text{A.8})$$

A.2 An estimation of the anisotropic hybridization due to the spin–vibron interaction

In this calculation, the spin–1 molecule’s ground state is the full degenerate triplet. That is, the effective anisotropy is $\tilde{A} = 0$. The molecule is then coupled to the metallic band of the leads by the hybridization term Eq. (4.28).

This term is complicated, but it is possible to evaluate the relevant fluctuations at zero temperature by computing the probability amplitudes of transitions among the hybridizing states. Let us define the uncoupled band state as

$$|\Omega\rangle := \prod_{k < k_F} c_{k\uparrow}^\dagger c_{k\downarrow}^\dagger |0\rangle, \quad (\text{A.9})$$

with k_F the Fermi momentum and $|0\rangle$ the vacuum state. The possible transitions are then:

$$\begin{aligned} |T, +1\rangle |\Omega\rangle &\longleftrightarrow |0_a \uparrow_b\rangle |\uparrow\rangle; \\ |T, +1\rangle |\downarrow\rangle &\longleftrightarrow |\uparrow\downarrow_a \uparrow_b\rangle |\Omega\rangle; \\ |T, -1\rangle |\uparrow\rangle &\longleftrightarrow |\uparrow\downarrow_a \downarrow_b\rangle |\Omega\rangle; \\ |T, -1\rangle |\Omega\rangle &\longleftrightarrow |0_a \downarrow_b\rangle |\downarrow\rangle; \\ |T, 0\rangle |\Omega\rangle &\longleftrightarrow \frac{1}{\sqrt{2}} |0_a \downarrow_b\rangle |\uparrow\rangle, \frac{1}{\sqrt{2}} |0_a \uparrow_b\rangle |\downarrow\rangle; \\ |T, 0\rangle |\uparrow\rangle &\longleftrightarrow \frac{1}{\sqrt{2}} |\uparrow\downarrow_a \uparrow_b\rangle |\Omega\rangle; \\ |T, 0\rangle |\downarrow\rangle &\longleftrightarrow \frac{1}{\sqrt{2}} |\uparrow\downarrow_a \downarrow_b\rangle |\Omega\rangle. \end{aligned}$$

To evaluate the matrix elements of the Hamiltonian over these states, it is important to define an ordering convention for the states, and stick to it throughout the calculation, due to the Fermionic signs that will arise when we reorder the operators. The convention followed here is as follows: all operators of the level a are placed to the left of those of level b , and all operators involving $\sigma = \uparrow$ are to the left of those involving $\sigma = \downarrow$; *e.g.*

$$|\uparrow_a \uparrow_b\rangle = d_{a\uparrow}^\dagger d_{b\uparrow}^\dagger d_{b\downarrow}^\dagger |0\rangle.$$

The band operators are placed to the right of all molecular operators, with the same spin ordering and with the lower momentum states farther to the right, as shown in Eq. (A.9).

Now that this is clear, the matrix elements are given by

$$\langle 0_a \uparrow_b | \langle \uparrow | \tilde{V}_\uparrow c_\uparrow^\dagger d_{a\uparrow} | \Omega \rangle | T, +1 \rangle = \langle \uparrow \downarrow_a \uparrow_b | \langle \Omega | \tilde{V}_\downarrow^\dagger d_{a\downarrow}^\dagger c_\downarrow | \downarrow \rangle | T, +1 \rangle = \sqrt{2} V e^{\frac{3A_1}{4\omega_0}(a^\dagger - a)}, \quad (\text{A.10a})$$

$$\langle 0_a \downarrow_b | \langle \downarrow | \tilde{V}_\downarrow c_\downarrow^\dagger d_{a\downarrow} | \Omega \rangle | T, -1 \rangle = \langle \uparrow \downarrow_a \downarrow_b | \langle \Omega | \tilde{V}_\uparrow^\dagger d_{a\uparrow}^\dagger c_\uparrow | \uparrow \rangle | T, -1 \rangle = \sqrt{2} V e^{\frac{3A_1}{4\omega_0}(a^\dagger - a)}, \quad (\text{A.10b})$$

$$\langle 0_a \uparrow_b | \langle \downarrow | \tilde{V}_\downarrow c_\downarrow^\dagger d_{a\downarrow} | \Omega \rangle | T, 0 \rangle = \langle \uparrow \downarrow_a \uparrow_b | \langle \Omega | \tilde{V}_\uparrow^\dagger d_{a\uparrow}^\dagger c_\uparrow | \uparrow \rangle | T, 0 \rangle = -V e^{-\frac{A_1}{4\omega_0}(a^\dagger - a)}, \quad (\text{A.10c})$$

$$\langle 0_a \downarrow_b | \langle \uparrow | \tilde{V}_\uparrow c_\uparrow^\dagger d_{a\uparrow} | \Omega \rangle | T, 0 \rangle = \langle \uparrow \downarrow_a \downarrow_b | \langle \Omega | \tilde{V}_\downarrow^\dagger d_{a\downarrow}^\dagger c_\downarrow | \downarrow \rangle | T, 0 \rangle = -V e^{-\frac{A_1}{4\omega_0}(a^\dagger - a)}. \quad (\text{A.10d})$$

The particle–hole and spin symmetries are clear, and we can also see that the fluctuations from and to the state $|T, 0\rangle$ contribute differently from those involving the states $|T, \pm 1\rangle$. This becomes more obvious when we average over arbitrary phonon occupation states by means of the formula

$$(m | e^{\alpha(a^\dagger - a)} | n) \sim e^{-\frac{\alpha^2}{2}} (m | e^{\alpha a^\dagger} e^{-\alpha a} | n). \quad (\text{A.11})$$

where $\alpha \in \mathbb{C}$. This means that the hybridization of the metallic states with the state $|T, 0\rangle$ is exponentially smaller than that with the states $|T, \pm 1\rangle$ by effect of the spin–vibron molecule, by a factor of the order of $\exp\{(A_1/\omega_0)^2\}$.

In Section A.3 it will be shown that this anisotropic hybridization places the level $|T, 0\rangle$ at lower energy with respect to the rest of the triplet, thus producing a positive contribution to the net anisotropy of the system.

A.3 Calculating the matrix elements of the hybridization term, relevant to the Schrieffer–Wolff transformation of Section

Equations (4.36) and (4.37), respectively give the general form of the diagonal and non–diagonal corrections of the hybridization to the decoupled Hamiltonian $H_0 + H_E$, up to second order in the coupling V .

This section contains the evaluated matrix elements relevant to the calculation of these corrections. We make extensive use of the canonical fermionic anti–commutation relations

$$\{\xi_i, \xi_j\} = \{\xi_i^\dagger, \xi_j^\dagger\} = 0, \quad \{\xi_i, \xi_j^\dagger\} = \delta_{i,j}, \quad (\text{A.12})$$

where $\xi_i \in \{d_{a\sigma}, d_{b\sigma}, c_{k\sigma}\}$.

A.3.1 States involving the molecular state $|T, +1; \tilde{n}\rangle$

The state $|c\rangle |T, +1; \tilde{n}\rangle$, with c the band state, is coupled by means of H_{M-E} to the following states:

$$\text{i) } c = \Omega : |\uparrow\rangle |0_a \uparrow_b\rangle |m\rangle$$

$$\text{ii) } c = \downarrow : |\uparrow\downarrow\rangle |0_a \uparrow_b\rangle |m\rangle$$

$$\text{iii) } c = \downarrow : |\Omega\rangle |\uparrow\downarrow_a \uparrow_b\rangle |m\rangle$$

$$\text{iv) } c = \uparrow\downarrow : |\uparrow\rangle |\uparrow\downarrow_a \uparrow_b\rangle |m\rangle$$

The matrix elements are given in Table A.3.1. The states involving the triplet are abbreviated using the labels from Table 4.2.

Matrix element	Value
$\langle 1, n H_{\text{M-E}} i \rangle$	$\sqrt{2} V (\tilde{n} m)$
$\langle 2, n H_{\text{M-E}} ii \rangle$	$-\sqrt{2} V (\tilde{n} m)$
$\langle 2, n H_{\text{M-E}} iii \rangle$	$-\sqrt{2} V (\tilde{n} m)$
$\langle 3, n H_{\text{M-E}} iv \rangle$	$-\sqrt{2} V (\tilde{n} m)$

Table A.1: Matrix elements involving the molecular state $|T, +1; \tilde{n}\rangle$.

Diagonal corrections given by Eq. (4.36) are also shown:

- $\langle 1, n | \frac{i}{2} [s, H_{\text{M-E}}] | 1, n \rangle :$

$$\begin{aligned}
 \langle 1, n | \frac{i}{2} [s, H_{\text{M-E}}] | 1, n \rangle &= \sum_{m=0}^{\infty} \frac{|\langle 1, n | H_{\text{M-E}} | i \rangle|^2}{2\varepsilon - \frac{J}{4} + (n-m)\omega_0} \\
 &= \sum_{m=0}^{\infty} \frac{2V^2 |(\tilde{n} | m)|^2}{-\frac{U}{2} - \frac{J}{4} + (n-m)\omega_0}
 \end{aligned} \tag{A.13}$$

- $\langle 2, n | \frac{i}{2} [s, H_{\text{M-E}}] | 2, n \rangle :$

$$\begin{aligned}
 \langle 2, n | \frac{i}{2} [s, H_{\text{M-E}}] | 2, n \rangle &= \sum_{m=0}^{\infty} \left[\frac{|\langle 2, n | H_{\text{M-E}} | ii \rangle|^2}{\varepsilon - \frac{J}{4} + (n-m)\omega_0} \right. \\
 &\quad \left. + \frac{|\langle 2, n | H_{\text{M-E}} | iii \rangle|^2}{\varepsilon - \frac{J}{4} + (n-m)\omega_0} \right] \\
 &= \sum_{m=0}^{\infty} \frac{4V^2 |(\tilde{n} | m)|^2}{-\frac{U}{2} - \frac{J}{4} + (n-m)\omega_0}
 \end{aligned} \tag{A.14}$$

- $\langle 3, n | \frac{i}{2} [s, H_{\text{M-E}}] | 3, n \rangle :$

$$\begin{aligned}
 \langle 3, n | \frac{i}{2} [s, H_{\text{M-E}}] | 3, n \rangle &= \sum_{m=0}^{\infty} \frac{|\langle 3, n | H_{\text{M-E}} | iv \rangle|^2}{-\varepsilon - U - \frac{J}{4} + (n-m)\omega_0} \\
 &= \sum_{m=0}^{\infty} \frac{2V^2 |(\tilde{n} | m)|^2}{-\frac{U}{2} - \frac{J}{4} + (n-m)\omega_0}
 \end{aligned} \tag{A.15}$$

A.3.2 States involving the molecular state $|T, -1; \tilde{n}\rangle$

The state $|c\rangle |T, -1; \tilde{n}\rangle$, with c the band state, is coupled by means of H_{M-E} to the following states:

i) $c = \Omega : |\downarrow\rangle |0_a \downarrow_b\rangle |m\rangle$

ii) $c = \uparrow : |\uparrow\downarrow\rangle |0_a \downarrow_b\rangle |m\rangle$

iii) $c = \uparrow : |\Omega\rangle |\uparrow\downarrow_a \downarrow_b\rangle |m\rangle$

iv) $c = \uparrow\downarrow : |\downarrow\rangle |\uparrow\downarrow_a \downarrow_b\rangle |m\rangle$

The matrix elements are given in Table A.3.2. The states involving the triplet are abbreviated using the labels from Table 4.2.

Matrix element	Value
$\langle 4, n H_{M-E} i \rangle$	$\sqrt{2} V (\tilde{n} m)$
$\langle 5, n H_{M-E} ii \rangle$	$\sqrt{2} V (\tilde{n} m)$
$\langle 5, n H_{M-E} iii \rangle$	$\sqrt{2} V (\tilde{n} m)$
$\langle 6, n H_{M-E} iv \rangle$	$-\sqrt{2} V (\tilde{n} m)$

Table A.2: Matrix elements involving the molecular state $|T, -1; \tilde{n}\rangle$.

Diagonal corrections given by Eq. (4.36) are also shown:

- $\langle 4, n | \frac{i}{2} [s, H_{M-E}] | 4, n \rangle :$

$$\begin{aligned}
 \langle 4, n | \frac{i}{2} [s, H_{M-E}] | 4, n \rangle &= \sum_{m=0}^{\infty} \frac{|\langle 4, n | H_{M-E} | i \rangle|^2}{2\varepsilon - \frac{J}{4} + (n-m)\omega_0} \\
 &= \sum_{m=0}^{\infty} \frac{2V^2 |\langle \tilde{n} | m \rangle|^2}{-\frac{U}{2} - \frac{J}{4} + (n-m)\omega_0}
 \end{aligned} \tag{A.16}$$

- $\langle 5, n | \frac{i}{2} [s, H_{\text{M-E}}] | 5, n \rangle :$

$$\begin{aligned} \langle 5, n | \frac{i}{2} [s, H_{\text{M-E}}] | 5, n \rangle &= \sum_{m=0}^{\infty} \left[\frac{|\langle 5, n | H_{\text{M-E}} | ii \rangle|^2}{\varepsilon - \frac{J}{4} + (n-m)\omega_0} \right. \\ &\quad \left. + \frac{|\langle 5, n | H_{\text{M-E}} | iii \rangle|^2}{\varepsilon - \frac{J}{4} + (n-m)\omega_0} \right] \\ &= \sum_{m=0}^{\infty} \frac{4V^2 |\langle \tilde{n} | m \rangle|^2}{-\frac{U}{2} - \frac{J}{4} + (n-m)\omega_0} \end{aligned} \quad (\text{A.17})$$

- $\langle 6, n | \frac{i}{2} [s, H_{\text{M-E}}] | 6, n \rangle :$

$$\begin{aligned} \langle 6, n | \frac{i}{2} [s, H_{\text{M-E}}] | 6, n \rangle &= \sum_{m=0}^{\infty} \frac{|\langle 6, n | H_{\text{M-E}} | iv \rangle|^2}{-\varepsilon - U - \frac{J}{4} + (n-m)\omega_0} \\ &= \sum_{m=0}^{\infty} \frac{2V^2 |\langle \tilde{n} | m \rangle|^2}{-\frac{U}{2} - \frac{J}{4} + (n-m)\omega_0} \end{aligned} \quad (\text{A.18})$$

A.3.3 States involving the molecular state $|T, 0; n\rangle$

The state $|c\rangle |T, 0; n\rangle$, with c the band state, is coupled by means of $H_{\text{M-E}}$ to the following states:

- i) $c = \Omega : |\uparrow\rangle |0_a \downarrow_b\rangle |m\rangle$
- ii) $c = \downarrow : |\uparrow\downarrow\rangle |0_a \downarrow_b\rangle |m\rangle$
- iii) $c = \Omega : |\downarrow\rangle |0_a \uparrow_b\rangle |m\rangle$
- iv) $c = \uparrow : |\uparrow\downarrow\rangle |0_a \uparrow_b\rangle |m\rangle$
- v) $c = \downarrow : |\Omega\rangle |\uparrow\downarrow_a \downarrow_b\rangle |m\rangle$
- vi) $c = \uparrow\downarrow : |\uparrow\rangle |\uparrow\downarrow_a \downarrow_b\rangle |m\rangle$
- vii) $c = \uparrow : |\Omega\rangle |\uparrow\downarrow_a \uparrow_b\rangle |m\rangle$
- viii) $c = \uparrow\downarrow : |\downarrow\rangle |\uparrow\downarrow_a \uparrow_b\rangle |m\rangle$

The matrix elements are given in Table A.3.3. The states involving the triplet are abbreviated using the labels from Table 4.2.

Matrix element	Value
$\langle 7, n H_{\text{M-E}} i \rangle$	$V \delta_{n,m}$
$\langle 9, n H_{\text{M-E}} ii \rangle$	$-V \delta_{n,m}$
$\langle 7, n H_{\text{M-E}} iii \rangle$	$V \delta_{n,m}$
$\langle 8, n H_{\text{M-E}} iv \rangle$	$V \delta_{n,m}$
$\langle 9, n H_{\text{M-E}} v \rangle$	$-V \delta_{n,m}$
$\langle 10, n H_{\text{M-E}} vi \rangle$	$-V \delta_{n,m}$
$\langle 8, n H_{\text{M-E}} vii \rangle$	$V \delta_{n,m}$
$\langle 10, n H_{\text{M-E}} viii \rangle$	$-V \delta_{n,m}$

Table A.3: Matrix elements involving the molecular state $|T, -1; \tilde{n}\rangle$.

Diagonal corrections given by Eq. (4.36) are also shown:

- $\langle 7, n | \frac{i}{2} [s, H_{\text{M-E}}] | 7, n \rangle :$

$$\begin{aligned}
 \langle 7, n | \frac{i}{2} [s, H_{\text{M-E}}] | 7, n \rangle &= \sum_{m=0}^{\infty} \left[\frac{|\langle 7, n | H_{\text{M-E}} | i \rangle|^2}{\varepsilon - \frac{J}{4} + (n-m)\omega_0} \right. \\
 &\quad \left. + \frac{|\langle 7, n | H_{\text{M-E}} | iii \rangle|^2}{\varepsilon - \frac{J}{4} + (n-m)\omega_0} \right] \\
 &= \frac{2V^2}{-\frac{U}{2} - \frac{J}{4}}
 \end{aligned} \tag{A.19}$$

- $\langle 8, n | \frac{i}{2} [s, H_{\text{M-E}}] | 8, n \rangle :$

$$\begin{aligned}
 \langle 8, n | \frac{i}{2} [s, H_{\text{M-E}}] | 8, n \rangle &= \sum_{m=0}^{\infty} \left[\frac{|\langle 8, n | H_{\text{M-E}} | iv \rangle|^2}{\varepsilon - \frac{J}{4} + (n-m)\omega_0} \right. \\
 &\quad \left. + \frac{|\langle 8, n | H_{\text{M-E}} | vii \rangle|^2}{-\varepsilon - U - \frac{J}{4} + (n-m)\omega_0} \right] \\
 &= \frac{2V^2}{-\frac{U}{2} - \frac{J}{4}}
 \end{aligned} \tag{A.20}$$

- $\langle 9, n | \frac{i}{2} [s, H_{\text{M-E}}] | 9, n \rangle :$

$$\begin{aligned} \langle 9, n | \frac{i}{2} [s, H_{\text{M-E}}] | 9, n \rangle &= \sum_{m=0}^{\infty} \left[\frac{|\langle 9, n | H_{\text{M-E}} | ii \rangle|^2}{\varepsilon - \frac{J}{4} + (n-m)\omega_0} \right. \\ &\quad \left. + \frac{|\langle 9, n | H_{\text{M-E}} | v \rangle|^2}{-\varepsilon - U - \frac{J}{4} + (n-m)\omega_0} \right] \\ &= \frac{2V^2}{-\frac{U}{2} - \frac{J}{4}} \end{aligned} \quad (\text{A.21})$$

- $\langle 10, n | \frac{i}{2} [s, H_{\text{M-E}}] | 10, n \rangle :$

$$\begin{aligned} \langle 10, n | \frac{i}{2} [s, H_{\text{M-E}}] | 10, n \rangle &= \sum_{m=0}^{\infty} \left[\frac{|\langle 10, n | H_{\text{M-E}} | vi \rangle|^2}{-\varepsilon - U - \frac{J}{4} + (n-m)\omega_0} \right. \\ &\quad \left. + \frac{|\langle 10, n | H_{\text{M-E}} | viii \rangle|^2}{-\varepsilon - U - \frac{J}{4} + (n-m)\omega_0} \right] \\ &= \frac{2V^2}{-\frac{U}{2} - \frac{J}{4}} \end{aligned} \quad (\text{A.22})$$

A.4 List of commutation relations, relevant to Appendix A.1

- $[n_{i\alpha}, d_{a\sigma}] :$

$$\begin{aligned} [n_{i\alpha}, d_{a\sigma}] &= [d_{i\alpha}^\dagger d_{i\alpha}, d_{a\sigma}] = d_{i\alpha}^\dagger [d_{i\alpha}, d_{a\sigma}] + [d_{i\alpha}^\dagger, d_{a\sigma}] d_{i\alpha} \\ &= d_{i\alpha}^\dagger (\{d_{i\alpha}, d_{a\sigma}\} - 2d_{a\sigma}d_{i\alpha}) + (\{d_{i\alpha}^\dagger, d_{a\sigma}\} - 2d_{a\sigma}d_{i\alpha}^\dagger) d_{i\alpha} \\ &= -d_{i\alpha}\delta_{i,a}\delta_{\alpha,\sigma}. \end{aligned}$$

- $[n_{i\alpha}, d_{a\sigma}^\dagger] :$

$$\begin{aligned} [n_{i\alpha}, d_{a\sigma}^\dagger] &= [d_{i\alpha}^\dagger d_{i\alpha}, d_{a\sigma}^\dagger] = d_{i\alpha}^\dagger [d_{i\alpha}, d_{a\sigma}^\dagger] + [d_{i\alpha}^\dagger, d_{a\sigma}^\dagger] d_{i\alpha} \\ &= d_{i\alpha}^\dagger (\{d_{i\alpha}, d_{a\sigma}^\dagger\} - 2d_{a\sigma}^\dagger d_{i\alpha}) + (\{d_{i\alpha}^\dagger, d_{a\sigma}^\dagger\} - 2d_{a\sigma}^\dagger d_{i\alpha}^\dagger) d_{i\alpha} \\ &= d_{i\alpha}^\dagger \delta_{i,a}\delta_{\alpha,\sigma}. \end{aligned}$$

- $[n_{i\alpha}n_{j\beta}, d_{a\sigma}] :$

$$\begin{aligned} [n_{i\alpha}n_{j\beta}, d_{a\sigma}] &= n_{i\alpha} [n_{j\beta}, d_{a\sigma}] + [n_{i\alpha}, d_{a\sigma}] n_{j\beta} \\ &= -n_{i\alpha}d_{j\beta}\delta_{j,a}\delta_{\beta,\sigma} - d_{i\alpha}\delta_{i,a}\delta_{\alpha,\sigma}n_{j\beta} \end{aligned}$$

- $[n_{i\alpha}n_{j\beta}, d_{a\sigma}^\dagger]:$

$$\begin{aligned} [n_{i\alpha}n_{j\beta}, d_{a\sigma}^\dagger] &= n_{i\alpha} [n_{j\beta}, d_{a\sigma}^\dagger] + [n_{i\alpha}, d_{a\sigma}^\dagger] n_{j\beta} \\ &= n_{i\alpha} d_{j\beta}^\dagger \delta_{j,a} \delta_{\beta,\sigma} + d_{i\alpha}^\dagger \delta_{i,a} \delta_{\alpha,\sigma} n_{j\beta} \end{aligned}$$

- $[S_z^2, d_{a\sigma}^\dagger]:$

$$[S_z^2, d_{a\sigma}^\dagger] = d_{a\sigma}^\dagger [1 - 2n_{a\bar{\sigma}} + 2\sigma S_z^b], \quad (\text{A.23})$$

- $[S_z^2, d_{a\sigma}]:$

$$[S_z^2, d_{a\sigma}] = -d_{a\sigma} [1 - 2n_{a\bar{\sigma}} + 2\sigma S_z^b]. \quad (\text{A.24})$$

- $\sum_{i=a,b} \sum_{\sigma} [n_{i\alpha}, d_{a\sigma}^\dagger d_{b\sigma}]:$

$$\begin{aligned} \sum_{i=a,b} \sum_{\sigma} [n_{i\alpha}, d_{a\sigma}^\dagger d_{b\sigma}] &= \sum_{i=a,b} \sum_{\sigma} \{d_{a\sigma}^\dagger [n_{i\alpha}, d_{b\sigma}] + [n_{i\alpha}, d_{a\sigma}^\dagger] d_{b\sigma}\} \\ &= \sum_{i=a,b} \sum_{\sigma} \{-d_{a\sigma}^\dagger d_{b\sigma} \delta_{i,b} \delta_{\alpha,\sigma} + d_{a\sigma}^\dagger d_{b\sigma} \delta_{i,a} \delta_{\alpha,\sigma}\} \\ &= \sum_{i=a,b} d_{a\sigma}^\dagger d_{b\sigma} (\delta_{i,a} - \delta_{i,b}) = 0 \end{aligned} \quad (\text{A.25})$$

- $[n_{i\alpha}n_{j\beta}, d_{a\sigma}^\dagger d_{b\sigma}]:$

$$\begin{aligned} [n_{i\alpha}n_{j\beta}, d_{a\sigma}^\dagger d_{b\sigma}] &= n_{i\alpha} [n_{j\beta}, d_{a\sigma}^\dagger d_{b\sigma}] + [n_{i\alpha}, d_{a\sigma}^\dagger d_{b\sigma}] n_{j\beta} \\ &= n_{i\alpha} d_{a\sigma}^\dagger d_{b\sigma} \delta_{\beta,\sigma} (\delta_{j,a} - \delta_{j,b}) \\ &\quad + (\delta_{i,a} - \delta_{i,b}) \delta_{\alpha,\sigma} d_{a\sigma}^\dagger d_{b\sigma} n_{j\beta} \end{aligned} \quad (\text{A.26})$$

- $\sum_{i,\alpha} [n_{i\alpha}, S_+^a S_-^b]:$

$$\sum_{i,\alpha} [n_{i\alpha}, S_+^a S_-^b] = 0. \quad (\text{A.27})$$

- $[n_{i\alpha}n_{j\beta}, S_+^a S_-^b]:$

$$\begin{aligned} [n_{i\alpha}n_{j\beta}, S_+^a S_-^b] &= n_{i\alpha} S_+^a S_-^b (\delta_{ja} - \delta_{jb}) (\delta_{\beta\uparrow} - \delta_{\beta\downarrow}) \\ &\quad + (\delta_{ia} - \delta_{ib}) (\delta_{\alpha\uparrow} - \delta_{\alpha\downarrow}) S_+^a S_-^b n_{j\beta} \end{aligned} \quad (\text{A.28})$$

- $[S_z^2(a^\dagger - a), \sum_{i=a,b} \lambda_i (n_i - 1)(a^\dagger + a)]:$

$$\begin{aligned}
& \sum_{i=a,b} [S_z^2(a^\dagger - a), \lambda_i (n_i - 1)(a^\dagger + a)] \\
&= \sum_{i=a,b} S_z^2 [(a^\dagger - a), \lambda_i (n_i - 1)(a^\dagger + a)] \\
&= \sum_{i=a,b} S_z^2 \lambda_i (n_i - 1) [(a^\dagger - a), (a^\dagger + a)] \\
&= -2S_z^2 \sum_{i=a,b} \lambda_i (n_i - 1)
\end{aligned} \tag{A.29}$$

- $[S_z^2(a^\dagger - a), S_z^2(a^\dagger + a)]:$

$$\begin{aligned}
[S_z^2(a^\dagger - a), S_z^2(a^\dagger + a)] &= S_z^2 [(a^\dagger - a), S_z^2(a^\dagger + a)] \\
&= S_z^4 [(a^\dagger - a), (a^\dagger + a)] = -2S_z^4
\end{aligned} \tag{A.30}$$

- $[\sum_{i=a,b} \lambda_i (n_i - 1)(a^\dagger - a), \sum_{j=a,b} \lambda_j (n_j - 1)(a^\dagger + a)]:$

$$(\dots) = -2 \left[\sum_{i=a,b} \lambda_i (n_i - 1) \right]^2 \tag{A.31}$$

- $[\sum_{i=a,b} \lambda_i (n_i - 1)(a^\dagger - a), S_z^2(a^\dagger + a)]:$

$$(\dots) = -2S_z^2 \sum_{i=a,b} \lambda_i (n_i - 1). \tag{A.32}$$

APPENDIX B: DETAILED CALCULATION OF THE VARIATIONAL GROUND STATE FOR THE SIAM

We begin with the system of equations

$$\alpha_0 = \frac{2V \sum_{k < k_F} \alpha_k}{\varepsilon_d - \Delta}, \quad (\text{B.1a})$$

$$\alpha_k = \frac{2V^2 \sum_{k' < k_F} \alpha_{k'}}{(\varepsilon_d - \Delta)(\varepsilon_k - \Delta)}. \quad (\text{B.1b})$$

We take the square of (B.1b) and sum over \vec{k} , and substitute into (B.1a) to obtain

$$\begin{aligned} \sum_{k < k_F} \alpha_k^2 &= \sum_{k < k_F} \frac{4V^4 \left(\sum_{k' < k_F} \alpha_{k'} \right)^2}{(\varepsilon_d - \Delta)^2 (\varepsilon_k - \Delta)^2} \\ &= \frac{4V^4 \left(\sum_{k' < k_F} \alpha_{k'} \right)^2}{2D (\varepsilon_d - \Delta)^2} \int_0^D \frac{d\varepsilon}{(\varepsilon + \Delta)^2} \\ &= \frac{2V^4}{\Delta (\varepsilon_d - \Delta)^2 (\Delta + D)} \left(\sum_{k < k_F} \alpha_k \right)^2, \end{aligned} \quad (\text{B.2})$$

where we have taken the continuum limit and changed the integral from momentum to energy as

$$\sum_{k < k_F} \longrightarrow \int_{-D}^0 d\varepsilon \rho(\varepsilon) = \frac{1}{2D} \int_{-D}^0 d\varepsilon.$$

Now we use normalization to find the square of the sum:

$$\begin{aligned} \langle \Psi | \Psi \rangle &= \alpha_0^2 + 2 \sum_{k < k_F} \alpha_k^2 = 1 \\ &= \frac{4V^2 \left(\sum_{k < k_F} \alpha_k \right)^2}{(\varepsilon_d - \Delta)^2} \left[\frac{\Delta (\Delta + D) + V^2}{\Delta (\Delta + D)} \right], \end{aligned}$$

so that

$$\left(\sum_{k < k_F} \alpha_k \right)^2 = \frac{(\varepsilon_d - \Delta)^2}{4V^2} \frac{\Delta (\Delta + D)}{\Delta (\Delta + D) + V^2}. \quad (\text{B.3})$$

Upon substitution we obtain

$$2 \sum_{k < k_F} \alpha_k^2 = Q = \frac{V^2}{\Delta (\Delta + D) + V^2}, \quad (\text{B.4})$$

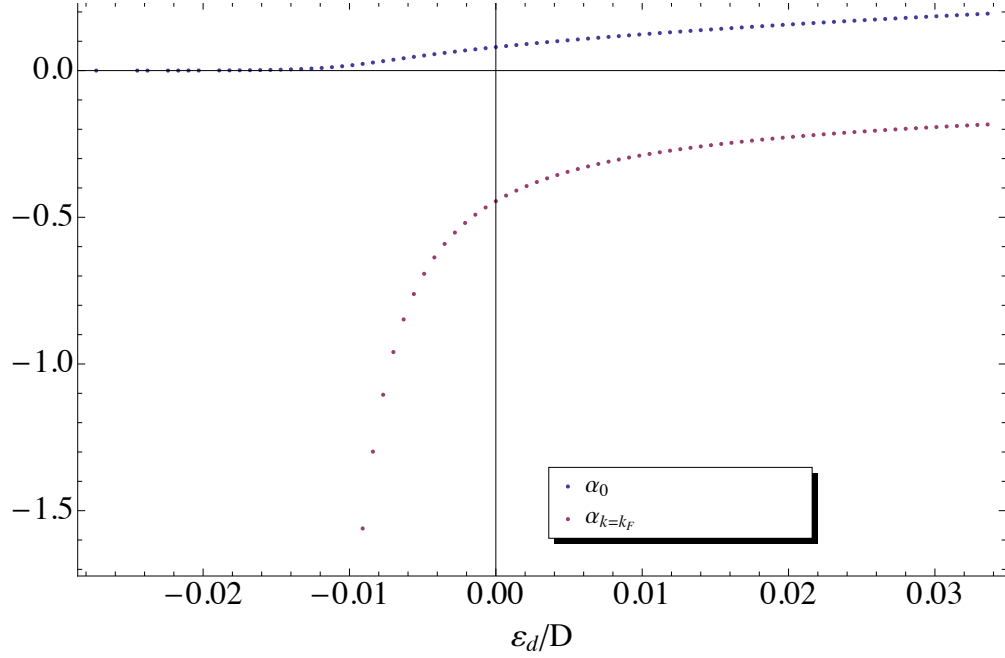


Figure B.1: Variational amplitudes as a function of the impurity level energy ε_d , for $V = 0.0357 D$.

and we have an expression for the charge and charge fluctuations at the QD.

We also substitute the square root of (B.3) onto (B.1a), which gives us an expression for α_0 :

$$\alpha_0 = \sqrt{\frac{\Delta (\Delta + D)}{\Delta (\Delta + D) + V^2}}. \quad (\text{B.5})$$

Immediately by substitution in (B.1b) we obtain the amplitudes α_k :

$$\alpha_k = \frac{V}{\varepsilon_k - \Delta} \sqrt{\frac{\Delta (\Delta + D)}{\Delta (\Delta + D) + V^2}}. \quad (\text{B.6})$$



OHIO
UNIVERSITY

Thesis and Dissertation Services